# Study on structural control of carbon nanowalls by surface reaction with radicals

**SHIMOEDA Hironao**

2014

Nagoya University

Department of Electrical Engineering and Computer Science

# Contents

## Chapter 1 Introduction



## Chapter 2 Experimental setup and evaluation methods of CNWs

## Chapter 3 Modification of CNW edges by reaction with oxygen atoms



## Chapter 4 Effects of ion irradiation to CNWs on reaction with radicals in oxygen plasma

## Chapter 5 Modification of edges and planes of CNWs using radicals in hydrogen peroxide solution



## Chapter 6 Conclusions and future works

# Chapter 1

# Introduction

## 1.1 Carbon nanomaterials

A chemical element of carbon with atomic number of 6 is expressed as a symbol "C". The electron configuration of carbon consists of $1s^2$ in the K-shell and $2s^2$ and $2p^2$ in the L-shell. Carbon has a lot of allotropes depending on various covalent chemical binds for the neighboring carbon-atoms due to the 2s- and 2p-orbitals having four electrons. Carbon atoms can mainly exhibit three types of different orbital hybridizations, sp, $sp^2$, and $sp^3$ [1]. There are many kinds of allotropes of carbon such as diamond, graphene sheet, and carbyne which consist of $sp^3$ hybridized orbitals (C-C), $sp^2$ hybridized orbitals (C=C), and sp hybridized orbitals (C≡C), respectively [2,3].

## Fullerene

Fullerene has been discovered by Kroto *et al.* in 1985 [4] and has a spherical structure. In fact, the presence of such structure had been estimated before the discovery of fullerene [5]. The name was homage to Richard Buckminster Fuller, whose geodesic domes it resembles. Fullerenes are molecules of varying sizes composed entirely of carbon and take a form a hollow sphere. Fullerene is composed of not only carbon hexagonal rings but also pentagonal or heptagonal rings. The structure of $C_{60}$ is a truncated icosahedron, which is similar in structure to a soccer ball made of twenty hexagons and twelve pentagons. The van der Waals diameter of $C_{60}$ molecule is approximately 1 nm.

## Carbon nanotubes (CNTs)

CNTs have been discovered to be a carbon nanomaterial with a cylindrical structure formed with rolled-up graphene sheets by Iijima [6]. CNTs are attracting great interests for remarkable properties and characteristics [7,8]. The CNTs have superior structural features such as high aspect ratios of up to 28,000,000:1, high mechanical strength, and high surface areas and various properties such as electrochemical and thermal stabilities and rich electronic and optical properties [9,10]. The high surface area and chemical inertness of CNTs give us possibilities for applications such as electrochemistry, catalysts, and supercapacitors [11-15]. Actually, according to these superior properties, various applications such as transparent conductors, thermal interfaces, antiballistic vests, and wind turbine blades are being put to practical use. Single-walled carbon

nanotubes (SWNTs) and multi-walled carbon nanotubes (MWNTs) can be synthesized using various growth methods such as high pressure arcs, laser ablation, and high pressure chemical vapor deposition (CVD) [16-20]. The structures of SWNTs can be conceptualized by wrapping a graphene sheet into a seamless cylinder with typical diameters of 0.8 to 2 nm and a bundle diameter of 10 to 30 nm.

To represent the wrapping angles of graphene sheets for the nanotubes, a pair of indices (*n*,*m*) called the chiral vectors are used as shown in Fig. 1.1 [21]. The integers *n* and *m* represent the number of unit vectors $a_1$ and $a_2$ along two directions in the honeycomb crystal lattice of graphene. The nanotubes are called as "zigzag" for $m = 0$ and "armchair" for $m = n$, which is expressed as "chirality". The electrical properties of CNTs are determined by the chirality, which gives both semiconducting and metallic characteristics. The CNTs can also provide expectations to develop semiconducting devices and interconnections in electric devices [22].

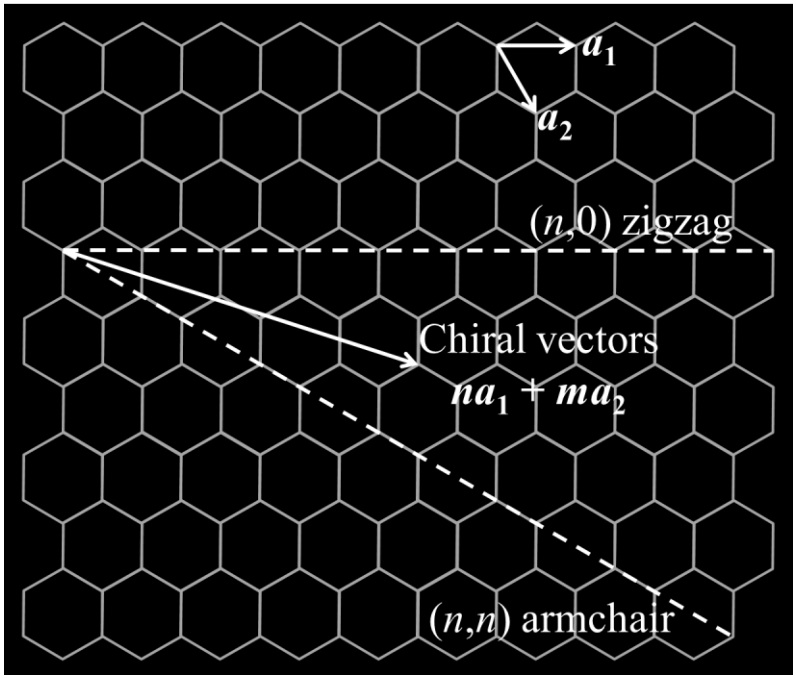


Fig. 1.1. Chiral vectors for CNTs.

## Graphene sheet

Graphene is monolayer of graphite with a two-dimensional (2D) honeycomb lattice and is a basic structural unit for various graphitic materials with other dimensionalities including fullerenes and CNTs [3]. Graphene can be viewed as an atomic-scale carbon network containing $sp^2$ C-C bonds with a bond length of 0.142 nm. Graphene can also be considered as an infinitely-large aromatic molecule including the limiting case of the family of flat polycyclic aromatic hydrocarbons.

A finite-sized graphene sheet has two types of edges which are an armchair and a zigzag edge shown in Figs. 1.2, respectively. Such different types of edge shapes have been experimentally observed using scanning tunneling microscopes (STM) [23]. Fujita *et al*. have expected by theoretical calculations that the electronic property of graphene depends on the edge shapes and system sizes [24–25]. In particular, they have pointed out that such edge effects can contribute to the electrical characteristics of only nanometer-sized graphene such as nanoribbons and should vanish in bulk graphite.

In 2004, Novoselov *et al*. have reported by the experimental results of transport measurements that graphene has an extremely-high electron mobility of more than 15 000 $cm^2V^{-1}s^{-1}$ even at room temperature [26]. In addition, carriers in graphene can be tuned continuously between electrons and holes and concentrations $n$ are approximately $10^{13}$ $cm^{-2}$ [26-28]. The observed mobilities are practically independent of temperature $T$ and still limited by scattering on defects. Therefore it can be improved, perhaps, even up to around the theoretical expectation value of 100 000 $cmV^{-1}s^{-1}$ [3]. This value of the mobility is higher than that reported for small gap InSb.

Since then, both experimental and theoretical reports on graphene have drastically increased. Especially, nanometer-sized graphenes such as graphene nanoribbons (GNRs) have received a lot of attention with respect to characteristic electronic properties that two-dimensional larger-sized (or infinite-sized) graphene doesn't have [29-32]. The GNRs can be classified according to the edge shape as either armchair GNRs (AGNRs) or zigzag GNRs (ZGNRs). It is now well known by density functional theory (DFT) calculations that AGNRs exhibit semiconducting properties with an energy band gap inversely proportional to the ribbon width [33]. In contrast, ZGNRs exhibit metallic properties due to a different edge state which prevents an energy band gap from opening [24,25]. On the other hand, more recent DFT calculation results have shown that a ordering of magnetic ordering is allowed to split the edge states [34-38].

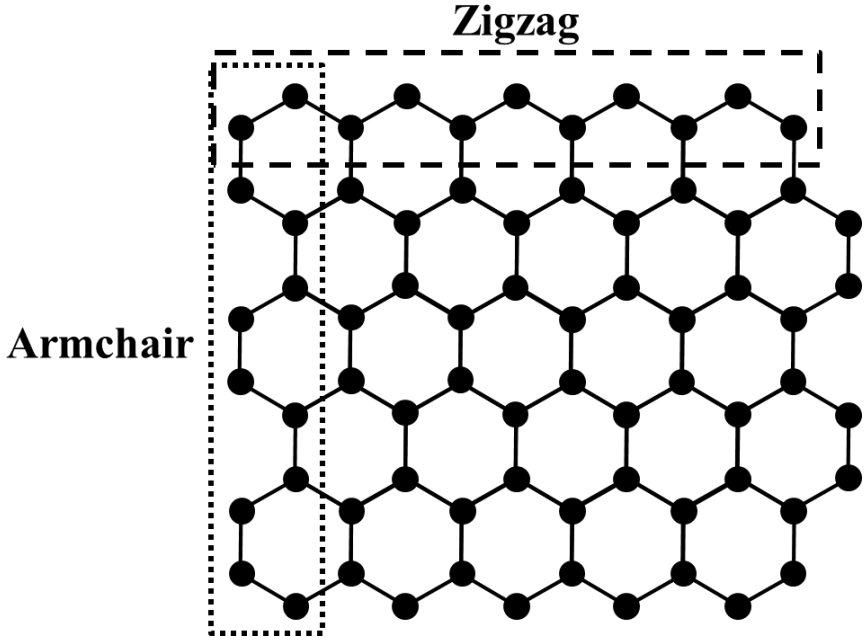


Fig. 1.2. Zigzag and armchair edges of a graphene nanoribbon.

# 1.2 Carbon nanowalls (CNWs)

## 1.2.1 Morphology and characteristics

Carbon nanowalls (CNWs) are also one of carbon nanomaterials consisting of stacks of nanometer-scaled graphene sheets which are vertically aligned on a substrate as shown on the upper side of Fig. 1.3 [39,40]. A stack of graphene sheets is a few nanometers to a few tens of nanometers in thickness which corresponds to more than ten graphene sheets. The height of each wall is controllable by growth time and up to several micrometers. Due to its characteristic wall structure, CNWs exhibit a high aspect ratio and large surface area. A batch of graphene sheets constituting each wall is crystallographically seamless. On the other hand, there are not only a lot of top edges of the walls but also bending or branching walls in CNWs forming a mazelike architecture. Each wall is considered to be composed of nanographite domains with a relatively high degree of graphitization and to contain domain boundaries on the six-membered ring plane which are distinguishable according to crystallographic distortions and defects as shown on the lower side of Fig. 1.3 [41].

These structural features of CNWs may possess characteristic electronic states which are different from those of other carbon nanomaterials such as planar nanographene and carbon nanotubes (CNTs) and open a new avenue to electronic, magnetic, and optical devices. For example, it has been found that while soft X-ray emission spectra of CNWs which indicate the energy band structure have similar behaviors as those for the highly oriented pyrolytic graphite (HOPG), the peaks

corresponding to π-band structures near the K-point in the spectra exhibit different behaviors [42,43]. These results mean that CNWs have similar but not identical electronic structures as the HOPG.

In general, graphene nanoribbons (GNRs) with a width of less than tens of nanometers have an energy band gap caused by the edge state [24,29,44]. CNTs exhibit both metallic and semiconducting properties significantly depending on the tube diameter and wrapping angle [45]. On the other hand, CNWs also exhibit semiconducting properties caused by structural fluctuations as described above such as graphitic distortions and chemical impurities [46-48]. Actually, as shown in Fig. 1.4, Hall measurements of CNWs have demonstrated that CNWs possess semiconducting electrical properties [46]. In Fig. 1.4(a), there are the intrinsic (I) and saturation (II) regions in the carrier concentration as a function of the reciprocal of the temperature. Additionally, the Hall coefficients in Fig. 1.4(b) change positive to negative by nitrogen (N) doping, which means a change in the carrier type from p- to n-type [47]. It has been found not only electrically by the Hall measurements but also optically by spectroscopic ellipsometry that CNWs have the energy band gap of more than 80 meV [48].

In the previous studies, applications utilizing some features of CNWs such as relatively-macroscopic wall structures, conductivity, huge sustainable current, and chemical and physical strength have been focused. For example, measurements of field emission properties and supporting processes of Pt or $TiO_2$ nanoparticles have been demonstrated toward realizing field emitters, electrodes for fuel cells, and organopollutant degradation devices [49-52].

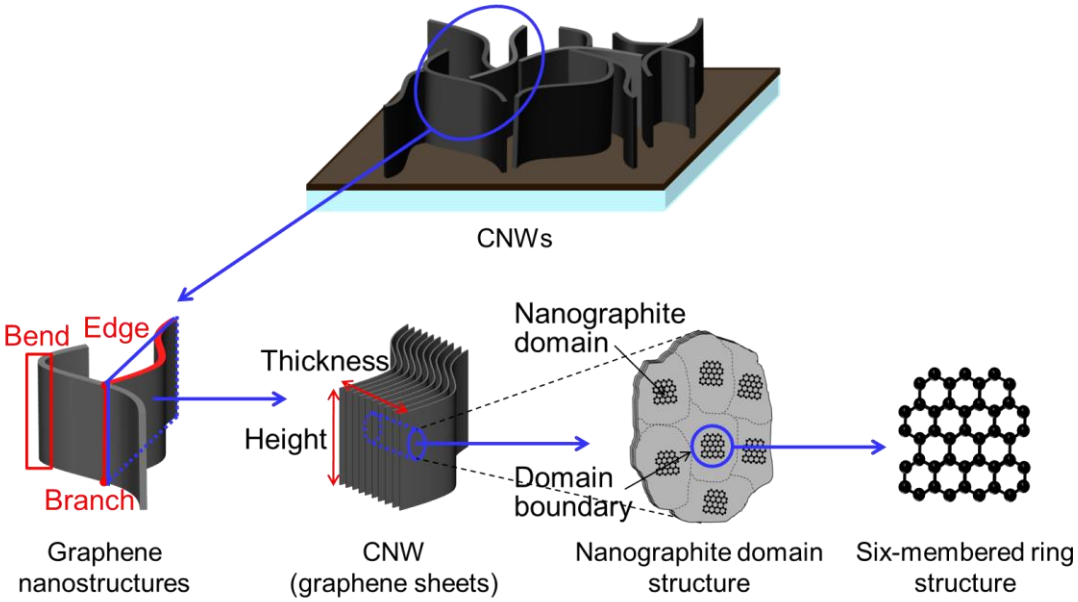


Fig. 1.3. Schematics of structures of CNWs including graphene nanostructures, a layered structure of graphene sheets, and nanographite domains.

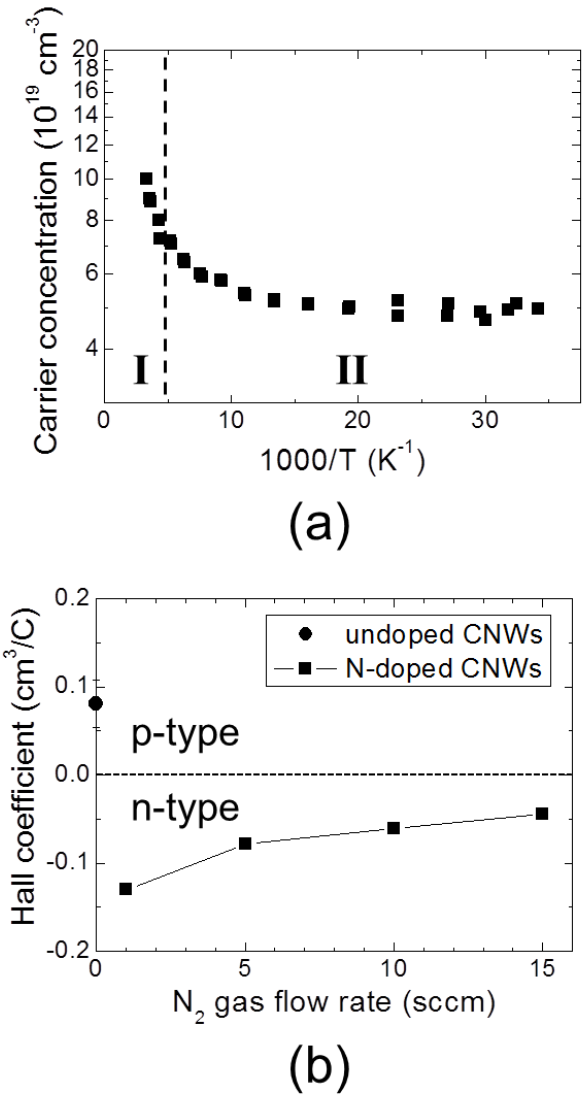


Fig. 1.4. Semiconducting properties of CNWs based on Hall measurements. (a) Carrier concentration as a function of the reciprocal of the temperature and (b) Hall coefficient and resistivity as functions of $N_2$ flow rate during the growth.

### 1.2.2 Growth mechanism and growth control

To gain better understanding of structural and electronic properties of CNWs toward various applications, control of the morphologies and chemical states is one of critical issues. Some control techniques of the complicated structures of CNWs have been developed by focusing on growth mechanism, conditions, and treatments after the growth.

The growth mechanism of CNWs employing plasma-enhanced chemical vapor deposition (PECVD) with $C_2F_6/H_2$ gases (this type of CNWs is called CF-CNWs in this thesis) has ever been discussed [53]. Figure 1.7 shows the initial growth model of CF-CNWs on a Si substrate. In the initial growth stages of CF-CNWs, nanoislands consisting of particulate amorphous carbon (a-C) are first nucleated, an aggregation of the carbon nanoislands forms an interface layer, and CF-CNWs then begin to grow at the nuclei on the interface layer. Although the nucleated graphene sheets are randomly orientated, those standing more vertically on the substrate preferentially grow and form vertically-aligned nanographene sheets. This is due to a difference between growth rates in the *a* direction along the strongly-bonded planes of graphene sheets and in the *c* direction along the weakly-bonded layers of the sheets. Our following studies have modified the above growth model to a new one as shown in Fig. 1.5. First, an a-C interface layer is formed, then, carbon nanoislands as nuclei of CF-CNWs are created on the interface layer, and finally, the vertical growth of nanographene sheets starts.

Furthermore, critical factors of nucleation and vertical growth of CF-CNWs have been also discussed [54]. The irradiation of ions can form dangling bonds on the growth surface and enhance adsorptions of $CF_x$ radicals. Concretely, despite the relatively-low

sticking coefficient of $CF_3$ which is one of critical species affecting CNW growth, the adsorption of $CF_3$ radicals can increase by ion bombardments. Such adsorptions and following abstraction of F atoms from absorbed $CF_x$ by H radicals result in formation of carbon films. At the initial stage, the a-C nanoislands can be formed only under the condition with ion irradiations. Moreover, nucleation of CF-CNWs can also occur on the nanoisland surfaces irradiated with the ions. However, while no ions with a relatively low energy can induce such nucleation, too high-energy ions also inhibit the CF-CNW growth due to etching effects. In the case of a too large ion flux, the deposition rate of a-C film is higher than the nucleation rate of CF-CNWs. As a result, not CF-CNWs but carbon films like a-C film containing both $sp^2$ and $sp^3$ components are formed under such high fluxes of ions. Consequently, vertical growth of graphene sheets constituting CF-CNWs requires ion irradiations with an appropriate energy and flux.

In contrast, some researchers have investigated an initial growth stage of CNWs synthesized using PECVD with $CH_4/H_2$ gases (this type of CNWs is called CH-CNWs in this thesis) by grazing incidence X-ray diffraction (XRD) [55]. They have demonstrated that the orientation of the graphene sheets in CH-CNWs changes from parallel to perpendicular to the substrate surface with increasing the growth time. At such a critical growth phase when the orientation changes, a characteristic crystalline phase may be formed.

In addition, it has been reported that the $H_2/CH_4$ flow rate ratio during direct current PECVD are some of critical factors in affecting the growth process and the structures of CH-CNWs [56]. In the region with less hydrogen at the $H_2/CH_4$ ratios ranging from 0 to 2, the wall size (height and length) increases while there is no change in the crystallinity

estimated by Raman spectroscopy. The results indicate that the hydrogen etching effect may be not enough to promote graphitization of CH-CNW film. On the other hand, it is clear that the density of CH-CNWs decreases with increasing $H_2/CH_4$ ratio. At the $H_2/CH_4$ flow rate ratios ranging from 2 to 4, the wall size decreases presumably due to a decrease in the amount of carbon-containing species while the crystallinity tends to increase due to hydrogen etchings of amorphous components as suggested by Shimabukuro *et al*. [57]. These results indicate that the hydrogen etching effect is one of critical factors in the growth of CH-CNWs and play an important role for determining the wall size, density, and crystallinity.

As another approach to control the crystallinity of CNWs synthesized using PECVD, the effects of $O_2$ gas addition to the process gas mixture of $C_2F_6/H_2$ on the structure of CF-CNWs have been also investigated [46]. CF-CNWs with $O_2$ addition exhibit less branching than those synthesized without $O_2$ addition and its growth rate decreases with increasing the additional $O_2$ gas flow rate. Figure 1.6 shows cross-sectional transmission electron microscope (TEM) images of the CF-CNWs grown without and with $O_2$ addition. Small overlapping nanographite domains are randomly orientated in Fig. 1.6(a) of the CF-CNWs grown without $O_2$ addition. In contrast, for the CF-CNWs grown with $O_2$ addition, monolithic self-sustaining graphene sheets with a size of more than 200 nm stand on the substrate. The magnified TEM images show that while there are bent graphene sheets with in the CF-CNWs grown without $O_2$ addition, a highly-orientated and smooth graphene sheets are clearly observed in the CF-CNWs grown with $O_2$ addition.

The degree of vertical structure of the CF-CNWs is evaluated using the ratio of the 002 peak intensity ratio to the 100/101 integrated intensity ratio ($I_{002}/I_{100/101}$) in

synchrotron XRD patterns. The $I_{002}/I_{100/101}$ ratio for the CF-CNWs grown with $O_2$ addition has been found to be approximately twice larger than that for the CF-CNWs grown without $O_2$ addition. The fact indicates that the orientation of the vertically standing graphene sheets is improved by effects of additional $O_2$ gas on the CF-CNW growth. $O_2$-related species can act as eliminators of impurities such as fluorine (F) atoms and small graphitic fragments, which leads to improve the crystallinity and orientation of CNWs.

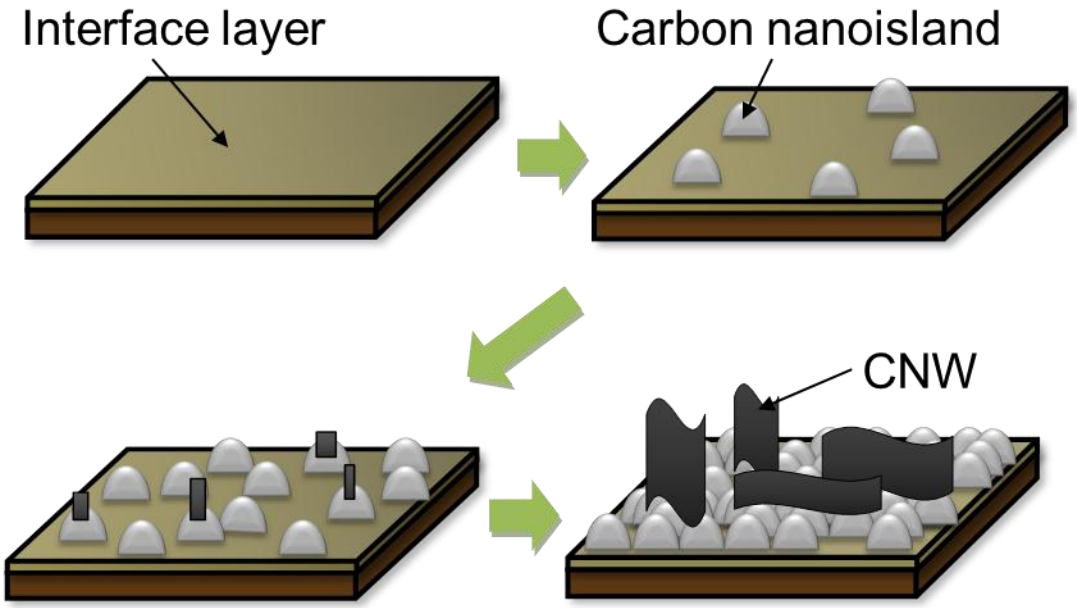


Fig. 1.5. Initial growth model of CNWs on a Si substrate.

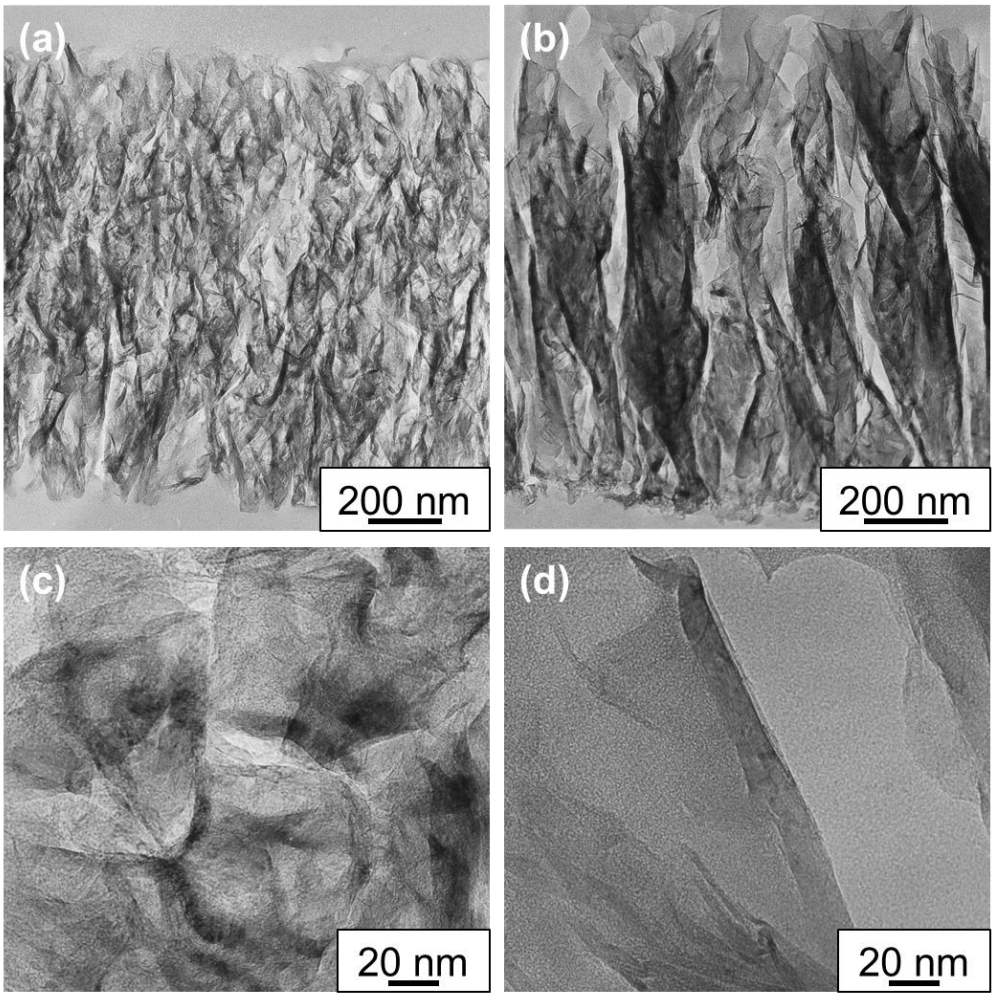


Fig. 1.6. Cross-sectional TEM images of CNWs grown (a) without and (b) with additional $O_2$ gas and (c),(d) each magnified view.

### 1.2.3 Post-growth processing

Growth control techniques as described in the previous section are not enough to precisely control the complicated structures of CNWs for developing their properties and realizing applications. One growth condition such as power, pressure, and flow rate ratio of mixture gases during PECVD affects and changes some structural parameters such as height and length of each CNW, orientation, and crystallinity. Smaller scale modifications and chemical changes such as functionalization only may be achieved by some kinds of treatments after the growth of CNWs.

Because CNWs have both a high density of edges and a large surface area of planes based on graphene, states of such edges and planes need to be crystallographically and chemically controlled, which significantly affects physical, chemical, and electronic properties. In addition, modification and control of structural fluctuations such as bends and branches in walls and various graphitic defects including domain boundaries are also necessary to precisely control the properties. Meanwhile, these structural modifications have to be selectively conducted to clarify each effect on the properties and achieve the precision control. Therefore, post-growth processings are also so important for controlling the structural factors of CNWs in their properties.

Surface chemical modifications have been successfully developed for controlling the surface characteristics of CNWs such as wettability using plasma treatments. Argon (Ar) atmospheric pressure plasma treatment has been applied to surface chemical modification for controlling the wettability of CF-CNWs by our research group [58]. Before the plasma treatment, the CF-CNW surface has been found to be almost super hydrophobic by measurements of the contact angle of the water droplets on the

CF-CNW surface. The contact angle obviously decreases by the plasma treatment, which induces a change in the surface wettability to super hydrophilic.

At the same time, chemical states of CF-CNWs significantly change after the plasma treatment whereas there is almost no change in the morphologies and crystalline structures. Figure 1.7 shows composition ratios of fluorine (F) to carbon (C) and oxygen (O) to C in CF-CNWs as a function of the plasma treatment time evaluated from X-ray photoelectron spectroscopy (XPS). On the surfaces of CF-CNWs before the treatment, there are some F atoms which may be incorporated during the PECVD growth processes employing a fluorocarbon gas. Such F atoms can induce F-terminated edges of CF-CNWs, which leads to their hydrophobic surface properties. After the plasma treatment only for 2 s, while the amount of F atoms drastically decreases, that of O atoms clearly increases at the same time. This result suggests that some oxygen-related species such as O radicals generated in the atmospheric pressure plasma can form some oxygen functional groups such as OH and COOH and may also contribute to desorption of F atoms. Both desorption of F atoms and chemisorption of O atoms on the surfaces of CF-CNWs result in a drastic change to hydrophilic surface properties.

On the other hand, the surfaces of CH-CNWs are rather hydrophilic and change to be super-hydrophilic after the Ar atmospheric pressure plasma treatment for more than 1 s. At that time, the oxygen content increases sharply while there is also no change in the morphologies and crystalline structures. In contrast, a super-hydrophobic CH-CNW surface can easily be obtained by post-growth $CF_4$ plasma treatment [59]. Accordingly, it has been found that the surface chemical states such as chemisorption of F and O atoms in CNWs can be modified by the plasma treatments and dominantly affect the wettability.

Plasma treatments of CNWs also have been applied for doping into the graphitic structures affecting the electrical properties. Nitrogen plasma (NP) treatments of CNWs have been demonstrated to enhance the field emission properties by our research group [49]. Figure 1.8(a) shows the XPS N 1s spectrum of the CNWs after the NP treatment. The atomic composition (at. %) of N on the CNW surface after the NP treatment is determined to be approximately 2 to 3 at. % with the peak intensity ratio of N 1s to C 1s (285 eV). The N 1s spectrum can be decomposed into two main Gaussian peaks around 398.6 and 401.2 eV which correspond to $sp^2$ C-N bonds in pyridine and graphite-like structures, respectively. As shown in Fig. 1.8(b), no C-N bond in a pyridine structure with two σ bonds, one π bond, and one paired electrons can contribute to electron doping into the graphitic structures of CNWs, those in a graphite-like structure with three σ bonds, one π bond, and one unpaired electron can be doped by dominating π electrons.

From the N 1s spectrum, the NP treatment can induce N-doping in the surface of CNWs. Measurements of field emission current have shown that the threshold field for the NP-treated CNWs at which the emission current reaches 0.1 μA is slightly lower than that for the untreated CNWs. Meanwhile, the electron emission current dramatically increases after the NP treatments. In the case of $N_2$ plasma treatment at lower pressures, the surface chemical states such as nitrogen chemisorption including N-doping also have been modified and found to affect the electrical properties of CNWs.

Plasma etchings are usually necessary to form fine patterns for fabrication of various devices. The reactive ion etchings (RIEs) of CNWs using $N_2/H_2$ or $Ar/H_2$ plasma have been also demonstrated to develop some kinds of fabrication processes of

CNW devices such as electronic devices [60]. In the case of $N_2/H_2$ plasma etching from the top surface of CNW films, CNWs are anisotropically etched at the etch rate of 250 nm/min, while the interface layer composed of amorphous components on the bottom surface of the CNW film is hard to be etched. On the other hand, the interface layer can be completely removed using $Ar/H_2$ plasma etching from the bottom surface of the exfoliated CNW film with inducing a characteristic morphology. For such RIEs, the heights of CNWs or amount of C atoms decrease preferentially from the areas irradiated with ions, which can be useful for patterning techniques with some masks.

Liquid-phase treatments also have been studied to functionalize the surfaces of CNWs and modify the morphologies and crystallinities. For instance, unintentionally N-doped CNWs have been oxidized by anodic polarization in mild electrolyte solution of $K_2SO_4$ [61]. Noticeable surface morphology changes and significant electrochemical oxidation happen. At that time, the electrochemical oxidation proceeds through C=C bond breaking and form some oxygen functional groups such as C=O, C-OH, and O-C-O. This method of electrochemical oxidation in a $K_2SO_4$ solution can change both macroscopic morphologies and chemical states in the whole structure of CNWs.

As described above, post-growth processings such as plasma treatments enable us to produce morphological, crystallographic, and chemical changes in the structures of CNWs. However, the previous studies have focused only on relatively-macroscopic structural changes. Especially, such modifications of morphologies, crystalline structures, and surface chemical states should be controlled at least for the edges and planes in CNWs separately. Furthermore, because various graphitic defects in CNWs are highly sensitive to surface reactions with a variety of species, each reaction process needs to be clarified in detail. To develop and control the properties of the CNWs, more

precise and highly-selective modification techniques are needed.

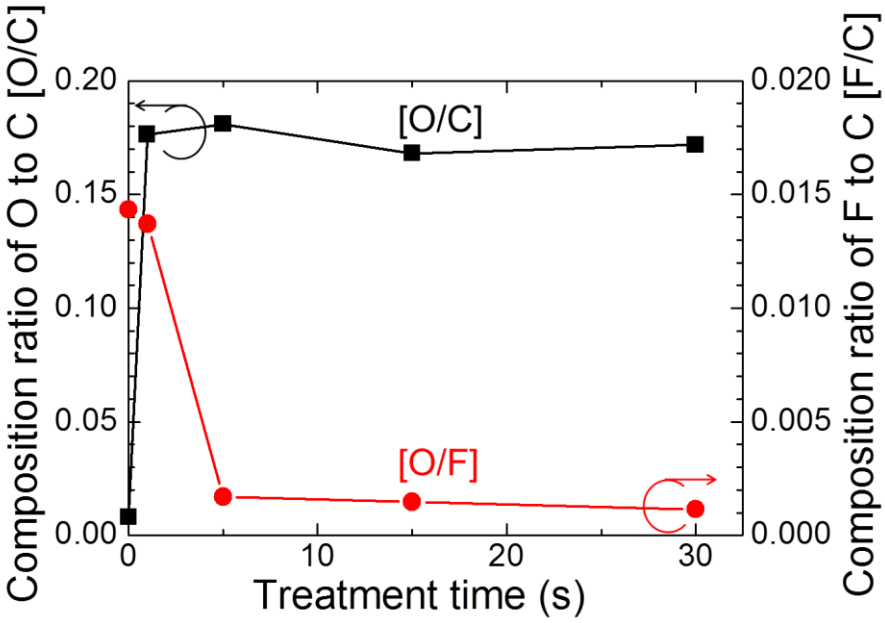


Fig. 1.7. Composition ratios of fluorine (F) to carbon (C) and oxygen (O) to C in CNWs evaluated from X-ray photoelectron spectra as a function of the plasma treatment time.

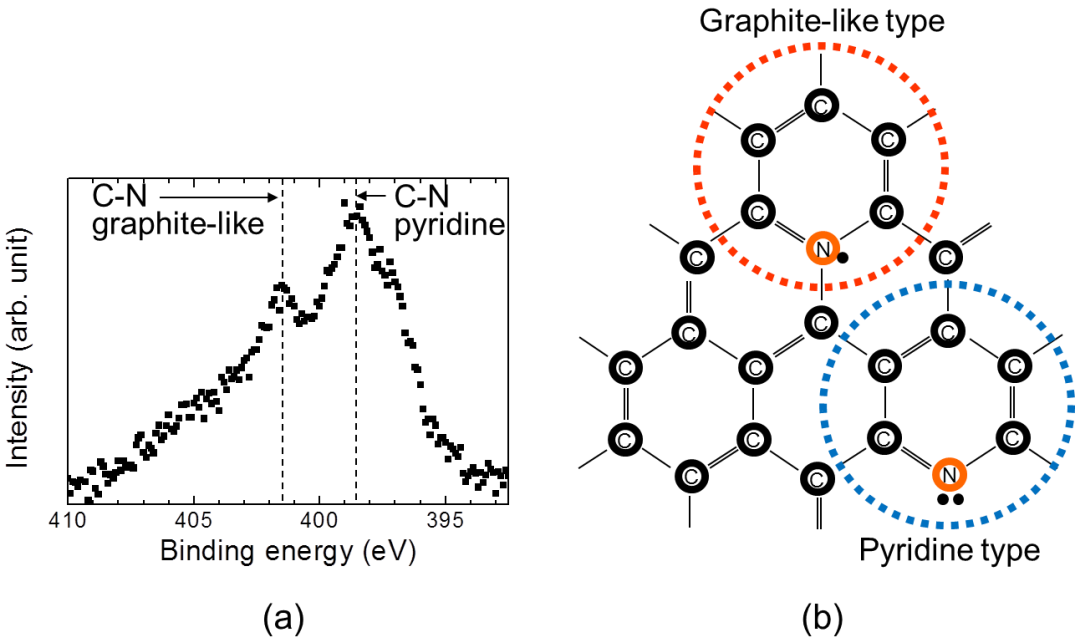


Fig. 1.8. (a) N 1s photoelectron spectra for CNWs after the NP treatment. (b) Structural model of $sp^2$ C-N bonds in a graphitic structure .

# 1.3 Defects and distortions in graphitic structures

## 1.3.1 Crystallographic defects and distortions [62]

Defects in three-dimensional crystals are referred to as *intrinsic* and *extrinsic* defects when the crystalline order is perturbed without and with foreign atoms denoted as impurities. Intrinsic defects can be distinguished by dimensionality. Point defects typically including vacancies or interstitial atoms are zero-dimensional, whereas dislocations are considered to be based on one-dimensional lines of defects. Grain boundaries or stacking faults are two dimensional defects, while inclusions and voids have a three-dimensional finite size. Existence of foreign atoms may be categorized into zero-dimensional defects if the foreign atoms substitute constituent atoms of the crystal or are located on interstitial sites.

On the other hand, agglomerations of foreign atoms become more dimensional defects. As the reduced dimensionality of graphene decreases the number of possible defect types, the concept of point defects is quite similar to bulk crystals, but line defects play a different role. Truly no three-dimensional defect even exists in graphene. It is well-known that defects are not always stationary and their migration can significantly affect the properties of a defective crystal. In a graphene lattice, each defect exhibits a certain mobility in the direction parallel to the graphene plane. In general, an activation barrier which depends on the defect type govern the migration, which results in an exponential dependence on temperature.

## (a) Point Defects

***Stone-Wales defect***

One of the unique properties of the graphene lattice is its possible reconstruction by forming nonhexagonal rings. Stone-Wales (SW) defect is the simplest example, which involves no removed or added atom [63]. Four hexagons are transformed into two pentagons and two heptagons by rotation of one C-C bond by 90˚ [SW(55-77) defect], which has a formation energy $E_f$ = 5 eV [64,65]. An in-plane bond rotation by simultaneous movement of the two involved atoms induce the transformation with the kinetic barrier of about 10 eV [64]. There is no change in the number of C atoms and no dangling bonds in the defected graphene lattice. The energy barrier for the reverse transformation is about 5 eV. Such high formation energy of the SW defect means an equilibrium concentration is negligible at least at typical experimental temperatures below 1000 ˚C. However, once the defect is formed under nonequilibrium conditions (e.g., rapid quenching from high temperature or under irradiation), the barrier of 5 eV for the reverse transformation should allow its stability at room temperature.

***Single Vacancies***

Missing lattice atom is formation of the simplest defect in any material. Single vacancies (SV) in a graphene lattice have been experimentally observed in graphene or a surface layer of graphite by TEM and STM [66-68]. The SV is formed through a Jahn-Teller distortion which results in the saturation of two of the three dangling bonds toward the missing atom. One dangling bond always remains due to geometric reasoning, which leads to the formation of a five-membered and a nine-membered ring [$V_1$(5-9) defect]. The local density of states at the Fermi energy on the SV is higher than that on the pristine region due to the spatially-localized density of states on the dangling

bonds. It is intuitively clear that the presence of an under-coordinated carbon atom makes the formation energy of such a defect high. In fact, the value has been calculated to be $E_f$ = 7.5 eV, which is much higher than the formation energies of vacancies in many other materials [69,70].

***Multiple Vacancies***

Double vacancies (DV) can be created either by the incorporation of two SVs or by missing two neighboring atoms. Four hexagons in perfect graphene are transformed into two pentagons and one octagon [$V_2$(5-8-5) defect], which leads to no dangling bond in a fully reconstructed DV. A theoretical simulation has shown that the formation energy $E_f$ of a DV is of the same order as that for a SV (about 8 eV) [69,70]. However, considering one missing atom in a DV, the energy per missing atom (4 eV per atom) is much lower than that for a SV. Hence, DVs are thermodynamically superior to SVs. The $V_2$(5-8-5) defect is not the only energetically favored way for a graphene lattice to accommodate two missing atoms. Similar to the creation of a SW defect, the octagon of the $V_2$(5-8-5) defect are transformed into an arrangement of three pentagons and three heptagons by the rotation of one of the bonds [$V_2$(555-777)] [71]. The formation energy of $V_2$(555-777) is approximately 1 eV lower than that of $V_2$(5-8-5). The further transformation of the $V_2$(555-777) form a $V_2$(5555-6-7777) defect through rotating another bond. The formation energy of $V_2$(5555-6-7777) is between those of $V_2$(5-8-5) and $V_2$(555-777).

## ⑹ One-Dimensional Defects

***Dislocation-like Defects***

Several experimental studies of graphene have shown the existence of

one-dimensional defects [72-75]. In general, the line defects are tilt boundaries between two domains with different lattice orientations with respect to the tilt axis normal to the plane. Such defects can be considered as a row of reconstructed point defects [76-78]. For example, a domain boundary due to mismatch in a graphene lattice consists of an alternating line with pairs of pentagons separated by octagons. Obviously, (5-8-5) divacancies form such a defect through the alignment along the zigzag lattice direction of graphene. Some one-dimensional defects in a graphene lattice are similar to a dislocation in a conventional crystal. However, in a graphene lattice, there is no screw dislocation which requires a three-dimensional strain field. On the other hand, a kind of edge dislocations can be imagined in graphene only as its projection onto a plane due to no dislocation line normal to the layer.

Such a dislocation in graphene has been conceptually described as a semi-infinite strip on the layer [77]. A pentagon-heptagon pair with no dangling bond which exists at the end of the strip plays a role of the dislocation core. Domains with different crystal orientations in a graphene plane are frequently separated with line defects. As an example, the growth of graphene on metal surfaces has induced such situations due to because simultaneous nucleation of graphene at different points leading to independent two-dimensional domains, corresponding to grains in three-dimensional crystals [73,75]. Normally, graphene can be synthesized on metal surfaces of hexagonal symmetry by chemical vapor deposition. Different lattice orientations in neighboring grains may be caused by the misfit between metal and graphene. Therefore, a line defect is formed on a boundary between two neighboring graphene grains with differing orientations. The linear defect should be of paramount importance with respect to grain boundaries in graphene. In the case of polycrystalline materials, the properties strongly depend on the

size of their grains and the atomic structure of the grain boundaries. On the other hand, the role of such structures should be referred for two-dimensional materials such as graphene because line defects can divide and disrupt their crystals. In particular, grain boundaries may dominantly affect the electronic transport in such crystals [77].

***Defects at the Edges of a Graphene Layer***

There are edges at the end of each graphene, which are terminated with the edge atom being either free or covered with hydrogen atoms. Two types of the simplest edge structures of the armchair and the zigzag orientation can be reconstructed, which enables us to imagine edges with any other directions between these two [79,80]. However, the zigzag and armchair orientations seem to be preferred with respect to the minimum number of dangling bonds at the edge. Local changes in the reconstruction type and sustaining removal of carbon atoms from the edges induce defective edge, which even can transform armchair edges into zigzag edges [81]. Defective edges can be also considered as an intermediate structure of such transformation. For example, an edge defect is formed by the removal of one carbon atom from a zigzag edge, which is composed of a row of hexagons with one pentagon in the middle of the edge. In addition, edge structures can be reconstructed to different combinations of pentagons and heptagons at the edge. Besides, chemical species such as hydrogen atoms can saturate dangling bonds at the edge under ambient conditions, which can be considered as disorders and dramatically increase the number of possible edge defects.

### 1.3.2 Chemical defects

Chemical reactions of carbon atoms in graphene with other species can induce some kinds of defects. Chemisorption on graphene is expected to affect fundamental properties of graphene through chemically-modification of the crystalline structure. Such intentional functionalization of graphene with hydrogen, oxygen-containing groups, or other elements and chemical groups is of great interest as a way to engineer different properties. Additionally, functionalized graphene plane and edge can be identified and affect the properties through different contributions.

**Graphene plane [82-84]**

Chemisorption structures of hydrogen (H), nitrogen (N), phosphorus (P), and some oxygen-containing species (O and OH) on pristine graphene are compared here.

For H chemisorption, the most stable configuration is for H atom to bond on top of a carbon atom forming an $sp^3$ hybridization with an adsorption energy of -1.20 eV. The H-bonded C atom moves 0.39 Å outward away from the graphene plane, which breaks the symmetry of the graphene, and changes the $sp^2$ hybridization of the graphene to an $sp^3$ hybridization locally [85-87].

For N or P chemisorption, N or P bonds vertically with two C atoms at the bridge site, which forms a planar and non-equivalent $sp^2$ hybridization structure perpendicular to the graphene plane with adsorption energies of -2.85 and 0.73 eV [88]. The two C atoms bonded to the N or P change to a $sp^2$-$sp^3$ hybridization and move outward from the graphene plane by 1.10 and 0.50 Å, respectively.

The amplitude of corrugation on P-chemisorbed graphene is smaller than that on

N-chemisorbed one, which indicates that the C-C bond below the P atom retains more the $sp^2$ character and rehybridizes relatively weakly with the P atomic orbitals. The equilibrium distance between the adatom and C is 1.13, 1.46 and 1.94 Å for H, N and P, respectively. The bond length of C-C is 1.42 Å and increases to 1.50, 1.46 and 1.46 Å due to the H, N, and P atoms bonding to one C atom in the C-C, respectively.

For O chemisorption, O atom interacts with pristine graphene to form a highly stable spin singlet epoxide-like structure with an adsorption energy of 1.91 eV, which is consistent with experimental results [89]. The C-O distances in the epoxide-like structure is optimized to be 1.47 Å and the C-C bond length in the three-membered ring increase from 1.42 Å to 1.50 Å. A spin-triplet epoxide structure is optimized to be with an adsorption energy of 1.56 eV, which means less stable than the singlet one. The localized unpaired spin density of the triplet hardly exists on the epoxide-functionalized graphene.

For OH chemisorption, OH molecule adsorbs with C atoms through forming a C-O bond with H pointing in the direction of the center of a hexagonal ring, which has an adsorption energy of -0.54 eV. Similarly to the H chemisorption on pristine graphene, the adsorbed OH molecule breaks one of the $sp^2$ C-C bonds, leading to transformation of the $sp^2$ hybridization to $sp^3$ [90,91]. Diffusion of the OH adsorbed on graphene surface can easily occur with an energy barrier of 0.32 eV. In this process, the H atom remains pointing toward the center of a hexagonal ring while O moves from one C atom on top of the ring to the adjacent one. In the diffusion transition state, OH remains weakly adsorbing on the hexagonal ring as can be seen from the electron density distribution because the C-O distance elongates from 1.51 Å to about 2.45 Å.

**Graphene edge [92]**

The edge states could be highly sensitive to variations in the edge chemistry owing to the relatively-high electron density at graphene edges. For example, the electronic structure of graphene nanodots is very sensitive to chemical terminations on the zigzag edges due to the relatively-high spin density. Chemically-modified edges exhibit metal-to-insulator transition, energy-gap variations of AGNRs, low-bias transport, enhanced half-metallicity of AGNRs [93-95]. The electronic structure is found to depend on terminated species uniquely.

The terminations of graphene nanodots described here include H, fluorine (F), and O atoms as well as OH and methyl ($CH_3$) functional groups. The initial bond length between all carbon atoms in the graphene nanodots is 1.42 Å which is the bond length of two-dimensional graphene. The geometrical structures of graphene nanodots are planar except the H atoms in OH and $CH_3$ functional groups. The optimized C-C bond lengths are ranging from 1.36 Å to 1.46 Å with the central bonds longer than the edge ones. The optimized distances between edge C atom and the saturating atoms are 1.08, 1.36, 1.29, 1.35-1.41, and 1.52 Å for H, F, O, OH, and $CH_3$, respectively.

The energy of the spin-polarized singlet state for the graphene nanodots with each termination is lower than those of both the triplet and spin-unpolarized singlet states. Thus, the ground state remains a spin-polarized singlet state even if the zigzag edges are saturated with different atoms or molecules. In addition, both the spin-polarized singlet and triplet states of the OH-terminated edge have the almost same energy, which makes the magnetic ordering easy to be detected. Meanwhile, the stability of the F-terminated edge is similar to that of the H-terminated one, while O- and $CH_3$-terminated edges are more stable than H-terminated one.

Furthermore, several other characteristics are observed in spin-density distributions of the ground state. First of all, while the spin arrangement on adjacent atoms is antiferromagnetic for H, F, OH, and $CH_3$ terminations, a mixed configuration of magnetic ordering appears at the ketonated edge. Both up- and down-spin waves can be seen in the same zigzag edge terminated with O atoms. On each zigzag edge, a half of the edge sustains having the up-spin wave and the other half are governed with the down-spin wave. For the one-dimensional graphene nanoribbon with ketonated edge, the magnetic ordering is antiferromagnetic on both edges unlike in the case of the graphene nanodots [93]. This difference is attributed to a weaker effective spin correlation due to a finite-size effect.

Additionally, such different terminations can significantly change the spin densities of the C atoms on the zigzag edges. For the $CH_3$ termination, while the largest local magnetic moments of C atoms ($M_C$) on zigzag edges is larger, that of terminal $CH_3$ molecule ($M_X$) is smaller in comparison with the H termination. On the other hand, F-, O-, and OH-terminated edges have smaller $M_C$ and larger $M_X$ compared to the H-terminated one. These differences are caused by charge transfer between edge C atoms and terminated atoms or molecules owing to differences in electronegativity. For example, the F atom which is more electronegative than the H atom attracts more charge (electron/spin) from the C atoms, which leads to larger magnetic moments of F atoms than H atoms.

### 1.3.3 Properties of defective graphene

***Chemical properties***

Intrinsically, defects with dangling bonds should enhance the reactivity of graphene. Theoretical simulations indicate that hydroxyl, carboxyl, or other groups can easily be formed on this type of defects such as vacancies and edges which are normally saturated with H atoms [96,97]. Additionally, reconstruction of defects without dangling bonds such as SW defects or vacancies locally change the density of $\pi$ electrons, which may also induce the enhanced local reactivity [96,98,99]. Indeed, reconstructed vacancies can be a trapping site of metal atoms [100]. Thus, highly-selective creation of defects in graphitic structures is useful for local functionalization, development of electrical contacts with metal electrodes, and design of chemically-modified graphene ribbons with various properties.

***Electronic properties***

Point and line defects in graphitic structures significantly affect their electronic structures and may make an avenue forward development of graphene-based electronics [68,75,101-104]. A kind of protrusions in STM images show that point defects give rise to localized states near the Fermi energy in $sp^2$ bond networks [68]. Some vacancy-type and SW defects can open a local bandgap (up to 0.3 eV) in graphene, which may play a quite important role for engineering of the local electronic structure with defect mediation [98]. For nanoribbons, SW defects can create new states in the band structure and control their energy position depending on the location with respect to ribbon edges and the density of the defects [96]. Line defects composed of non-hexagonal rings

should induce localized electronic states aligned along the line, which can enhance the conductivity along the line due to a larger number of conducting channels [75]. As a real system, the electronic transport through grain boundaries in polycrystalline graphene is important. Reflection or perfect transmission of charge carriers has been predicted for these grain boundaries consisting of periodic arrays of dislocations [104].

Doping of graphene to modify the electronic properties can be carried out usually in two ways. One is self-doping caused by intrinsic defects which lead to a slight electron-hole asymmetry in graphene [101,105]. The asymmetry changes the Fermi energy of point defects as well as line defects and results in an injection of charge into the whole electron system. Such a self-doping has experimentally been done for line defects such as rows of pentagons and octagons which may act as conducting metallic wires [75].

The other is doping by foreign species which has already been demonstrated in several ways. Metal contacts or organic molecule adsorption on graphene enable us to inject charge into the electron system [106-108]. Although the organic species weakly adsorb and desorb at temperatures below 100°C, the localization of dopants can occur on reactive defects in graphene [109]. Foreign atoms on substitutional sites on graphene are unfavorable because the electronic properties can degrade due to the strong scattering of the conduction electrons [101,110]. Nevertheless, the foreign dopant atoms are easy to be firmly attached on reconstructed defects [100].

***Magnetic properties***

Calculations in theory indicate that magnetic behaviors in graphitic systems could be attributed to graphitic defects such as vacancies, interstitials, carbon adatoms, and

atoms at the edges of graphitic nanofragments with dangling bonds [35,111-113]. Such defects possess local magnetic moments and may give rise to flat bands, which can eventually develop magnetic ordering. Impurity atoms such as H or N atoms are nonmagnetic by themselves, but for the specific chemical environment, give rise to local magnetic moments. However, no ferromagnetism on magnetized graphene nanocrystals is obtained at any temperature down to 2 K [114]. No strong paramagnetism has been observed in graphene even with the large amount of edge defects. Instead, similarly to graphite, graphene shows strong diamagnetic behavior at above 50 K. In addition, a relatively weak paramagnetic behavior at lower temperatures may be caused by the magnetic moments at the edges of small graphene crystallites. Overall, it is necessary to understand the expression mechanism of the observed magnetism in carbon systems such as graphene.

### 1.3.4 Graphene oxide and its applications

Graphene oxide (GO) is one of best examples of defective graphene, which attracts much attention in recent years. GO is an oxidized graphene sheet with several oxygenated functional groups on the basal planes and at the edges, resulting in a hybrid structure comprising a mixture of $sp^2$ and $sp^3$ C-C bonds [115]. Hydroxyl and epoxy functional groups are formed on the plane surface of GO while carbonyl and carboxyl groups are formed at the edges [116,117]. However, a complete model to determine the exact ratio and spatial distribution of the functional groups has yet to be established [118-120]. Such functional groups make GO sheets strongly hydrophilic and reduce the interaction energy between the graphene layers which increases the interlayer distance from 0.34 nm in graphite to 0.70 nm in oxidized graphite [121,122]. Hence, graphite oxide can be readily exfoliated into GO sheets [123].

It is well known that GO is a promising precursor for synthesis of graphene sheets by chemical and thermal reduction techniques [124]. It is noteworthy that GO can be useful to several applications in various fields such as optoelectronics, supercapacitors, memory devices, composite materials, photocatalysis, and drug delivery agents [125-128]. Most of the characteristic properties of GO arise from its hybrid electronic structure induced by containing both the conducting $\pi$ states in the $sp^2$ and less-conducting $\sigma$ states in the $sp^3$ domains [129]. Theoretical studies show that the electronic properties of GO can be controlled by tuning the $sp^2/sp^3$ ratios [130].

In recent studies, GO shows promise for biological applications including biosensors due to its superior properties such as high quenching efficiency, good water dispersibility, and biocompatibility [131-138]. In particular, the efficient quenching

property of GO can develop fluorescent biosensors for the detection of DNA, adenosine-5′-triphosphate (ATP), reactive oxygen species (ROS), metal ions, and proteins [132,139-143]. These GO-based biosensors can improve the sensitivity and selectivity due to the unique identification ability of GO for different biomolecules and the ultrahigh fluorescent quenching property.

For example, a fluorescent biosensor for the analysis of peptide−receptor interactions for understanding functions of proteins in cells has been developed using GO and fluorescein isothiocyanate (FITC)-labeled octreotide (FOC) [144]. FOC has a high adsorption affinity for GO, which leads to an efficient fluorescence quenching of FITC. In addition, the specific interaction between the antibody anti-octreotide (AOC) and FOC leads to releases of FOC from the GO surface, which results in the recovery of fluorescence. AOC can be detected with a low detection limit of 2 ng/mL employing this GO-based fluorescent platform. This GO-FOC biosensor has also demonstrated the specific imaging ability for receptors in AR42J cells which is one of rat pancreatic cells in comparison with a Chinese hamster ovary cell line. The GO-based biological sensing shows high promise for molecular imaging in cancer diagnosis.

## 1.4 Oxidative processes for graphitic structures

Oxidation is one of fundamental and important reactions for graphene and graphite with respect to chemisorption leading graphene or graphite oxides and etchings inducing some defects and modulated system size. The chemical and crystallographic modifications of graphene or graphite affect the mechanical, chemical, electrical, optical, and magnetic properties. In this section, typical cases of chemisorption and etching processes are explained.

**Chemisorption**

As one of basic and simple cases, oxygen (O) atoms are considered here. O atoms bind to the graphene plane in bridge position over the C-C bonds and form epoxy groups as described in Section 1.3.2 [118,121,145-149]. It has been theoretically shown by some calculations that in the three-member epoxy ring, the length of the C-C bond increases from 1.42 to 1.51-1.58 Å, which is close to the $sp^3$ bond length in a diamond structure [147,148,150,151]. Spin-singlet and spin-triplet epoxide structures are optimized to be with adsorption energies of 1.91 and 1.56 eV, respectively. The epoxy groups can interact at a coverage of up to 50%, and epoxy clustering is energetically favored even if they are randomly distributed [121,148].

Density functional theory (DFT) suggests structural models, in which two epoxy groups on one hexagonal ring cannot bind to the same C atom. When two epoxy groups are formed on the opposite C-C bonds with reference to the symmetrical axis, the binding force of one epoxy group increases the binding of the other, which induces unzipping and breaks the C-C bonds.

Some researchers have experimentally discussed about such atomic oxygen chemisorption on a graphene plane [152]. The highly oriented pyrolitic graphite (HOPG) surface exposed to O atoms generated by a radio frequency (rf) plasma has been evaluated by XPS analyses of the C 1s and O 1s photoelectron spectra. In the C 1s spectra, a broader component arising from the C-C bonds surrounding or close to the chemisorbed O atoms drastically increases at an oxidation time, $t_{ox}$, of up to 6 min, but then gradually decreases [151,153,154]. This behavior indicates that at first, perturbation of the C-C bonds occurs due to O chemisorption and leads an expansion of the oxidized domains, and then, the perturbed C-C bonds progressively transform into C-O bonds.

The components corresponding to epoxy groups appear in C 1s and O 1s peaks at $t_{ox}$ = 3 min, which means formation of epoxy groups on the surface of HOPG [153,155-157]. Peaks assigned as in-plane C-O-C ether bonds can be clearly observed in both C 1s and O1s peaks with progressing the oxidation [153,157,158]. The C=O and O-C=O bonds are notably formed at $t_{ox}$ = 21 min or longer $t_{ox}$, likely in semiquinones, carbonyls, and lactone groups. These types of oxides also correspond to the component in the O 1s spectrum caused by the C=O bonds.

For more oxidized samples, the C 1s component emerges in relation to C atoms surrounding bare and oxidized vacancies [153]. A long exposure to the oxygen plasma can induce the proliferation of vacancies due to erosions of the oxidized $sp^2$ lattice occurred by the energetic atoms and ions even at room temperature (RT). On the other hand, the O 1s spectra suggest that while at low O coverage, the bridge sites over the C-C bonds for O atoms exclusively form epoxy groups, the relative concentration of ether groups increases considerably with increasing the O coverage [155,156]. Such

ether groups can be formed on the graphene plane including seven-membered or larger-membered rings through likely unzipping processes and on the vacancies and edges with uncoordinated C atoms. The increase of the ether concentration may be related to a simultaneous increase in the number of semiquinones due to the oxidation of defects, as both groups quickly saturate vacancies [153,159].

Both ethers and semiquinones on defected graphene are accessible adsorption sites comparable with epoxy sites. In fact, no C=O bond at up to $t_{ox}$ = 15 min suggests that the observed ether groups are caused by not defect oxidation but unzipping processes. The unzipped C-O-C bonds are created by a local strain induced by the adsorbed O atoms [160]. Although oxygen diffusion hardly occurs at RT, long exposures to O atoms increase the probability for the formation of additional epoxy groups on the graphene plane with other epoxy groups, which induces the precursors for unzipping [150,161].

Some theoretical studies have shown the effects of oxidized zigzag edges on the electronic properties and relative stabilities of ZGNRs [93]. Figure 1.9 shows different edge oxidation schemes of ZGNRs with a width of 1.8 nm terminated with hydroxyl, lactone, ketone, and ether functional groups at the edges. The relative stability of the ground states of each oxidized zigzag edge has been compared by defining and calculating a Gibbs free energy of formation. The energies for the fully hydrogenated and etherated ZGNRs are found to be positive, which means less stable than their corresponding constituents. In contrast, the energies for the ZGNRs terminated with hydroxyl, lactone, and ketone functional groups are negative resulting in considerable energetic stabilization of the structure of the GNRs. Among these oxidized zigzag edges, the fully hydroxylated one is the most stable, which is attributed to the hydrogen bonds

formed between adjacent hydroxyl groups.

Table 1.1 shows the energy band gaps for hydrogenated ZGNRs and oxidized ZGNRs with relative high stability except those with ether functional groups. The hydroxylated and lactonized ZGNRs have energy band gaps comparable to the fully hydrogenated one, which indicates that the oxidation of the edges only slightly changes the electronic band structures of ZGNRs. However, the half-metallic characteristics of the ketonated ZGNRs almost vanish. Consequently, such edge oxidation plays an important role for realizing efficient and robust spintronic devices based on GNRs.

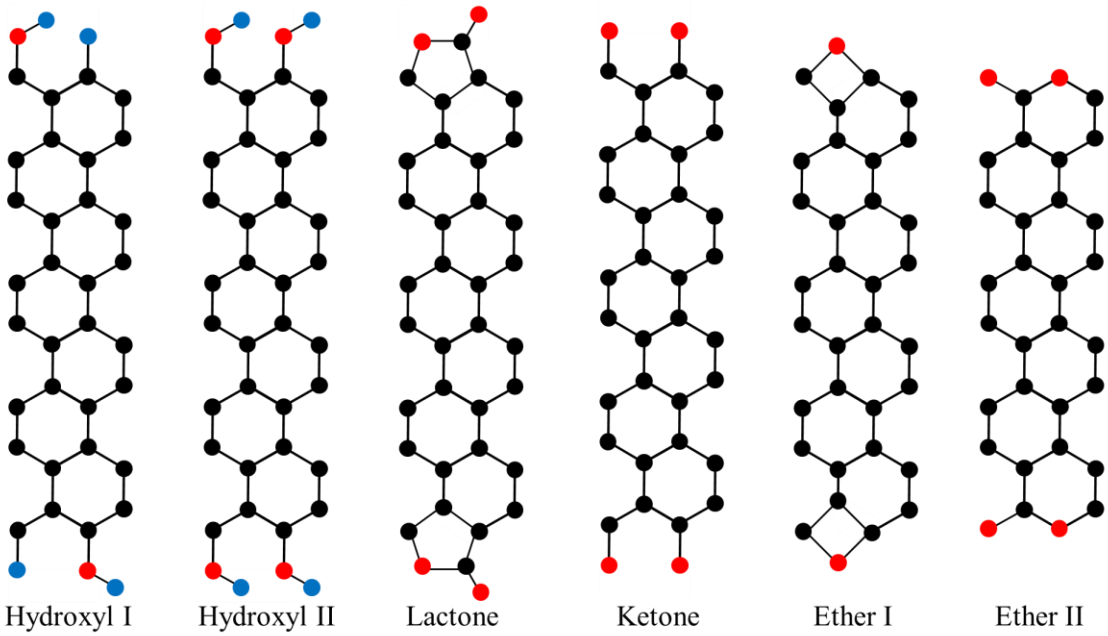


Fig. 1.9. Optimized unit cell geometries of different edge oxidation schemes [124].

Table 1.1. Energy band gaps of ZGNRs with termination of different functional groups in antiferromagnetic ground states [124].

| Terminating functional groups | Energy band gap (eV) |
|---|---|
| Hydrogen | 1.05 |
| Hydroxyl I | 0.99 |
| Hydroxyl II | 0.90 |
| Lactone | 0.77 |
| Ketone | 0.03 |

**Formation of $CO/CO_2$ and etching**

Thermal reduction processes of graphite and graphene oxides are one of fundamental thermodynamics for graphitic materials, which leads induction of some defects and etchings of graphitic structures. For example, epoxy groups on graphene surfaces resulting from exposure to atomic oxygen as described above can thermally form molecular $CO/CO_2$. A single epoxy group as an initial state finally forms an unsaturated vacancy and a CO molecule released into the gas phase. This reaction is strongly endothermic (6.31 eV) which means that the resulting dangling bonds are a final state with the high energy because C atoms surrounding a single vacancy in the basal plane are relatively stable [162,163].

When a second O atom contributes to the reaction, the defective surface becomes a state with a lower energy due to partial saturation of the three dangling bonds in the vacancy, which also results in the endothermic reaction (0.70 eV). When a third O atom participates into the reaction, two epoxy groups can now fully saturate all the dangling bonds in a vacancy induced by formation of CO, which is strongly exothermic (-2.48 eV). The hexagonal rings are reconstructed to a defective graphene region of a semiquinone and an ether functional group, which is the stable configuration involving two O atoms and a C vacancy on graphene.

On the other hand, two neighboring epoxy groups as an initial state form an unsaturated vacancy and a $CO_2$ molecule released into the gas phase, which is also a strongly-endothermic reaction with 2.43 eV. When a third O atom contributes to the reaction, it becomes strongly exothermic (-2.90 eV) due to a vacancy partially saturated by an O atom. As is the case in the CO formation, four O adatoms on graphene plane lead to the reaction with more than 6 eV in favor of the products because the vacancy

can be fully saturated by the semiquinone and ether functional groups.

The above oxidation processes through the formation of $CO/CO_2$ molecules in the gas phase lead to some kinds of etchings of graphitic structures. The graphite lattice has a highly anisotropic crystallographic structure, which makes the etching reaction dependent on the lattice direction. For instance, a systematic kinetic study of the oxidative etching of graphite basal planes along the *a* and *c* directions at temperatures up to 950˚C has been reported using STM [164]. Thermal oxidation of graphite in dry air at 550-950˚C forms pits by layer-by-layer etching of the layered structure. Circular pits with the uniform size are formed on the sites of point defects at temperatures below 875˚C. In contrast, the formation of pits occurs on both defected and basal plane at temperatures above 875˚C. However, vertical etchings inducing pits contacting with next-layer pits hardly occur.

As a result, the lateral etch rate is three orders of magnitude faster than the vertical etch rate because vacancies on graphite surface increase in the local electronic density near the Fermi level in the atoms surrounding the vacancy, which can enhance the reactivity of such dangling bonds. Furthermore, as the thermal energy at high temperatures enables the oxygen species to migrate faster on the graphene surface and frequently collide with the C atoms on the surface, the etch rate increases with increasing temperature. It should be noted that at the relatively higher temperatures, $O_2$, $H_2O$, and $CO_2$ in air can easily be dissociated into O atoms [165-168]. Accordingly, the etchings are consistent with the theoretical study on the formation of a vacancy and $CO/CO_2$ molecules depending on the number of O atom contributing to the reaction, which corresponds to the dependence of the frequency factor discussed experimentally.

## 1.5 Objective and composition of this thesis

Surface reactions with reactive and energetic species in graphitic structures can critically modify the crystalline structures with respect to crystallography and chemistry due to introduction of various defects. Therefore, understanding of the reaction mechanism and its control are absolutely necessary, in particular, for CNWs in which there are intrinsically various structural fluctuations including characteristic nanostructures and graphitic defects.

Oxidation is a reaction process most readily occurring in carbon materials and can effectively change their structures. Accordingly, oxidation is expected to be one of promising techniques to control the crystallographic and chemical states of CNWs for modifying their electronic structure, chemical properties, and magnetic properties. Concretely, the oxidative chemisorption can induce chemically-modified edges and planes, which may result in GO nanostructures. Furthermore, the formation of defects and control of its states are also addressed through oxidation processes. Oxidative etchings will enable us to control the size of the graphitic system and thickness of the walls corresponding to the number of graphene sheets.

These structural modifications are expected to control the electronic properties toward realization of carbon nanoelectronics, high-efficiency optical devices, and highly-sensitive biosensors. However, oxidation processes in the complicated crystalline structures of CNWs have not been clarified yet. Moreover, no selective oxidation technique of graphitic structures including various defects has been established while there are a lot of theoretical studies on the oxidation reactions. In this thesis, the

oxidation processes in CNWs under some different oxidative conditions were investigated. In addition, the selectivity of the oxidation of the edges and wall surfaces in CNWs was also discussed by focusing on each morphological and chemical change.

The structures and properties of carbon nanomaterials are described in Section 1.1. Then, CNWs consisting of vertically-aligned graphene sheets have characteristic structural features and exhibit unique electronic properties. In Section 1.2, previous studies on control of the structural parameters during the growth and after the growth are described. Especially, graphitic defects in CNWs are one of critical factors in affecting the electronic properties. Section 1.3 refers to various graphitic defects such as crystallographically- and chemically-reconstructed hexagonal rings in graphene and its effects on properties. The oxidation is one of fundamental and important reactions to control the graphitic structures including defects. In Section 1.4, the oxidative chemisorption and etching of graphene or graphite are described based on theoretical and experimental analyses. As one of promising states of oxidized graphene, GO possesses excellent properties such as quenching properties and is one of promising candidates for applications in various field such as biosensors.

In Chapter 2, two main plasma processing systems are described, in which one is for synthesis of CNWs and the other is for post-growth treatment of them. CNWs were synthesized using plasma-enhanced CVD (PECVD) with hydrogen radical injection and the PECVD system is called RI-PECVD system. The CNWs were treated using multi-beam plasma irradiation system which consists of two remote plasma sources. Various evaluation methods of the treated CNWs are also described.

In Chapter 3, the effects of atomic oxygen (O) exposure to CNWs are described as one of fundamental oxidative processes. As there are various graphitic defects in both

graphene edges and planes in the CNWs, it is important to clarify the oxidative contributions of O atoms to the crystalline structures of CNWs. Furthermore, to also clarify the dependence of the effects of O treatment on the crystallinity of CNWs, two types of CNWs which have quite different crystallinities were prepared with $C_2F_6/H_2$ and $CH_4/H_2$ plasmas and exposed to O atoms.

In Chapter 4, the independent or synergetic effects of ions on the reactions of radicals including O atoms in an $O_2$ plasma are described. The reactive ion etching using capacitively-coupled $O_2$ plasma was carried out and compared with the O treatment. Then, to focus on the effects of limited species and control them, CNWs were irradiated with O atoms and Ar ions independently generated using the multi-beam plasma irradiation system. In particular, with a view to selectively control the oxidative reactions on the edges and wall surfaces in CNWs, the ion irradiated area was controlled by changing the incident angle to the substrate.

In Chapter 5, the effects of radicals in hydrogen peroxide ($H_2O_2$) solution on the surface morphologies and chemistry of CNWs are described as effects of molecular oxidative radicals and active oxygen species (AOS). To observe the oxidation process on a typical graphene surface, graphite was also treated with $H_2O_2$ solution and compared with the CNWs. Moreover, the subsequent O treatment after the $H_2O_2$ treatment contributes to not only clarify the reaction mechanism but also suggest possible applied treatments.

Finally, the results and discussion in the present study are summarized, and the future scopes are described in Chapter 6.

# References

[1] Tanso zairyou gakkai "*Shin Tansozairyou Nyumon*, [New carbon materials introductory book]" Realize Science & Engineering, Tokyo, 1996. [in Japanese]

[2] 2007 International Technology Roadmap for Semiconductors, *Executive Summary*.

[3] A. K. Geim and K. S. Novoselov: Nat. Mater. **6** (2007) 183.

[4] H. W. Kroto, J. R. Heath, S. C. O'brien, R. F. Curl, and R. E. Smally: Nature **318** (1985) 163.

[5] E. Ozawa: Kagaku **25** (1970) 854.

[6] S. Iijima: Nature **354** (1991) 56.

[7] T. Durkop, S. A. Getty, E. Cobas, and M. S. Fuhrer: Nano Lett. **4** (2004) 35.

[8] C. Berger, Y. Yi, Z. L. Wang, W. A. de Heer: Appl. Phys. A **74** (2002) 363.

[9] L. X. Zheng, M. J. O'Connell, S. K. Doorn, X. Z. Liao, Y. H. Zhao, E. A. Akhadov, M. A. Hoffbauer, B. J. Roop, Q. X. Jia, R. C. Dye, D. E. Peterson, S. M. Huang, J. Liu, and Y. T. Zhu: Nat. Mater. **3** (2004) 673.

[10] P. M. Ajayan: Chem. Rev. **99** (1999) 1787.

[11] R. H. Baughman, C. Cui, A. A. Zakhidov, Z. Iqbal, J. N. Barisci, G. M. Spinks, G. G. Wallace, A. Mazzoldi, D. De Rossi, A. G. Rinzler, O. Jaschinski, S. Roth, and M. Kertesz: Science **21** (1999) 1340.

[12] A. C. Dillon, K. M. Jones, T. A. Bekkedahl, C. H. Kiang, D. S. Bethune, M. J. Heben: Nature **386** (1997) 377.

[13] B. Gao, A. Kleinhammes, X. P. Tang, C. Bower, L. Fleming, Y. Wu, O. Zhou: Chem. Phys. Lett. **307** (1999) 153.

[14] C. Niu, E. K. Sichel, R. Hoch, D. Moy, and H. Tennent: Appl. Phys. Lett. **70** (1997) 1480.

[15] E. Frackowiak, K. Metenier, V. Bertagna, and F. Beguin: Appl. Phys. Lett. **77** (2000) 2421.

[16] S. Iijima and T. Ichihashi: Nature **363** (1993) 603.

[17] C. Journet, W. K. Maser, P. Bernier, A. Loiseau, M. Lamy de la Chapelle, S. Lefrant, P. Deniard, R. Lee, J. E. Fischer: Nature **388** (1997) 756.

[18] A. Thess, R. Lee, P. Nikolaev, H. Dai, P. Petit, J. Robert, C. Xu, Y. H. Lee, S. G. Kim, A. G. Rinzler, D. T. Colbert, G. E. Scuseria, D. Tománek, J. E. Fischer, and R. E. Smalley: Science **273** (1996) 483.

[19] A. M. Cassell, J. A. Raymakers, J. Kong, and H. Dai: J. Phys. Chem. B **103** (1999) 6484.

[20] A. Javey, J. Guo, Q. Wang, M. Lundstrom, and H. Dai: Nature **424** (2003) 654.

[21]http://upload.wikimedia.org/wikipedia/commons/5/53/Types_of_Carbon_Nanotubes.png

[22] J. Kong, N.R. Franklin, C. Zhou, M.G. Chapline, S. Peng, K. Cho, and H. Dai: Science **287** (2000) 622.

[23] Y. Kobayashi, K. Fukui, T. Enoki, K. Kusakabe, and Y. Kaburagi: Phys. Rev B **71** (1996) 193406.

[24] K. Nakada, M. Fujita, G. Dresselhaus, and M. S. Dresselhaus: Phys. Rev. B **54** (1996) 17954.

[25] M. Fujita, K. Wakabayashi, K. Nakada, and K. Kusakabe1: J. Phys. Soc. Jpn. **65** (1996) 1920.

[26] K. S. Novoselov, A. K. Geim, S. V. Morozov, D. Jiang, Y. Zhang, S. V. Dubonos, I.

V. Grigorieva, and A. A. Firsov: Science **306** (2004) 666.

[27] K. S. Novoselov, A. K. Geim, S. V. Morozov, D. Jiang, M. I. Katsnelson, I. V. Grigorieva, S. V. Dubonos, and A. A. Firsov: Nature **438** (2005) 197.

[28] Y. Zhang, Y.-W Tan, H. L. Stormer, and P. Kim: Nature **438** (2005) 201.

[29] Y.-W Son, M. L. Cohen, and S. G. Louie: Phys. Rev. Lett. **97** (2006) 216803.

[30] O. Hod, J. E. Peralta, and G. E. Scuseria: Phys. Rev. B **76** (2007) 233401.

[31] T. Fang, A. Konar, H. Xing, and D. Jena: Appl. Phys. Lett. **91** (2007) 092109.

[32] D. Finkenstadt, G. Pennington, and M. J. Mehl1: Phys. Rev. B **76** (2007) 121405(R).

[33] P, Shemella, Y, Zhang, M, Mailman, P. M. Ajayan, and S. K. Nayak: Appl. Phys. Lett. **91** (2007) 042101.

[34] H. Lee, Y.-W Son, N. Park, S. Han, and J. Yu: Phys. Rev. B **72** (2005) 174431.

[35] Y.-W Son, M. L. Cohen, and S. G. Louie: Nature **444** (2006) 347.

[36] Y.-W Son, M. L. Cohen, and S. G. Louie: Phys. Rev. Lett. **97** (2006) 216803.

[37] E.-J Kan, Z. Li, J. Yang, and J. G. Hou: Appl. Phys. Lett. **91** (2007) 243116.

[38] D. Jiang, B. G. Sumpter, and S. Dai: J. Chem. Phys. **126** (2007) 134701.

[39] M. Hiramatsu, K. Shiji, H. Amano and M. Hori: Appl. Phys. Lett. **84** (2004) 4708.

[40] M. Hiramatsu and M. Hori: Jpn. J. Appl. Phys. **45** (2006) 522.

[41] K. Kobayashi, M. Tanimura, H. Nakai, A. Yoshimura, H. Yoshimura, K. Kojima, and M. Tachibana: J. Appl. Phys. **101** (2007) 094306.

[42] J. A. Carlisle, S. R. Blankenship, L. J. Terminello, J. J. Jia, T. A. Callcott, D. L. Ederer, R. C. C. Perera, and F. J. Himpsel: J. Electron Spectrosc. Relat. Phenom. **110-111** (2000) 323.

[43] H. Kondo, W. Takeuchi, M. Hori, S. Kimura, Y. Kato, T. Muro, T. Kinoshita, O.

Sakata, H. Tajiri, and M. Hiramatsu: Appl. Phys. Lett. **99** (2011) 213110.

[44] V. Barone, O. Hod, and G. E. Scuseria: Nano Lett. **6** (2006) 2748.

[45] J. W. G. Wildöer, L. C. Venema, A. G. Rinzler, R. E. Smalley, and C. Dekker: Nature **391** (1998) 59.

[46] W. Takeuchi, K. Takeda, M. Hiramatsu, Y. Tokuda, H. Kano, S. Kimura, O. Sakata, H. Tajiri, and M. Hori: Phys. Status Solidi **207** (2010) 139.

[47] W. Takeuchi, M. Ura, M. Hiramatsu, Y. Tokuda, H. Kano, and M. Hori: Appl. Phys. Lett. **92** (2008) 213103.

[48] S. Kawai, S. Kondo, W. Takeuchi, H. Kondo, M. Hiramatsu, and M. Hori: Jpn. J. Appl. Phys. **49** (2010) 060220.

[49] W. Takeuchi, H. Kondo, T. Obayashi, M. Hiramatsu, and M. Hori: Appl. Phys. Lett. **98** (2011) 123107.

[50] T. Machino, W. Takeuchi, H. Kano, M. Hiramatsu,a and M. Hori: Appl. Phys. Express **2** (2009) 025001.

[51] K. Mase, H. Kondo, S. Kondo, M. Hori, M. Hiramatsu, and H. Kano: Appl. Phys. Lett. **98** (2011) 193108.

[52] T. Horibe, H. Kondo, K. Ishikawa, H. Kano, M. Sekine, M. Hiramatsu, and M. Hori: Appl. Phys. Express **6** (2013) 045103.

[53] S. Kondo, S. Kawai, W. Takeuchi, K. Yamakawa, S. Den, H. Kano, M. Hiramatsu, and M. Hori: J. Appl. Phys. **106** (2009) 094302.

[54] S. Kondo, H. Kondo, M. Hiramatsu, M. Sekine, and M. Hori: Appl. Phys. Express **3** (2010) 045102.

[55] H. Yoshimura, S. Yamada, A. Yoshimura, I. Hirosawa, K. Kojima, and M. Tachibana: Chem. Phys. Lett. **482** (2009) 125.

[56] S. Suzuki, A. Chatterjee, C. L. Cheng, and M. Yoshimura: Jpn. J. Appl. Phys. **50** (2011) 01AF08.

[57] S. Shimabukuro, Y. Hatakeyama, M. Takeuchi, T. Itoh, and S. Nonomura: Thin Solid Films **516** (2008) 710.

[58] H. Watanabe, H. Kondo, M. Sekine, M. Hiramatsu, and M. Hori: Jpn. J. Appl. Phys. **51** (2012) 01AJ07.

[59] H. Watanabe, H. Kondo, M. Hiramatsu, M. Sekine, S. Kumar, K. Ostrikov, and M. Hori: Plasma Process. Polym. **10** (2013) 582.

[60] S. Kondo, H. Kondo, Y. Miyawaki, H. Sasaki, H. Kano, M. Hiramatsu, and M. Hori: Jpn. J. Appl. Phys. **50** (2011) 075101.

[61] A. Achour, S. Vizireanu, G. Dinescu, L. Le Brizoual, M.-A. Djouadi, and M. Boujtita: Appl. Surf. Sci. **273** (2013) 49.

[62] F. Banhart, J. Kotakoski, and A. V. Krasheninnikov: ACS Nano **5** 26 (2011).

[63] A. J. Stone and D. J. Wales: Chem. Phys. Lett. **128** (1986) 501.

[64] L. Li, S. Reich, and J. Rovertson: Phys. Rev. B **72** (2005) 184109.

[65] J. Ma, D. Alfé, A. Michaelides, and E. Wang: Phys. Rev. B **80** (2009) 033407.

[66] M. H. Gass, U. Bangert, A. L. Bleloch, P. Wang, R. R. Nair, and A. K. Geim: Nat. Nanotechnol. **3** (2008) 676.

[67] J. C. Meyer, C. Kisielowski, R. Erni, M. D. Rossell, M. F. Crommie, and A. Zettl: Nano Lett. **8** (2008) 3582.

[68] M. M. Ugeda, I. Brihuega, F. Guinea, and J. M. Gómez-Rodríguez: Phys. Rev. Lett. **104** (2010) 096804.

[69] A. V. Krasheninnikov, P. O. Lehtinen, A. S. Foster, and R. M. Nieminen: Chem. Phys. Lett. **418** (2006) 132.

[70] A. A. El-Barbary, R. H. Telling, C. P. Ewels, M. I. Heggie, and P. R. Briddon: Phys. Rev. B **68** (2003) 144107.

[71] G.-D. Lee, C. Z. Wang, E. Yoon, N.-M. Hwang, D.-Y. Kim, and K. M. Ho: Phys. Rev. Lett. **95** (2005) 205501.

[72] A. Hashimoto, K. Suenaga, A. Gloter, K. Urita, and S. Iijima: Nature **430** (2004) 870.

[73] J. Coraux, A. T. N'Diaye, C. Busse, and T. Michely: Nano Lett. **8** (2008) 565.

[74] J. Červenka, M. I. Katsnelson, and C. F. J. Flipse, Nat. Phys. **5** (2009) 840.

[75] J. Lahiri, Y. Lin, P. Bozkurt, I. I. Oleynik, and M. Batzill: Nat. Nanotechnol. **5** (2010) 326.

[76] B. W. Jeong, J. Ihm, and G.-D. Lee: Phys. Rev. B **78** (2008) 165403.

[77] O. V. Yazyev and S. G. Louie: Phys. Rev. B **81** (2010) 195420.

[78] S. Malola, H. Häkkinen, and P. Koskinen: Phys. Rev. B **81** (2010) 165447.

[79] P. Koskinen, S. Malola, and H. Häkkinen: Phys. Rev. Lett. **101** (2008) 115502.

[80] P. Koskinen, S. Malola, and H. Häkkinen: Phys. Rev. B **80** (2009) 073401.

[81] Ç. Ö. Girit, J. C. Meyer, R. Erni, M. D. Rossell, C. Kisielowski, L. Yang, C.-H. Park, M. F. Crommie, M. L. Cohen, S. G. Louie, and A. Zettl: Science **323** (2009) 1705.

[82] L. Chen, H. Hu, Y. Ouyang, H. Z. Pan, Y. Y. Sun, and F. Liu: Carbon **49** (2011) 3356.

[83] D. C. Sorescu, K. D. Jordan, and P. Avouris: J. Phys. Chem. B **105** (2001) 11227.

[84] N. Ghaderi and M Peressi: J. Phys. Chem. C **114** (2010) 21625.

[85] D. Yu and F. Liu: Nano Lett. **7** (2007) 3046.

[86] Z. F. Wang, Y. Zhang, and F. Liu: Phys. Rev. B **83** (2011) 041403.

[87] E. J. Duplock and M. Scheffler: Phys. Rev. Lett. **92** (2004) 225502.

[88] X. T. Zhou, T. K. Sham, Y. Wu, Y. M. Chong, I. Bello, S. T. Lee, F. Heigl, T. Regier, and R. I. R. Blyth: J. Am. Chem. Soc. **129** (2007) 1476.

[89] H. He, J. Klinowski, M. Forster, and A. Lerf: Chem. Phys. Lett. **287** (1998) 53.

[90] Y. Ferro, D. Teillet-Billy, N. Rougeau, V. Sidis, S. Morisset, and A. Allouche: Phys. Rev. B **78** (2008) 085417.

[91] S. Casolo, O. M. Lovvik, R. Martinazzo, and G. F. Tantardini: J. Chem. Phys. **130** (2009) 054704.

[92] H. Zheng and W. Duley: Phys. Rev. B **78** (2008) 045421.

[93] O. Hod, V. Barone, J. E. Peralta, and G. E. Scuseria: Nano Lett. **7** (2007) 2295.

[94] Z. F. Wang, Q. Li, H. Zheng, H. Ren, H. Su, Q. W. Shi, and J. Chen: Phys. Rev. B **75** (2007) 113406.

[95] D. Gunlycke, J. Li, J. W. Mintmire, and C. T. White: Appl. Phys. Lett. **91** (2007) 112108.

[96] D. W. Boukhvalov and M. I. Katsnelson: Nano Lett. **8** (2008) 4373.

[97] G. Cantele, Y.-S. Lee, D. Ninno, and N. Marzari: Nano Lett. **9** (2009) 3425.

[98] X. Peng and R. Ahuja: Nano Lett. **8** (2008) 4464.

[99] E. J. Duplock, M. Scheffler, and P. J. D. Lindan: Phys. Rev. Lett. **92** (2004) 225502.

[100] R. Anton and I. Schneidereit: Phys. Rev. B **58** (1998) 13874.

[101] A. H. Castro Neto, F. Guinea, N. M. R. Peres, K. S. Novoselov, and A. K. Geim: Rev. Mod. Phys. **81** (2009) 109.

[102] G. M. Rutter, J. N. Crain, N. P. Guisinger, T. Li, P. N. First, and J. A. Stroscio: Science **317** (2007) 219.

[103] T. G. Pedersen, C. Flindt, J. Pedersen, N. A. Mortensen, A.-P. Jauho, and K. Pedersen: Phys. Rev. Lett. **100** (2008) 136804.

[104] O. V. Yazyev and S. G. Louie: Nat. Mater. **9** (2010) 806.

[105] S. Reich, J. Maultzsch, C. Thomsen, and P. Ordejón: Phys. Rev. B **66** (2002) 035412.

[106] G. Giovanetti, P. A. Khomyakov, G. Brocks, V. M. Karpan, J. van den Brink, and P. J. Kelly: Phys. Rev. Lett. **101** (2008) 026803.

[107] T. O. Wehling, K. S. Novoselov, S. V.Morozov, E. E. Vdovin, M. I. Katsnelson, A. K. Geim, and A. I. Lichtenstein: Nano Lett. **8** (2008) 173.

[108] N. Jung, N. Kim, S. Jockusch, N. J. Turro, P. Kim, and L. Brus: Nano Lett. **9** (2009) 4133.

[109] C. Coletti, C. Riedl, D. S. Lee, B. Krauss, L. Patthey, K. von Klitzing, J. H. Smet, and U. Starke: Phys. Rev. B **81** (2010) 235401.

[110] J.-C. Charlier, X. Blase, and S. Roche: Rev. Mod. Phys. **79** (2007) 677.

[111] P. O. Lehtinen, A. S. Foster, A. Ayuela, A. V. Krasheninnikov, K. Nordlund, and R. M. Nieminen: Phys. Rev. Lett. **91** (2003) 017202.

[112] A. N. Andriotis, M. Menon, R. M. Sheetz, and L. Chernozatonskii: Phys. Rev. Lett. **90** (2003) 026801.

[113] O. V. Yazyev: Phys. Rev. Lett. **101** (2008) 037203.

[114] M. Sepioni, S. Rablen, R. R. Nair, J. Narayanan, F. Tuna, R. Winpenny, A. K. Geim, and I. V. Grigorieva: Phys. Rev. Lett. **105** (2010) 207205.

[115] D. A. Dikin, S. Stankovich, E. J. Zimney, R. D. Piner, G. H. B. Dommett, G. Evmenenko, S. T. Nguyen, and R. S. Ruoff: Nature **448** (2007) 457.

[116] J. T. Paci, T. Belytschko, and G. C. Schatz: J. Phys. Chem. C **222** (2007) 18099.

[117] J. Chattopadhyay, A. Mukherjee, C. E. Hamilton, J. Kang, S. Chakraborty, W. Guo, K. F. Kelly, A. R. Barron, and W. E. Billups: J. Am. Chem. Soc. **130** (2008) 5414.

[118] A. Lerf, H. He, M. Forster, and J. Klinowski: J. Phys. Chem. B **102** (1998) 4477.

[119] T. Szabó, O. Berkesi, P. Forgó, K. Josepovits, Y. Sanakis, D. Petridis, I. and Dékány: Chem. Mater. **18** (2006) 2740.

[120] H. He, J. Klinowski, M. Forster, and A. Lerf: Chem. Phys. Lett. **287** (1998) 53.

[121] D. W. Boukhvalov and M. I. Katsnelson: J. Am. Chem. Soc. **130** (2008) 10697.

[122] S. Stankovich, D. A. Dikin, R. D. Piner, K. A. Kohlhaas, A. Kleinhammes, Y. Jia, Y. Wu, S. T. Nguyen, and R. S. Ruoff: Carbon **45** (2007) 1558.

[123] D. Long, W. Li, L. Ling, J. Miyawaki, I. Mochida, and S.-H. Yoon: Langmuir. **26** (2010) 16096.

[124] S. Park and R. S. Ruoff: Nat. Nanotechnol. **4** (2009) 217.

[125] G. Wang, X. Sun, C. Li, and J. Lian: Appl. Phys. Lett. **99** (2011) 0531141.

[126] K. Krishnamoorthy, R. Mohan, and S.-J. Kim: Appl. Phys. Lett. **98** (2011) 2441011.

[127] U. Khan, P. May, A. O. Neill, and J. N. Coleman: Carbon **48** (2010) 4035.

[128] Q. Cheng, J. Tang, J. Ma, H. Zhang, N. Shinya, and L.-C. Qin: Carbon **49** (2011) 2917.

[129] K. P. Loh, Q. Bao, G. Eda, and M. Chhowalla: Nat. Chem. **2** (2010) 1015.

[130] H. K. Jeong, C. Yang, B. S. Kim, and K. Kim: Europhys. Lett. **92** (2010) 370051.

[131] S. J. He, B. Song, D. Li, C. F. Zhu, W. P. Qi, Y. Q. Wen, L. H. Wang, S. P. Song, H. P. Fang, and C. H. Fan: Adv. Funct. Mater. **20** (2010) 453.

[132] C. H. Lu, J. Li, X. J. Qi, X. R. Song, H. H. Yang, X. Chen, and G. N. J. Chen:

Mater. Chem. **21** (2011) 10915.

[133] X. M. Sun, Z. Liu, K. Welsher, J. T. Robinson, A. Goodwin, S. Zaric, and H. Dai: J. Nano Res. **1** (2008) 203.

[134] K. P. Loh, Q. Bao, P. K. Ang, and J. J. Yang: Mater. Chem. **20** (2010) 2277.

[135] J. W. Burress, S. Gadipelli, J. Ford, J. M. Simmons, W. Zhou, and T. Yildirim: Angew. Chem., Int. Ed. **49** (2010) 8902.

[136] S. Mao, G. H. Lu, K. H. Yu, Z. Bo, and J. H. Chen: Adv. Mater. **22** (2010) 3521.

[137] W. H. Wu, H. Y. Hu, F. Li, L. H. Wang, J. M. Gao, J. X. Lu, and C. H. Fan: Chem. Commun. **47** (2011) 1201.

[138] Z. Liu, J. T. Robinson, X. M. Sun, and H. J. J. Dai: Am. Chem. Soc. **130** (2008) 10876.

[139] C. H. Lu, J. Li, M. H. Lin, Y. W. Wang, H. H. Yang, X. Chen, and G. N. Chen: Angew. Chem., Int. Ed. **122** (2010) 8632.

[140] M. Liu, Q. Zhang, H. M. Zhao, S. Chen, H. Yu, Y. B. Zhang, and X. Quan: Chem. Commun. **47** (2011) 4084.

[141] Y. Q. Wen, F. F. Xing, S. J. He, S. P. Song, L. H. Wang, Y. T. Long, D. Li, and C. H. Fan: Chem. Commun. **46** (2010) 2596.

[142] H. X. Chang, L. H. Tang, Y. Wang, J. H. Jiang, J. H. Li: Anal. Chem. **82** (2010) 2341.

[143] L. H. Wang, K. Y. Pu, J. Li, X. Y. Qi, H. Li, H. Zhang, C. H. Fan, and B. Liu: Adv. Mater. **23** (2011) 4386.

[144] F. Bianying, G. Linjie, W. Lihua, L. Fan, L. Jianxin, G. Jimin, F. Chunhai, and H. Qing: Anal. Chem. **85** (2013) 7732.

[145] D. Lamoen and B. N. J. Persson: J. Chem. Phys. **108** (1998) 3332.

[146] A. M. Butkus, C. Y. Yang, Y. W. Tsang, and C. Y. Fong: Phys. Rev. B **26** (1982) 6853.

[147] A. Incze, A. Pasturel, and C. Chatillon: Surf. Sci. **537** (2003) 55.

[148] J.-L. Li, K. N. Kudin, M. J. McAllister, R. K. Prud'homme, I. A. Aksay, and R. Car: Phys. Rev. Lett. **96** (2006) 176101.

[149] R. J. W. E. Lahaye, H. K. Jeong, C. Y. Park, and Y. H. Lee: Phys. Rev. B **79** (2009) 125435.

[150] K. A. Mkhoyan, A. W. Contryman, J. Silcox, D. A. Stewart, G. Eda, C. Mattevi, S. Miller, and M. Chhowalla: Nano Lett. **9** (2009) 1058.

[151] J.-A. Yan and M. Y. Chou: Phys. Rev. B **82** (2010) 125403.

[152] R. Larciprete, P. Lacovig, S. Gardonio, A. Baraldi, and S. Lizzit: J. Phys. Chem. C **116** (2012) 9900.

[153] A. Barinov, O. B. Malcioglu, S. Fabris, T. Sun, L. Gregoratti, M. Dalmiglio, and M. Kiskinova: J. Phys. Chem. C **113** (2009) 9009.

[154] C. Bittencourt, C. Navio, A. Nicolay, B. Ruelle, T. Godfroid, R. Snyders, J.-F. Colomer, M. J. Lagos, X. Ke, G. Van Tendeloo, I. Suarez-Martinez, and C. P. Ewels: J. Phys. Chem. C **115** (2011) 20412.

[155] R. Larciprete, S. Fabris, T. Sun, P. Lacovig, A. Baraldi, and S. Lizzit: J. Am. Chem. Soc. **133** (2011) 17315.

[156] N. A. Vinogradov, K. Schulte, M. L. Ng, A. Mikkelsen, E. Lundgren, N. Martensson, and A. B. Preobrajenski: J. Phys. Chem. C **115** (2011) 9568.

[157] R. Larciprete, S. Gardonio, L. Petaccia, and S. Lizzit: Carbon **47** (2009) 2579.

[158] W. Zhang, V. Carravetta, Z. Li, Y. Luo, and J. Yang: J. Chem. Phys. **131** (2009) 244505.

[159] J. M. Carlsson, F. Hanke, S. Linic, and M. Scheffler: Phys. Rev. Lett. **102** (2009) 166104.

[160] T. Sun and S. Fabris: Nano Lett. **12** (2012) 17.

[161] A. Kutana and K. P. Giapis: J. Phys. Chem. C 113 (2009) 14721.

[162] T. J. Frankcombe, S. K. Bhatia, and S. C. Smith: Carbon **40** (2002) 2341.

[163] Y. Ma, P. O. Lehtinen, a. S. Foster, and R. M. Nieminen: NEW J. Phys. **6** (2004) 68.

[164] J. R. Hahn: Carbon **43** (2005) 1506.

[165] E. L. Evans, R. J. M. Griffiths, and J. M. Thomas: Science **171** (1971) 175.

[166] C. Wong and R. T. Yang: Ind. Eng. Chem. Fundam. **23** (1984) 298.

[167] R. T. Yang and K. L. Yang: Carbon **23** (1985) 537.

[168] K. L. Yang and R. T. Yang: Am. Inst. Chem. Eng. J. **31** (1985) 1313.

# Chapter 2

# Experimental setup and evaluation methods of CNWs

## 2.1 Synthesis and oxidative treatments of CNWs

Plasma-enhanced chemical vapor deposition (PECVD) has been widely applied to fabricate various kinds of material including carbon materials such as amorphous carbon (a-C) film, graphene, carbon nanotubes (CNTs), and carbon nanowalls (CNWs) as well as various silicon (Si) films such as hydrogenated amorphous Si (a-Si:H) films. These materials are synthesized by surface reactions with ions and radicals at relatively low temperature.

In a typical plasma, free electrons are accelerated by an electric field and have high energies. Chemically-reactive and energetic species are usually generated under low pressure by collisions between the energetic electrons and molecules. These active species chemically and physically interact or react with the surface atoms of the substrate. Continuous cycle of such surface reactions deposits materials on a substrate. To control the surface reactions, we should determine to control the plasma state by

changing the gas flow rates, total gas pressure, frequency of the power source, the input power, etc as parameters. The typical process carbon gases are methane ($CH_4$), ethylene ($C_2H_4$), acetylene ($C_2H_2$), $CF_4$, and $C_2F_6$ for fabrication of carbon nanomaterials. Hydrogen ($H_2$) and argon (Ar) gases are used as additional gases to alter the plasma states and directly or indirectly the reactions. Various electrical power sources with different frequencies including direct current (DC) and 13.56 MHz-2.45 GHz and pressures ranging between 1 Pa and 10 kPa (atmospheric pressure) are widely used.

Remote plasma sources are widely used for effective plasma processes such as CVD deposition, etchings, and surface treatments of films due to extraction of target species, in general, neutral species such as radicals. Furthermore, such a remote plasma is also applied as a radical source (or ion source with extraction and acceleration electrodes) to clarify surface reactions in detail. As localized and partially-limited plasmas with a relatively-high density are needed to make the remote plasma sources, inductively-coupled rf plasmas (rf-ICP) and surface-wave microwave excited plasma (SWP) are usually used.

In this study, two types of systems were used for the synthesis and treatment of CNWs. One is radical-injection plasma-enhanced chemical vapor deposition (RI-PECVD) system for the experiments of Chapters 3, 4, and 5. The other is multi-beam plasma irradiation system as a radical and ion source for the experiments of Chapters 3 and 4.

### 2.1.1 Radical injection plasma-enhanced chemical vapor deposition (RI-PECVD) of CNWs

PECVD combined with radical injection using a remote plasma source (RI-PECVD) has been proposed as a synthesis method for CNWs. Well-controlled and reproducible fabrications of CNWs have been demonstrated using fluorocarbon PECVD with hydrogen (H) radical injection from the side of the CCP region [1,2]. This RI-PECVD has been constructed based on a concept of precisely-controlling internal parameters of plasma such as an electron density, an electron temperature, radical densities, etc., which are critical factors in PECVD. The additional H radical injection source installed to the RI-PECVD system is expected to increase the amount of H radicals and control its behavior in the CCP region. Moreover, the size of electrodes of the main CCP source would be arbitrarily extended as maintaining the internal parameters.

Figure 2.1 shows the schematic diagram of RI-PECVD system. This system has a shape of tandem type consisting of a surface wave plasma (SWP) source in the upper region and a CCP source in the lower region. For the SWP source as a source of H radical injection, microwave (2.45 GHz) is fed to the region through quartz glass. $H_2$ gas is introduced into the upper SWP chamber from the side, and H radicals are generated and transported to the lower CCP region through holes in a shower head type of upper electrode. For the parallel-plate CCP source, a very high frequency (VHF; 100 MHz) is used to obtain advantages in terms of low electron temperature and high plasma density compared with conventional rf (13.56 MHz) CCP. $C_2F_6$ gas is introduced into the lower CCP chamber from the side through the holes in the upper

electrode with H radicals. In Chapter 3 and 4, $CH_4$ gas is also introduced in place of $C_2F_6$ gas to fabricate a different type of CNWs. The typical distance between the electrodes is approximately 4 cm. The lower electrode is ordinary grounded in the case of syntheses of CNWs. The total pressure is maintained at less than several hundreds of pascals with an oil-sealed rotary pump, which can be controlled by a gate valve or an angle valve installed between the pump and the lower CCP chamber. The pressure is measured using a capacitance manometer (Baratron gauge). A substrate is placed on the lower electrode, which is transferred via the load lock chamber. The substrate is heated during the synthesis of CNWs by a carbon heater beneath the lower electrode. When the heater temperature measured with a thermocouple is set to 930˚C, the substrate temperature is estimated to be approximately 630˚C by an optical pyrometer.

Previously, our research group has successfully developed the highly reliable growth process of CNWs using the RI-PECVD system [3]. The growth rate and morphologies of the CNWs are strongly influenced by the surface conditions of the chamber wall. The $O_2$ plasma cleaning process followed by pre-deposition process for passivation of the inside of the chamber can be effective for maintaining the steady conditions to synthesis CNWs with high reproducibility.

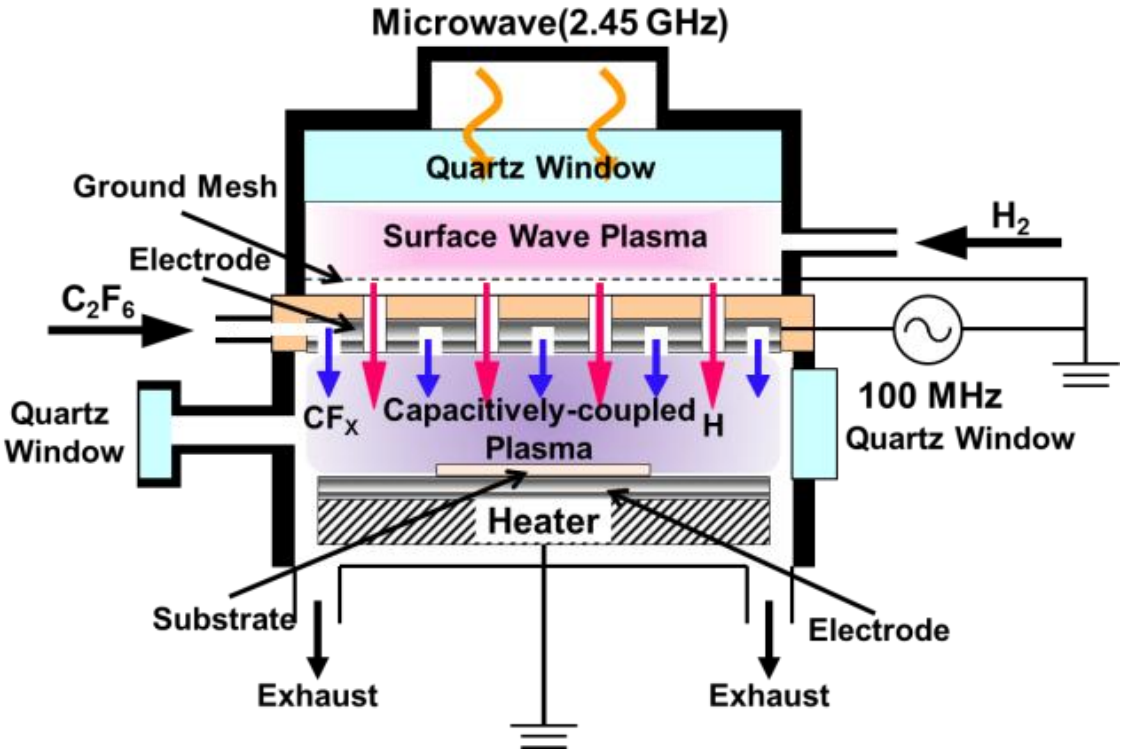


Fig. 2.1 Schematic diagram of the RI-PECVD system.

### 2.1.2 Multi-beam plasma irradiation system

Figure 2.2 shows the schematic diagram of multi-beam plasma irradiation system. This system consists of two plasma beam sources for oxygen (O) atoms and Ar ions. The radical source for O atoms is mounted obliquely at the upper right side of the chamber as a reactor, and $O_2$ gas is introduced into the radical source. The radical source consists of radio frequency (rf: 13.56 MHz) inductively-coupled plasma (ICP) with 8-turn coil and two grounded metal meshes in the head to retard irradiating electrons and ions. An orifice of 2 mm in diameter is installed in the head of O atom source, in order to control the flux of neutral species. O atoms generated in the source are irradiated to a substrate at the angle of 30˚ from the horizontal line. On the other hand, the ion source is mounted on the top of the chamber as a reactor. The ion source consists of 13.56 MHz rf ICP. The plasma potential in the ICP can be set to 0-250 V by applying DC voltage. A grounded metal mesh is installed inside the ion source. Generated Ar ions are accelerated between the ICP and the mesh and irradiated vertically to a substrate. The total pressure is maintained at less than several pascals with a turbo molecular pump, which can be controlled by a gate valve set between the pump and reactor. The pressure is measured using a crystal gauge, an ionized gauge, and a capacitance manometer (Baratron gauge). The base pressure is approximately $1.0\times10^{-4}$ Pa. A substrate is set on the stage in the center of the chamber, where irradiations of all species are focused on, via the load lock chamber. For the thermal oxidation with O atoms in Chapters 3, 4, and 5, the substrate was heated by a carbon heater beneath the lower electrode. When the heater temperature measured by a

thermocouple is set to 900°C, the substrate temperature is estimated to be approximately 700˚C based on an optical pyrometer and ellipsometric analysis.

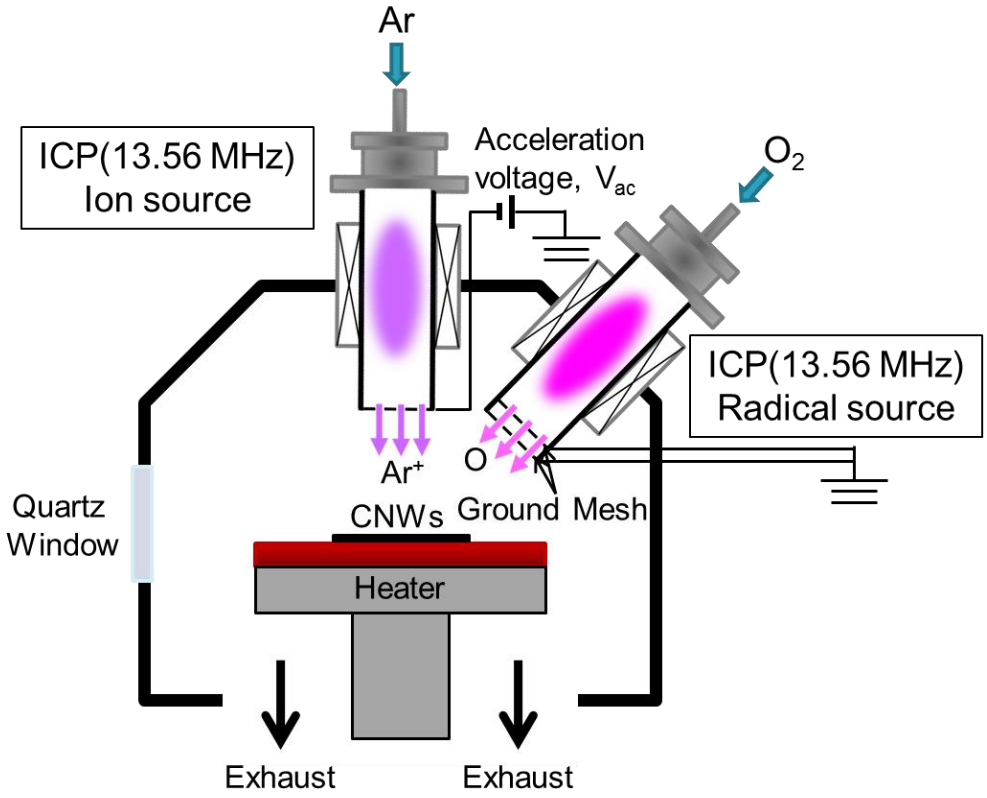


Fig. 2.2. Schematic diagram of the multi-beam plasma irradiation system.

# 2.2. Evaluation methods of CNWs

## 2.2.1 Scanning electron microscopy (SEM)

Scanning electron microscopy (SEM) is one of electron microscopic observational methods, which images a sample surface by scanning with a high-energy electron beam in a raster scan pattern [4]. SEM is one of the most essential tools in present nanoscience and nanotechnology due to the relatively-high resolution. In particular, nanometer-scale morphologies of carbon nanomaterials such as CNWs and CNTs can be readily observed by SEM.

A schematic of an SEM system is shown in Fig. 2.3. The typical SEM system consists of an electron gun, condenser lens, scan coils, objective lens, an electron detector, etc. Electrons emitted from the electron gun pass through a series of lenses to be focused on and scanned across the sample. The electron beam should be bright with small energy spread. A display unit consists of a cathode-ray tube (CRT), defection coil, scanning circuits, video amplifier, etc. The magnification, *M*, is determined by the ratio of the dimension scanned on the CRT to the dimension of the scanned sample *M* = (Length of CRT display)/(Length of scanned sample).

Electron microscopes produce magnified images of samples by electron beams. An electron beam induces emissions of secondary and/or backscattered electrons, auger electrons, characteristic X-rays, and cathode luminescence from the beam-irradiated areas of a sample. In SEM, the secondary and/or backscattered electrons are detected as an electron-beam induced current due to absorption of the electrons. An SEM image is produced by the currents measured at each location with the focused electron beam

scanning the sample [5].

The electron energy is typically ranging from 1 to 30 keV for most samples. Such energetic electrons give us two main advantages over optical microscopes with respect to magnification and depth of field much. De Broglie has proposed in 1923 that particles can also behave as waves [6]. The electron wavelength, $\lambda_e$, depends on the electron velocity, $\upsilon$, or the acceleration voltage, $V$, as shown in the following equation

$$\lambda_e = \frac{h}{mv} = \frac{h}{\sqrt{2qmV}} = \frac{1.22}{\sqrt{V}}\,[nm], \tag{2.1}$$

When $V$ = 10,000 V, $\lambda_e$ = 0.012 nm, which is significantly much smaller than that of visible lights ranging from 400 to 700 nm. For example, the electron wavelength for the commercial model of Hitachi S-5200, which was used in this study, is typically 0.4 nm. Therefore, the much smaller wavelength can make the resolution of SEM much better than that of an optical microscope.

As described above, $V$ is a critical factor to determine the resolution of SEM. Figure 2.4 shows cross-sectional and top-viewed SEM images of typical CNWs observed at $V$ = 1 and 10 kV. Comparing between Fig. 2.3(a),(c) at $V$ = 1 kV and Fig. 2.3(b),(d) at $V$ = 10 kV, the images at $V$ = 10 kV exhibit the higher resolution, which can make us more clearly observe the morphologies of the wall surface and top edge. On the other hand, we should concern about transmission effects of energetic electrons in the case of observations of quite thin structures such as CNWs and CNTs, which have typically several nanometers in thick and diameter for each wall and tube, respectively. Resulting transparent images may give us incorrect surface morphologies. In this study, considering the resolution and transmission effects, the acceleration voltage was chosen to be 10 kV.

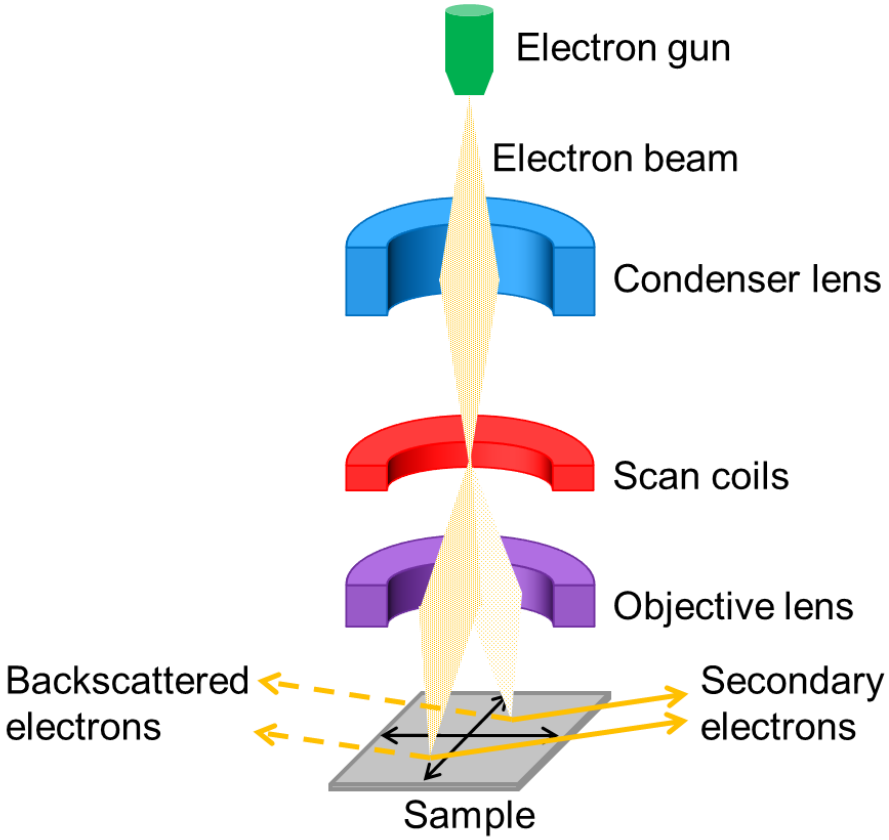


Fig. 2.3. Schematic diagram of electron optical system in SEM.

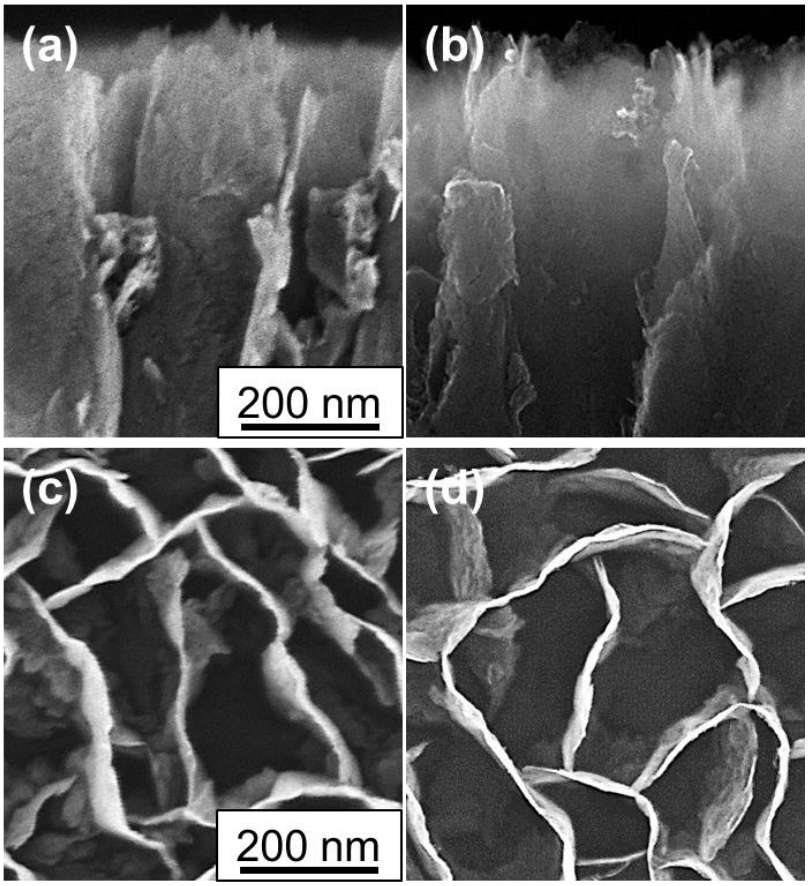


Fig. 2.4. Cross-sectional and top-viewed SEM images of typical CNWs observed at (a),(c) $V$ = 1 and (b),(d) 10 kV.

### 2.2.2 Raman spectroscopy

Raman scattering is a phenomenon that photons irradiated to materials are scattered and lose or gain some amounts of energy, which results in the scattered photons with a lower or higher frequency [7-9]. The former is Stokes scattering and the latter is anti-Stokes scattering. The changes in the frequency of photons in a light strongly depend on the structural characteristics of molecular bonds in the target materials.

Therefore, Raman scattering is very sensitive to the crystalline structures of materials including silicon and carbon materials. For carbon materials, Raman spectroscopy has been usually used as an useful and powerful tool for analyses of graphitic structures in graphene or graphite, carbon black, graphite fiber, amorphous carbon, diamond, carbon nanotubes, and CNWs [10-20]. Raman shifts caused by crystalline structures of carbon materials have been well known. The first-order Raman shift for a diamond has appeared at 1332 $cm^{-1}$ [21]. For microcrystalline graphitic materials, there are three main peaks with the Raman shifts for about 1580 $cm^{-1}$, 1350 $cm^{-1}$, and 1620 $cm^{-1}$, which are assigned as G-band, D-band, and D'-band. The intensities of D-band and D'-band increase with increasing crystalline domain size ($L_a$). D-band and D'-band as well as G-band have been clearly observed in the Raman spectra for a disordered graphite, which correspond to the disorder-induced modes.

Generally, Raman spectroscopy is convenient and useful for qualitatively evaluating the crystallinity of graphitic materials. Equally, some researchers have presented simple equations for quantitatively evaluating the domain size, $L_a$ (or distance between point defects) which has been well-fitted to their experimental results [22-24]. For nanographite samples, Cançado *et al*. have defined a general equation using the peak intensity ratio of D-band to G-band, $I_D/I_G$, as

$$L_a = (2.4 \times 10^{-10})\lambda_l^4 \left(\frac{I_D}{I_G}\right)^{-1}, \quad (2.2)$$

where $\lambda_l$ in nanometer units is the laser line wavelength and the unit of $L_a$ is nm [22]. In Chapter 5, we used this equation to evaluate the domain size of CNWs.

Figure 2.5 shows Raman spectra for pristine graphite and typical CNWs measured with argon ion ($Ar^+$) laser with the wavelength of 532 nm. For CNWs, there are three main peaks of D-band, G-band, and D'-band around 1350, 1580, and 1620 $cm^{-1}$. The relatively-sharp and strong D-band peak is due to their high-density edges and nanocrystalline structures including graphitic defects. In fact, such effects of the structural features of CNWs have been experimentally shown [19,25]. When the Raman spectra are measured by irradiations of the excitation laser from the top and side of CNWs, there is the obvious difference in D-band and D'-band between the two types of laser direction. In the Raman spectra measured from the top edges, the intensities of D-band and D'-band peaks are quite high, which indicates the effect of their high-density edges. On the other hand, the Raman spectra measured from the side wall also exhibit relatively high-intensity of D-band, which means the CNWs contain graphitic defects including domain boundaries.

In this study, Raman spectra for CNWs and graphite were measured using inVia Raman microscope, Renishaw. The 532 nm line of $Ar^+$ laser with a focal spot size of approximately 10 μm was used and the laser power was 1 mW.

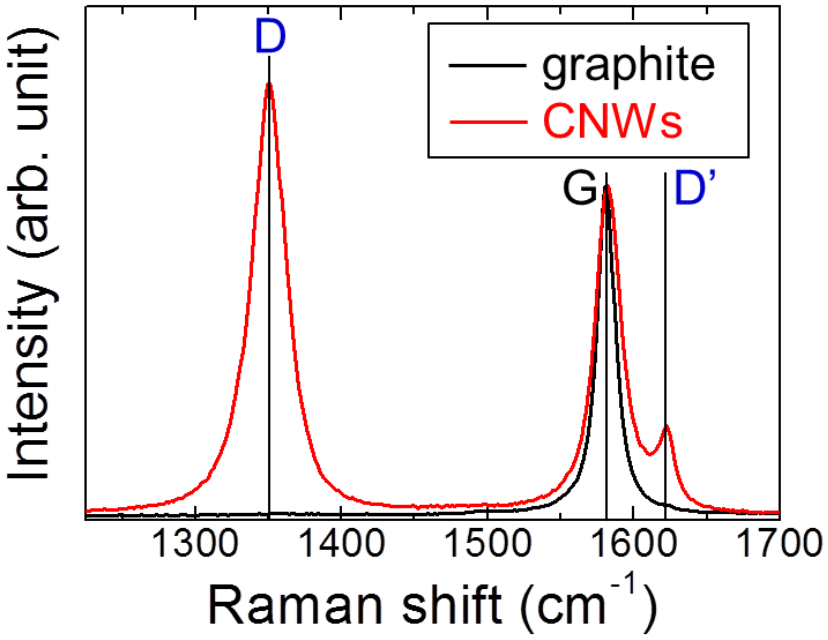


Fig. 2.5. Raman spectra for pristine graphite and typical CNWs.

### 2.2.3 X-ray photoelectron spectroscopy (XPS)

X-ray photoelectron spectroscopy (XPS) is a quantitative spectroscopic technique for analyses of an elemental composition, empirical formula, chemical state, and electronic state of the elements within a material. XPS is also known as one of electron spectroscopy for chemical analysis (ESCA). While XPS can detect all elements with an atomic number, Z, of 3 (lithium) and above, it can detect no hydrogen (Z = 1) or helium (Z = 2). In general, photoelectron signals from most elements can be detected in parts per thousand.

XPS is routinely used to analyze materials in huge different fields such as inorganic compounds, metal alloys, semiconductors, polymers, elements, catalysts, glasses, ceramics, paints, papers, inks, woods, plant parts, make-up, teeth, bones, medical implants, bio-materials, viscous oils, glues, ion modified material, etc. Especially, soft X-ray of AlKα line at 1486.7 eV and MgKα line at 1253.8 eV have been usually used for the X-ray source.

In XPS, the energy of ejected electrons measured by a spectrometer, $E_{sp}$, is related to the binding energy, $E_b$, referenced to the Fermi energy, which can be expressed as

$$E_b = h\upsilon - E_{sp} - q\varphi_{sp}, \tag{2.3}$$

where $h\upsilon$ is the X-ray energy and $\varphi_{sp}$ is the work function of the spectrometer. It should be noted that the incident X-ray energy is monochromatic, which means that $h\upsilon$ is a constant value. The spectrometer and the sample are connected with reference to their Fermi levels which are well defined. The electron binding energy is sensitive to the chemical state, which enables us to identify chemical states from $E_b$. Accordingly, XPS analyses have a strong advantage in chemical and elemental identifications without

mechanical destructions of samples. However, a charging can readily occur in some materials, especially insulators, which affects the detected photoelectron energy.

No photoelectron generated in the deep parts from the surface can reach the surface due to inelastic scattering. The intensity determined by the amount of photoelectrons, $I_d$, is described as

$$I_d = I_\infty\{1 - e^{-d/\Lambda_{(E)}\sin\varphi}\}, \quad (2.4)$$

where $I_\infty$ is the whole intensity determined by the amount of photoelectrons ejected from a film with an infinite of depth, $d$ is the depth from the surface, $\Lambda_{(E)}$ is the escape depth, and $\phi$ is the take-off angle of photoelectron [26]. In many materials, $\Lambda_{(E)}$ ranges from 1 to 5 nm. Moreover, specific information more sensitive to the surface can be obtained by decreasing $\varphi$. For instance, at $\varphi$ = 60˚, e.g. $sin\varphi$ = 0.5, the effective escape depth can decrease to a half of $\Lambda_{(E)}$.

For graphitic materials, $\Lambda_{(E)}$ is approximately 10 nm. Figure 2.6 shows schematic illustrations of take-off angles of photoelectrons for graphite and CNWs. At $\varphi$ = 90˚, while for graphite, photoelectrons ejected from graphene sheets within a depth of 10 nm are detected, for CNWs, the detected photoelectrons can contain not only ones ejected from the top edges but also ones ejected from the wall surface due to not exactly vertically-aligned walls. In addition, the effective escape depth for the CNWs at $\varphi$ = 90˚ is unclear. On the other hand, at $\varphi$ = 8˚, while for graphite, photoelectrons ejected from graphene sheets within a depth of about 1 nm are detected, for CNWs, photoelectrons ejected from around the top edges within a length of about 1 nm can only be detected.

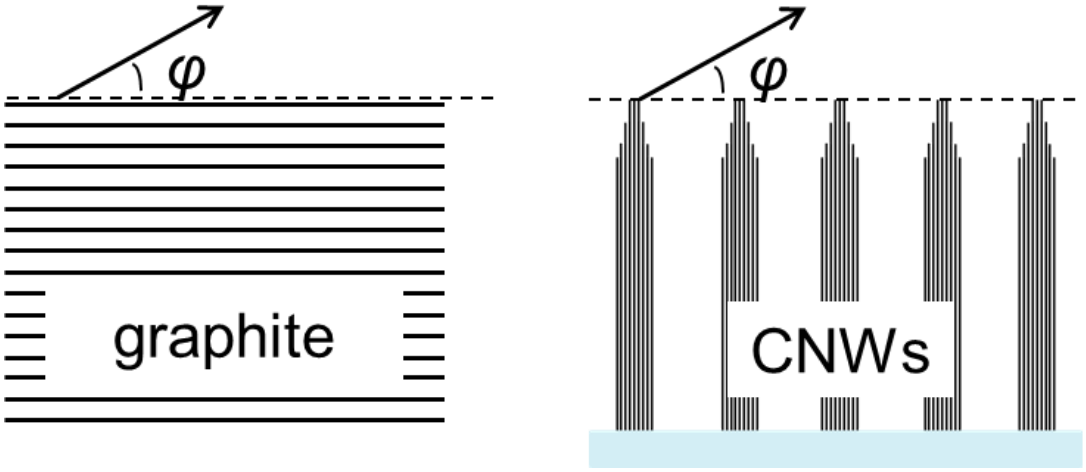


Fig. 2.6. Schematic illustrations of take-off angles of photoelectrons, $\varphi$, for graphite and CNWs.

### 2.2.4 X-ray diffraction (XRD)

X-ray diffraction (XRD) is a non-destructive technique for identifying crystalline structures such as crystalline phases, orientation, and grain size. XRD requires no specific preparation of samples and gives crystallographic information of relatively-high accuracy. When monochromatic X-rays with a wavelength of $\lambda$ is incident on the sample at an angle of $\theta$, some of them are reflected at the same angle of $\theta$. The X-rays scattered from adjacent lattice planes with a lattice spacing of $d$ reinforce the total detected X-rays when a difference in the path length determined with $\theta$ is equal to the integral multiple of $\lambda$, $n\lambda$. The relation can be described below, which is the Bragg's law.

$$2d \sin\theta = n\lambda, \tag{2.5}$$

For example, the wavelength of CuKα line is 1.5418 Å and the lattice spacing of graphite (002) is about 0.34 nm.

The grain size can be estimated with the width of a diffraction peak, via Scherrer's equation expressed as

$$D_{hkl} = \frac{k\lambda}{\beta \cos\theta}, \tag{2.6}$$

where $D_{hkl}$ is the grain size of ($hkl$) lattice plane, $\beta$ is the width of a diffraction peak, and $k$ is a constant which is 0.9 (width is full-width at half-maximum) or 1 (width is integral width).

For a planar graphite, the graphite (002) lattice planes existing in the vertical direction to the surface can be mainly evaluated based on the Bragg's law and Scherrer's equation. For CNWs, the diffraction peak caused by graphite (002) lattice planes can be also observed. However, the graphite (002) lattice planes in the CNWs exist almost in the parallel direction to the film surface and exhibit the crystallinities of

each wall in the thichness direction as shown in Fig. 2.7. According to the characteristic crystalline structure of CNWs, in this study, we used the in-plane XRD with the incident X-rays at a small angle of 0.4˚ to the film surface. Because each CNW is ramdomly oriented in the plane parallel to the film surface and almost but not perfectly vertically-aligned in the plane perpendicular to the film surface, we can see the X-ray diffraction stochastically occurred in the CNWs.

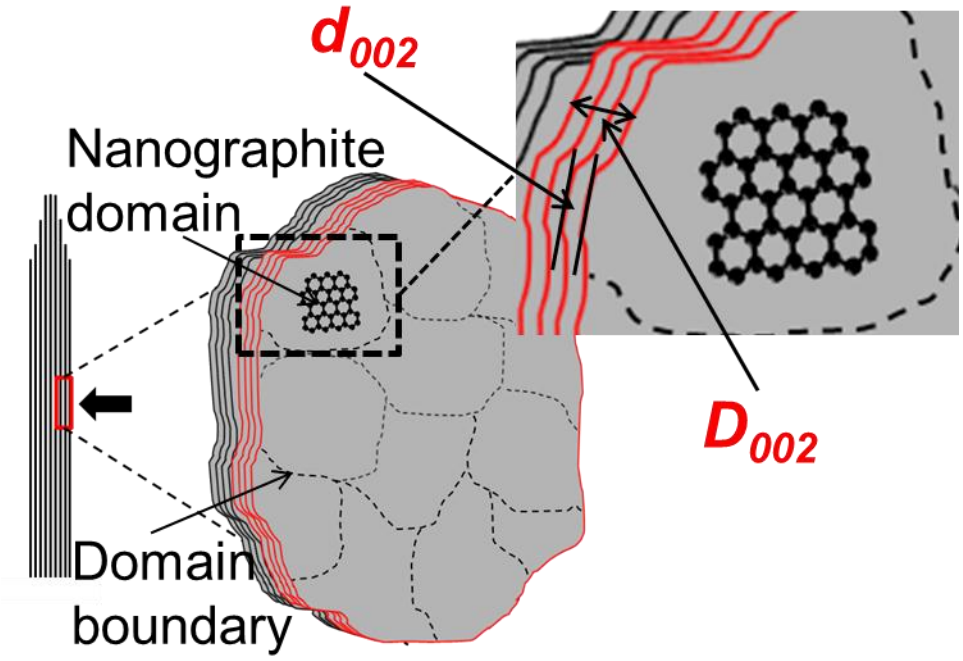


Fig. 2.7. Schematic illustration of graphite (002) lattice planes in CNWs.

# References

[1] M. Hiramatsu, K. Shiji, H. Amano, and M. Hori: Appl. Phys. Lett. **84** (2004) 4708.

[2] M. Hiramatsu and M. Hori: Jpn. J. Appl. Phys. **45** (2006) 5522.

[3] S. Kondo, M. Hori, K. Yamakawa, S. Den, H. Kano, and M. Hiramatsu: J. Vac. Sci. Technol. B **26** (2008) 1294.

[4] M. Knoll: Zeitschrift für technische Physik **16** (1935) 467.

[5] P. Sigmund: Phys. Rev. **184** (1969) 383.

[6] D. K. Schroder: *Semiconductor Materials and Device Characterization Third Edition*, (Wiley, New York, 2006).

[7] C. V. Raman and K. S. Krishnan: Nature **121** (1928) 501.

[8] R. Singh: Physics in Perspective **4** (2002) 399.

[9] G. Landsberg and L. Mandelstam: Naturwissenschaften **16** (1928) 557.

[10] R. J. Nemanich and S. A. Solin: Phys. Rev. B **20** (1979) 392.

[11] G. Katagiri, H. Ishida, and A. Ishitani: Carbon **26** (1988) 565.

[12] M. Nakamizo, R. Kammereck, P.L. Walker Jr.: Carbon **12** (1974) 259.

[13] T. P. Mernagh, R. P. Cooney, and R. A. Johnson: Carbon **22** (1984) 39.

[14] T. C. Chieu, M. S. Dresselhaus, and M. Endo: Phys. Rev. B **26** (1982) 5867.

[15] H. Tsai and D. B. Bogy: J. Vac. Sci. Technol. A **5** (1987) 3287.

[16] J. Wagner, M. Ramsteiner, Ch. Wild, and P. Koidl: Phys. Rev. B **40** (1989) 1817.

[17] A. C. Ferrari and J. Robertson: Phys. Rev. B **63** (2001) 121405.

[18] A. M. Rao, E. Richter, S. Bandow, B. Chase, P. C. Eklund, K. A. Williams, S. Fang, K. R. Subbaswamy, M. Menon, A. Thess, R. E. Smalley, G. Dresselhaus, and M. S.

Dresselhaus: Science **275** (1997) 187.

[19] S. Kurita, A. Yoshimura, H. Kawamoto, T. Uchida, K. Kojima, M. Tachibana, P. Molina-Morales, and H. Nakai: J. Appl. Phys. **97** (2005) 104320.

[20] Z. H. Ni, H. M. Fan, Y. P. Feng, Z. X. Shen, B. J. Yang, and Y. H. Wu: J. Chem. Phys. **124** (2006) 204703.

[21] D. S. Knight and W. B. White: J. Mater. Res. **4** (1989) 385.

[22] L. G. Cançado, K. Takai, T. Enoki, M. Endo, Y. A. Kim, H. Mizusaki, A. Jorio, L. N. Coelho, R. Magalhães-Paniago, and M. A. Pimenta: Appl. Phys. Lett. **88** (2006) 163106.

[23] L. G. Cançado, A. Jorio, E. H. Martins Ferreira, F. Stavale, C. A. Achete, R. B. Capaz, M. V. O. Moutinho, A. Lombardo, T. S. Kulmala, and A. C. Ferrari: Nano. Lett. **11** (2011) 3190.

[24] A. C. Ferrari and J. Robertson: Phys. Rev. B **61** (2000) 14095.

[25] T. Mori, M. Hiramatsu, K. Yamakawa, K. Takeda, and M. Hori: Diamond and Related Materials **17** (2008) 1513.

[26] T. Sugano, N. Mikoshiba, and A. Hiraki: *Hyomen Denshi Kougaku [Surface Electronics Engineering]* (Corona, Tokyo, 1979). [in Japanese]

# Chapter 3

# Modification of CNW edges by reaction with oxygen atoms

## 3.1 Introduction

Some researchers have studied on oxidation reactions with atomic oxygen (O) in graphite as one of basic and simplest oxidative reactions [1-6]. These studies have shown that the oxidative reaction with O atoms exhibits activation energies depending on temperature. The detailed study on the oxidation of graphite has been carried out using O atoms generated in a radio frequency (rf) plasma in the temperature range from 14 to 350˚C [6]. The oxidation rate estimated with the changes in the weight of graphite depends on the temperature. The activation energies at the temperatures from 14 to 200˚C are in the range from 0.43 to 0.47 eV. However, the activation energy decreases to almost zero (less than 0.05 eV) with increasing temperature from 200 to 350˚C. This temperature dependence of the activation energy indicates that the rate-determining process for the oxidative removal of carbon (C) atoms in graphite can change with increasing temperature. Namely, while the rate-determining process at 14 to 200˚C is

formation of volatile products such as CO and $CO_2$ due to thermal energies, that at 200 to 350˚C is adsorption of O atoms determined by its concentration and flux. Therefore, most thermal oxidation processes for graphite using O atoms can be macroscopically considered as a first order reaction with respect to the flux of O atoms. On the other hand, at around room temperature, O atoms can more readily form surface oxides than molecular oxygen, and the induced surface oxide can retard the oxidation rate.

Focusing on the surface reaction on graphite at 150˚C, O atoms form monolayer pits in various sizes which are initiated from vacancies and also continuously the additional vacancies [7]. The shape of the pits formed by the reaction with atomic oxygen is hexagonal and different from that in the case of molecular oxygen which is circular. The oxidation reaction with O atoms preferentially proceeds in the direction of *a* axis rather than the direction of *c* axis in the graphite lattice.

These experimental studies on the oxidation of graphite with O atoms are consistent with the later experimental and theoretical sturdies as described in Subsection 1.4.1. These studies indicate that temperature dependences and the amount of O atoms contributing to oxidation reactions are critical factors in identification of the oxidation process in graphitic structures. However, no detailed study on the oxidative processes in graphene edges and planes containing defects has been conducted based on the reaction with atomic oxygen. As CNWs have a high-density of edges and large surface area of planes based on nanometer-sized graphene, more microscopic approach to identify the oxidation processes by O atoms in different graphitic structures can be realized using CNWs. Furthermore, such fundamental knowledge of the oxidation of CNWs including various structural fluctuations is necessary to be understood toward precisely controlling their structural and electronic characteristics.

In this chapter, we investigated the effects of atomic oxygen (O) treatment on the structures of CNWs and its temperature dependence. The oxidation rate was estimated with the change in the height of CNWs while the morphological, crystallographic, and chemical changes were evaluated for the treated CNWs. The activation energy for the oxidation from the top edges of CNWs was determined with Arrhenius plot and compared with that for graphite. Furthermore, two types of CNWs with extremely different crystallinities synthesized by $C_2F_6/H_2$ and $CH_4/H_2$ plasmas were compared with respect with the effects of the O treatment, which gave us the dependence of the crystalline structures of CNWs.

## 3.2 Experimental details

CNWs were fabricated using the RI-PECVD system as described in the section 2.1.1. Carbon source gas of $C_2F_6$ was introduced into the VHF-CCP region with a flow rate of 50 standard cc per minute (sccm). $H_2$ with a flow rate of 100 sccm was introduced into the microwave-SWP region, and H radicals were injected into the VHF-CCP. The total gas pressure was 173 Pa. The VHF power for CCP ranged from 220-250 W and the microwave power of SWP was 270 W. A Si wafer was used as the substrate and set on the sample stage as the grounded electrode. The substrate temperature was measured to be about 630˚C using an optical pyrometer. The typical deposition time was 30 min. This type of CNWs will be called CF-CNWs.

A different type of CNWs was also fabricated employing RI-PECVD. Instead of $C_2F_6$, $CH_4$ was introduced into the VHF-CCP region with a flow rate of 100 sccm. The

flow rate of $H_2$ gas and the total gas pressure were 50 sccm and 1 Pa, respectively. The VHF power for CCP and the microwave power for SWP were 300 and 400 W. A Si wafer was used as the substrate and set on the sample stage as the grounded electrode. The substrate temperature was about 600˚C. The deposition time was 15 min. This type of CNWs will be called CH-CNWs in Sect. 3.4.

After the growth of the CNWs, the CNWs were treated with atomic oxygen produced using the radical source of multi-beam plasma irradiation system described in Subsection 2.1.2. The oxygen plasma was generated in the remote plasma system as a radical source. The total pressure in the chamber with an oxygen flow rate of 10 sccm and input RF power were 0.2 Pa and 500 W. The CNW samples were placed on the heater stage located approximately 20 cm apart from the exit of the radical source. The substrate temperature was changed to 25, 300, and 700˚C. The oxygen treatment time was 5 min. In addition, we measured the absolute density of oxygen atoms employing a vacuum ultraviolet absorption spectroscopy (VUVAS) [8]. The measurement system was attached to the chamber as shown in Fig. 3.1. The VUV light passed about 30 mm above the sample and the abruption pass length was 270 mm. As a result, the absolute density of O atoms near the substrate was measured and the flux of oxygen atoms incident on the substrate was estimated to evaluate the reaction probabilities of oxygen with the CNWs edges.

After the O treatments, the morphologies of the CNWs were observed by scanning electron microscopy (SEM). The crystalline structures of CNWs were also evaluated using Raman spectroscopy and X-ray diffraction (XRD). X-ray photoelectron spectroscopy (XPS) using Mg Kα radiation (photon energy: 1253.6 eV) was used to evaluate the amount of oxygen.

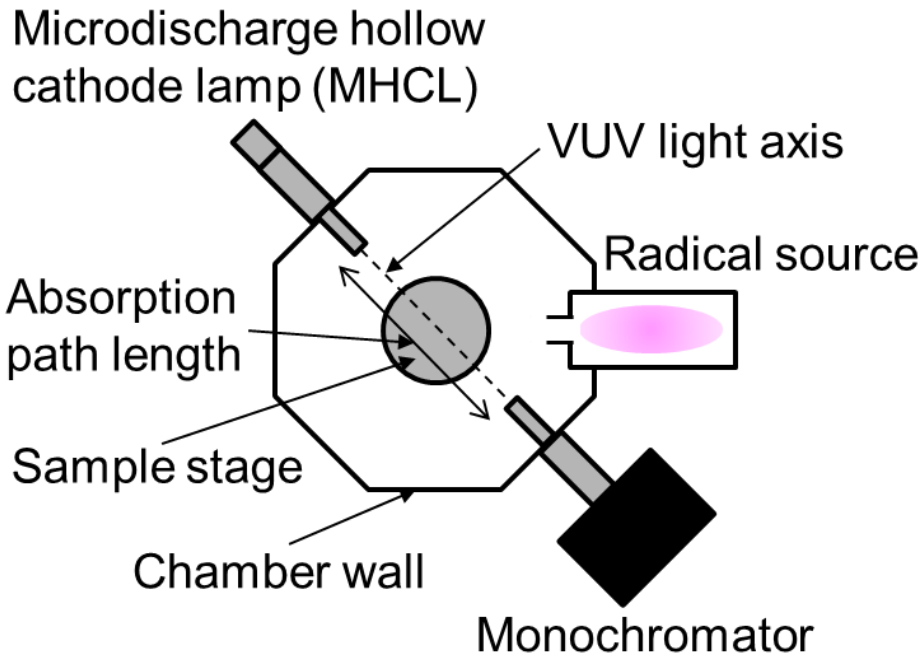


Fig. 3.1. Schematic diagram of the overhead view of the VUVAS measurement system installed to the chamber of the multi-beam plasma irradiation system.

# 3.3 Effects of atomic oxygen treatment on structures of CNWs

## 3.3.1 Morphological and crystallographic changes in O-treated CNWs

The CNWs were etched by oxygen (O) atoms generated in oxygen plasma as a radical source. Figure 3.2 shows the cross-sectional SEM images and each overhead view of CNWs before and after the O treatment. The height of CNWs before the treatment was initially 500 nm. The CNWs were etched off by approximately 30 nm from the top after the atomic oxygen treatment at 25˚C as shown in Fig. 3.2(c). The variation in average height of CNWs increased to approximately 160 nm at 700˚C with increasing temperature. A partial asperity was induced on the edges and the edge surface morphology was also changed to a little rougher, in particular, at 700˚C as shown in Fig. 3.2(h). On the other hand, the morphology of the wall plane surface was shown to have no etching reaction.

By the way, CNWs were also exposed to oxygen molecular gas without a plasma discharge at the same gas pressure and substrate temperature. However, no etching reaction was observed on both the wall surface and top edge even at 700 ˚C. The partial pressure of oxygen molecule in this experiment is more than two orders of magnitude lower than those in the thermal oxidations of graphite and carbon nanomaterials [6,7,9-12]. In addition, the specific surface area of the graphene planes in the CNWs is more than ten times larger than that of a planar graphite. Therefore, it is suggested that the amount of oxygen molecule incident on the CNW surfaces is too small to produce

oxidation of the graphene planes in this experiment. In contrast, the SEM observation showed that O atoms could selectively react with the top edges of CNWs. It is noteworthy that this selective reaction inducing the anisotropic etching occurred without ion irradiations in the oxygen plasma.

Raman spectra of the CNWs were measured at room temperature in air using the 532 nm line of an argon laser. The Raman spectra of the CNWs before and after the O treatments at 25, 300, and 700˚C are shown in Fig. 3.3. In all Raman spectra of the CNWs, there were three main peaks corresponding to G-band, D-band, and D'-band which appear around 1580, 1350, and 1620 $cm^{-1}$, respectively. The relatively strong and sharp D-band and D'-band peaks were observed. Each Raman spectrum of the CNWs was normalized by the peak intensity of G-band. Furthermore, the peak intensity ratios of D-band to G-band ($I_D/I_G$) and full width at half maximum of G-band ($\Delta\nu_{G\text{-band}}$) were determined by curve fitting with Lorentzian peak shape. The relative intensity of D-band slightly decreased after the O treatments as shown in the inset of Fig. 3.3, where the value of $I_D/I_G$ changed from 1.29 to 1.10 for the treatment at 25˚C. On the other hand, the value of $\Delta\nu_{G\text{-band}}$ slightly increased from 22 to 25 $cm^{-1}$ after the treatment at 25˚C and then decreased to 23 $cm^{-1}$ with increasing the substrate temperature.

In general, the factors in decreasing $I_D/I_G$ for micro/nanocrystalline graphite include a decrease in the amount of defects and an increase in the crystallite size. However, it should be noted that in contrast to such typical graphitic nanocrystals, CNWs have the high-density edges on the film surface significantly affecting D-band in the Raman spectra [13]. From the SEM observations, O atoms can preferentially react with the top edges of CNWs and locally induce much more defected edges due to oxidative chemisorption and etching. Such a kind of amorphization in graphitic structures can

inactivate the defective mode Raman scattering from the graphite structures, in particular, the top edges of CNWs [14,15]. Accordingly, these results suggest that amorphization caused by the oxidation reaction with O atoms on the top edges of CNWs would result in decreasing $I_D/I_G$ in the Raman spectra after atomic oxygen treatments. However, these changes in Raman spectra were relatively small, which indicates that O atoms may affect only the top edges and wall surface and a large fraction of the vertically-aligned nanographites keeps relatively-high graphitization degree.

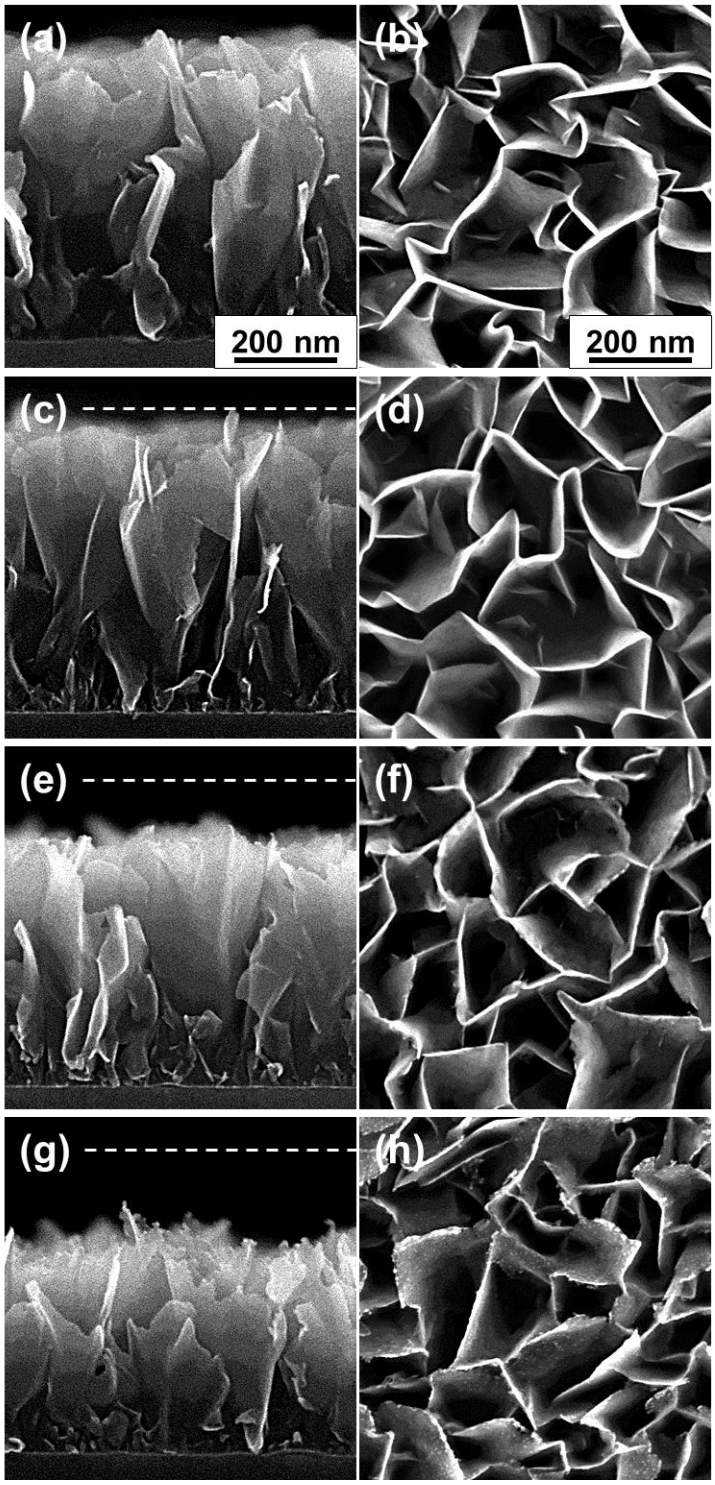


Fig. 3.2. Cross-sectional SEM images and each overhead view of CNWs (a),(b) before and after the O treatment at (c),(d) 25, (e),(f) 300, and (g),(h) 700˚C for 5 min. The white dash lines in (c), (g), and (g) indicate the average height of the initial CNWs before the treatment.

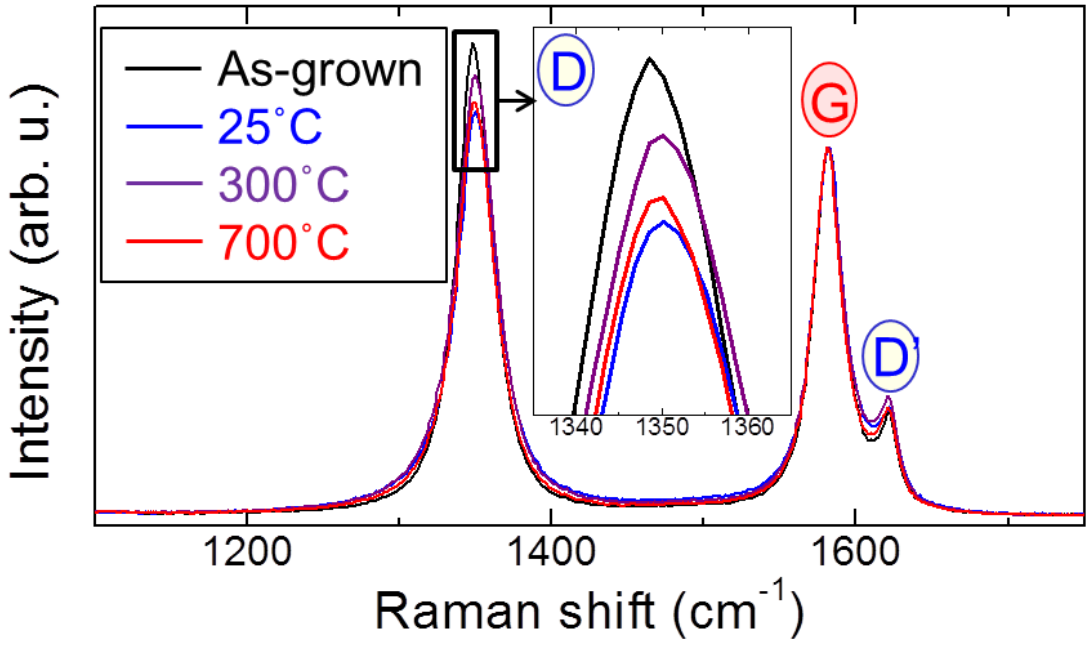


Fig. 3.3. Raman spectra of the CNWs before and after the O treatments at 25, 300, and 700˚C.

### 3.3.2 Estimation of rate constant from Arrhenius plot

The activation energy and reaction probability for the oxidative reaction at the top edges of CNWs were estimated to summarize the above results of etching from the top edges. Figure 3.4 shows a temperature dependence of the etch rate, which was calculated on the basis of the variation in average height of CNWs and the carbon atom density around the CNW edges. The carbon atom density was estimated to be about $4\times10^{21}$ $cm^{-3}$ by calculation with the total surface area of top edges of CNWs in a SEM image, which gave an assumption of 200 sheets of graphene in a wall thickness of 70 nm per micrometer.

The etched amount of the CNWs increased with increasing substrate temperature. An Arrhenius-type behavior with an activation energy of 0.06±0.04 eV was shown for the removal rate of carbon atoms at the top edges of the CNWs. The activation energy was almost barrierless for the etching reaction at the CNW edge. This was similar to the value of less than 50 meV comparable to the case of oxidation of graphite with O atoms at more than 200˚C as reported in the literature [6]. The fact indicates that the oxidative process by O atoms on the top edges of CNWs is almost independent of temperature and the rate-determining process is adsorption of O atoms. This may also indicate that the thermal oxidation of graphite would dominantly occur on graphene edges existing in the sample edges and in-plane vacancies with increasing temperature.

To analyze the Arrhenius plot in detail, the triplet O atom density was estimated to be approximately $2\times10^{10}$ $cm^{-3}$ by VUVAS measurements. The density of singlet O atoms was much lower than the detection limit ($1\times10^{10}$ $cm^{-3}$). Assuming the root-mean-square velocity at room temperature in the case of a remote oxygen ICP, the

flux of O atoms incident on the sample surface can be calculated to be $1.4\times10^{15}$ $cm^{-2}s^{-1}$ [16]. The reaction probability can be defined as the number of carbon atom removed per unit time and area by an O atom. According to this definition, the reaction probability was estimated to be 0.3 by dividing the intercept of the exponent of the vertical axis in Fig. 3.4 by the flux obtained above. The rate constant for the reaction described above, *k*, can be expressed as

$$k = 0.3\exp(-0.06/\mathrm{R}T), \tag{3.1}$$

where *R* is the gas constant and the unit of *k* is $cm^{-2}s^{-1}$. The values of *k* can be calculated with eq. (3.1) to be approximately 0.03, 0.09, and 0.15 $cm^{-2}s^{-1}$ at 25, 300, and 700˚C, respectively. Considering the ratio of the edge surface area of CNWs to the substrate surface area is less than 10%, these values mean that O atoms may preferentially and effectively remove the carbon atoms on the top edge. This also indicates that O atoms hardly contribute to etch the graphene planes on the CNW surfaces at least at the lower pressure, which is intrinsically much lower reactive than the edge.

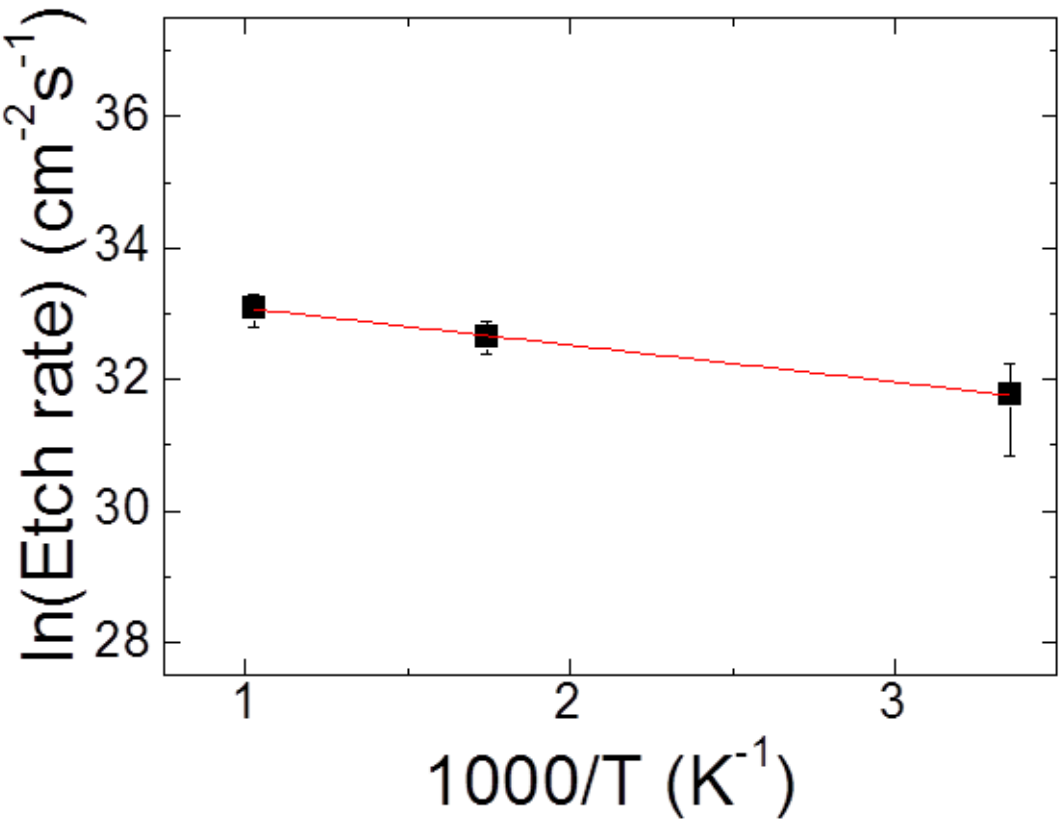


Fig. 3.4. Arrhenius plot for the temperature dependence of the etch rate with the definition as the number of carbon atoms removed per unit time and area, where the line is the least-squares linear fit.

### 3.3.3 Surface chemical states of O-treated CNWs

To examine the surface chemical states in the O-treated CNWs, *ex situ* XPS analysis was carried out. Figure 3.5 shows the X-ray photoelectron spectra of the C 1s and O 1s regions for the CNWs. The binding energy was calibrated to the C 1s graphitic peak at 284.5 eV. The O 1s peaks were normalized with the peak area of each C 1s peak, which gave us the peak area ratios of O 1s to C 1s. The spectra were decomposed into some components by curve fitting assuming Gaussian-Lorentzian peak shapes after Shirley background correction. In the C 1s region, four components arising from oxides were assigned with respect to bonding of 1, 2, and 3 O atoms. The peaks shifted by approximately 1.5-2.0 eV for one or two O atom, 3.0 eV for one, 4.0-4.5 eV for two, and 6.1 eV for three as referenced to the peak position for the graphitic peak and each peak was assigned as 1,2,3,and 4 in the C 1s region of Fig. 3.5 [17]. The oxides bonding to one to three O atoms also include such functional groups as alcohol (C-OH) or ether (O-C-O), carbonyl (C=O), carboxyl (COOH) or ester (COOR), and carbonate ($CO_3^-$) [17].

Notations of (a)-(d) correspond to (a) as-grown, after atomic oxygen treatments at (b) 25, (c) 300, and (d) 700˚C. Fig. 3.5(b) The oxide-related components were clearly observed in the CNWs treated at 25˚C [Fig. 3.5(b)] while there was no significant difference between those treated at 300 and 700˚C, which were exactly comparable with respect to the signal-to-noise (S/N) ratio. The integrated intensity of the O 1s peak increased owing to the increase in the amount of physisorbed and chemisorbed oxygen on the CNW edges and surfaces. These results indicate that surface oxide layers may be formed by the oxidation reaction. The O 1s peak intensity decreased with

increasing temperature, which can be considered as the result from the dominant etching reaction or desorption of adsorbed oxygen and the promotion of recombination at higher temperatures.

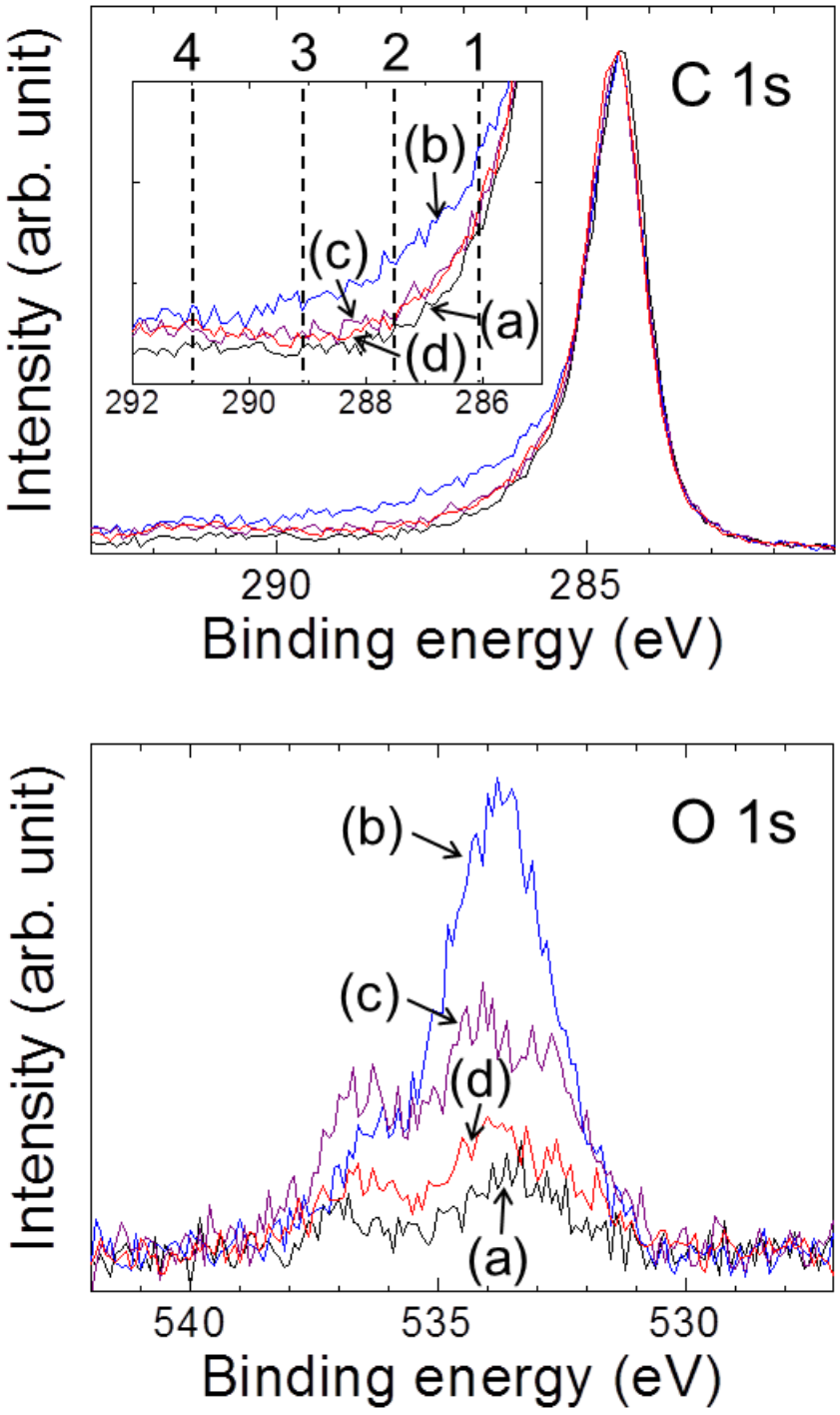


Fig. 3.5. C ls and O 1s photoelectron spectra of the CNWs (a) as-grown, after atomic oxygen treatments at (b) 25, (c) 300, and (d) 700˚C. The C 1s includes the magnified view as an inset.

# 3.4 Dependence of reaction with atomic oxygen on crystalline structures of CNWs

## 3.4.1 Differences between crystalline structures of $C_2F_6/H_2$- and $CH_4/H_2$-CNWs

Our previous study has compared between the growth rates and macroscopic morphologies of CNWs synthesized $C_2F_6/H_2$ and $CH_4/H_2$ plasmas (CF-CNWs and CH-CNWs) [18]. It has been found that while each wall in CH-CNWs is rather wavy and a little thinner than that in CF-CNWs, the total morphology of CH-CNWs is similar to that of CF-CNWs. Figure 3.6 shows the SEM images as overhead views of CF- and CH-CNWs synthesized by the RI-PECVD system. Both types of CNWs had maze-like structures consisting of differently-bending walls, which was consistent with the previous study.

Now, to focus on the crystalline structures of both CNWs, we measured Raman spectra and X-ray diffraction (XRD) patterns. Figure 3.7 shows the Raman spectra for the CF- and CH-CNWs normalized with the intensity of G-band. There were three main peaks of G, D, and D' in the smaller shift region, and 2D'', 2D, G+D, and 2D' in the larger shift region. In the Raman spectra, the relative intensity of D-band to G-band for the CH-CNWs was higher than that for the CF-CNWs, which means a larger amount of graphitic defects. In addition, the relative intensity of 2D-band to G-band was much lower than that for the CF-CNWs, which indicates larger disorders of hexagonal rings in the graphene planes such as breaking the symmetry. The broader G-band and 2D-band

peaks for the CH-CNWs were also attributed to such the disorders. These results indicate that the CH-CNWs may be composed of lower-crystallized graphene sheets.

On the other hand, we could evaluate the layered structures of graphite in CNWs with the measured XRD patterns as shown in Fig. 3.8. The graphite (002) lattice spacing in the CF- and CH-CNWs was calculated to be 0.340 and 0.343 nm with the diffraction angles, while that in a typical graphite sample is approximately 0.335 nm for the diffraction angle of 26.54˚. Furthermore, each crystallite size for the graphite (002) lattice plane was also estimated to be 5.8 nm for the CF-CNWs and 2.5 nm for CH-CNWs. From the XRD analyses, it was found that the layered structure of graphene sheets in CH-CNWs exhibits larger lattice spacing and smaller crystallite size than in CF-CNWs as shown in Fig. 3.9 of an illustration of the structural model of CH-CNW. Such information of the graphitic crystalline structures obtained by Raman spectroscopy and XRD can be correlated [19]. These differences in the crystalline structures of CH-CNWs in comparison with those of CF-CNWs are considered to be due to the amount of residual hydrogen because the hydrogen content is one of important factors in affecting the $sp^2/sp^3$ component fraction in amorphous carbons [14].

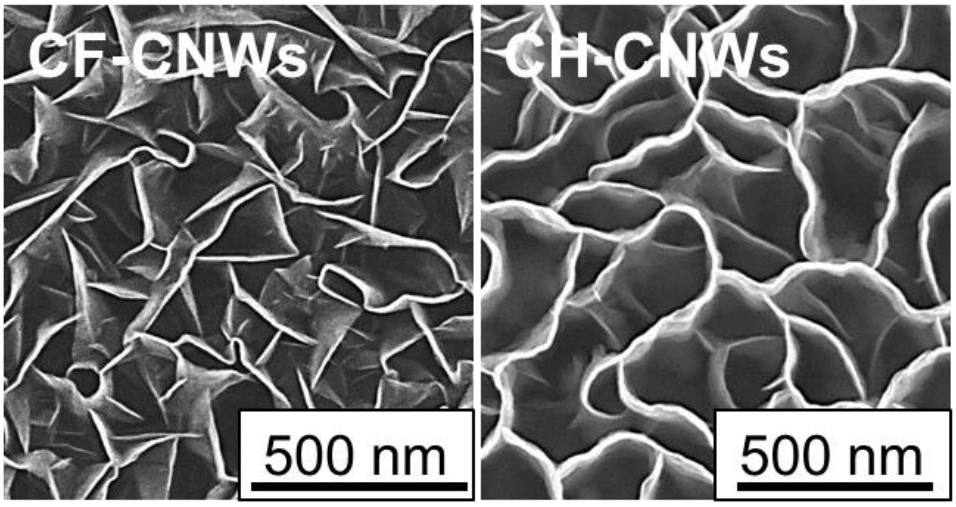


Fig. 3.6. SEM images as overhead views of CF- and CH-CNWs.

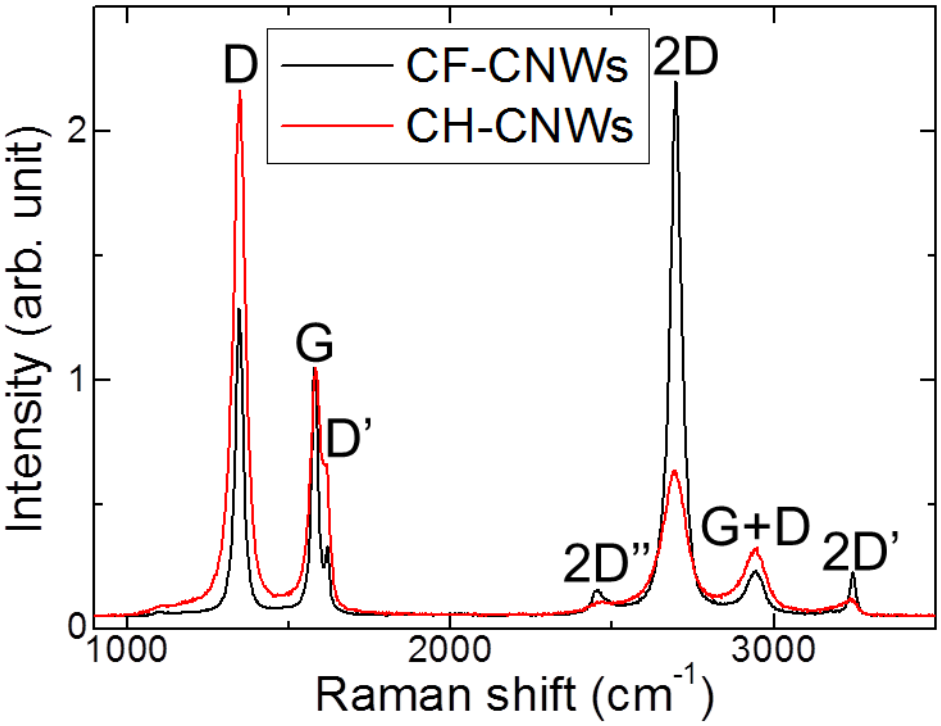


Fig. 3.7. Raman spectra for CF- and CH-CNWs.

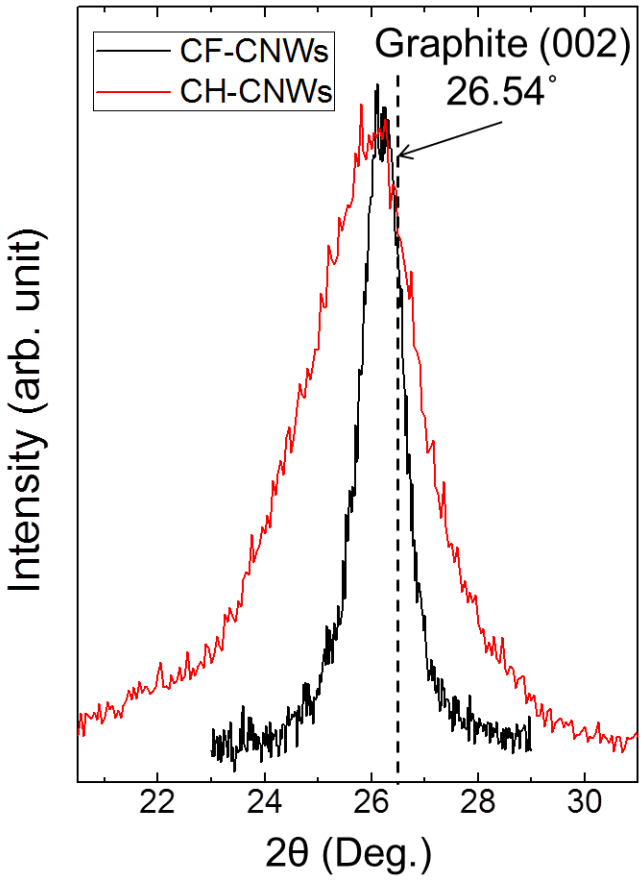


Fig. 3.8. XRD patterns for CF- and CH-CNWs with the graphite (002) line as a reference.

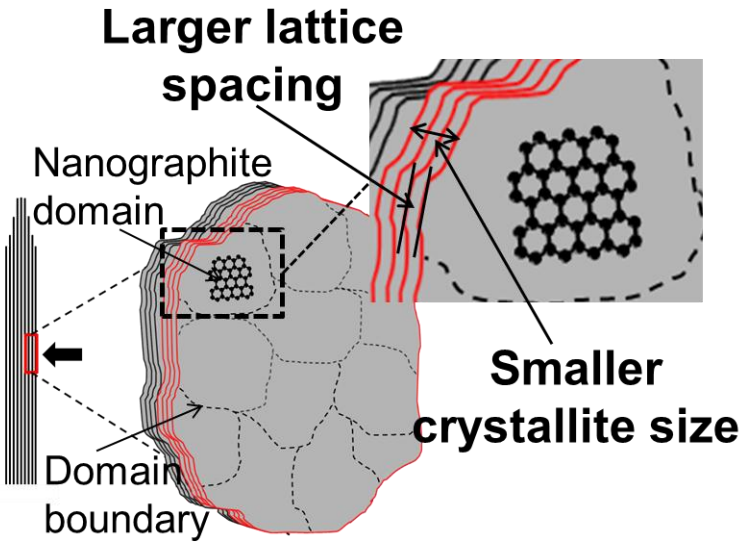


Fig. 3.9. Illustration of a structural model of CH-CNWs.

### 3.4.2 Morphological and crystallographic changes in O-treated $CH_4/H_2$-CNWs

The CH-CNWs were also etched by the O treatment under the same condition as the case of CF-CNWs. Figure 3.10 shows the cross-sectional SEM images and each overhead view of CH-CNWs before and after the O treatments. Before the treatment, the CNWs have initially a height of 1800 nm. After the O treatment at 25˚C as shown in Fig. 3.10(c), the CH-CNWs were etched off by approximately 100 nm from the top. The change in the average height of CH-CNWs increased to approximately 600 nm at 700˚C with increasing the temperature. As a result, the etch rate of CH-CNWs from the top edges was approximately five times faster than that of CF-CNWs. The reaction with O atoms on the top edges of CH-CNWs induced much rougher edge surfaces than CF-CNWs, which became more marked with increasing the temperature as shown in Fig. 3.10(f) and (h). On the other hand, although differences in the wall thicknesses were hard to be evaluated because of the rough morphologies of the edge surfaces, there was no significant change in morphologies of the wall plane surface in the CH-CNWs as was the case in the CF-CNWs. These results indicate that the lower crystallinities of graphene sheets and its layered structure of CH-CNWs can enhance the etching reaction from the top edges of CNWs with O atoms.

Raman spectra of the CH-CNWs before and after the O treatments were measured and compared with those of the CF-CNWs. Figure 3.11 shows Raman spectra for the CH-CNWs before and after the O treatments at 25, 300, and 700˚C. From these Raman spectra, the peak intensity ratios of D-band to G-band ($I_D/I_G$) and full width at half maximum of G-band ($\Delta\nu_{G\text{-band}}$) were determined by curve fitting with Lorentzian peak

shape for each Raman spectrum. Figure 3.12 shows the values of $I_D/I_G$ and $\Delta\nu_{G\text{-band}}$ as a function of G peak position, in which also includes the values for the CF-CNWs. First, it is noteworthy that the G peak position for the CH-CNWs significantly changed after the O treatments, which strongly depended on the treatment temperature. The G peak position decreased from about 1585 to 1574 $cm^{-1}$ after the treatment at 25˚C. In contrast, the G peak position increased up to about 1589 $cm^{-1}$ after the treatment at 700˚C. No such peak shifts caused by the O treatments were observed in the Raman spectra for the CF-CNWs. At the same time, $I_D/I_G$ decreased from 0.38 up to 0.48 by the O treatment at 25˚C and hardly depended on the temperature as shown in Fig. 3.12(a). Additionally, $\Delta\nu_{G\text{-band}}$ increased from 36 up to 43 by the O treatment at 25˚C with almost no temperature dependence. These tendencies of $I_D/I_G$ and $\Delta\nu_{G\text{-band}}$ in the Raman spectra for the CH-CNWs are similar to those for the CF-CNWs.

From these changes in Raman spectra, we can consider the effects of oxidative chemisorption and etching on the crystalline structures of CH-CNWs. During the reaction with O atoms at 25˚C, O atoms more readily chemisorb mainly on the top edges and may induce more amorphization due to the lower crystallinity of CH-CNWs, which results in the downward shift of G peak and changes in $I_D/I_G$ and $\Delta\nu_{G\text{-band}}$ [14,15]. Furthermore, such the downward shift of G peak can be also due to oxygen-induced hole doping into graphene sheets [20]. On the other hand, the reaction with O atoms at higher temperatures enhances the etching from the top edges and may form a little smaller crystallites and region containing more $sp^3$ component, which corresponds to the upward shift of G peak and changes in $I_D/I_G$ and $\Delta\nu_{G\text{-band}}$ as well as the rougher edge surface morphologies observed in the SEM images as shown in Fig. 3.10(f) and (h) [14,15]. Therefore, the crystalline structures of CNWs with lower crystallinities of

graphene sheets and its layered structure can be susceptible to the effects of the reaction with O atoms resulting in oxidative chemisorption and etching.

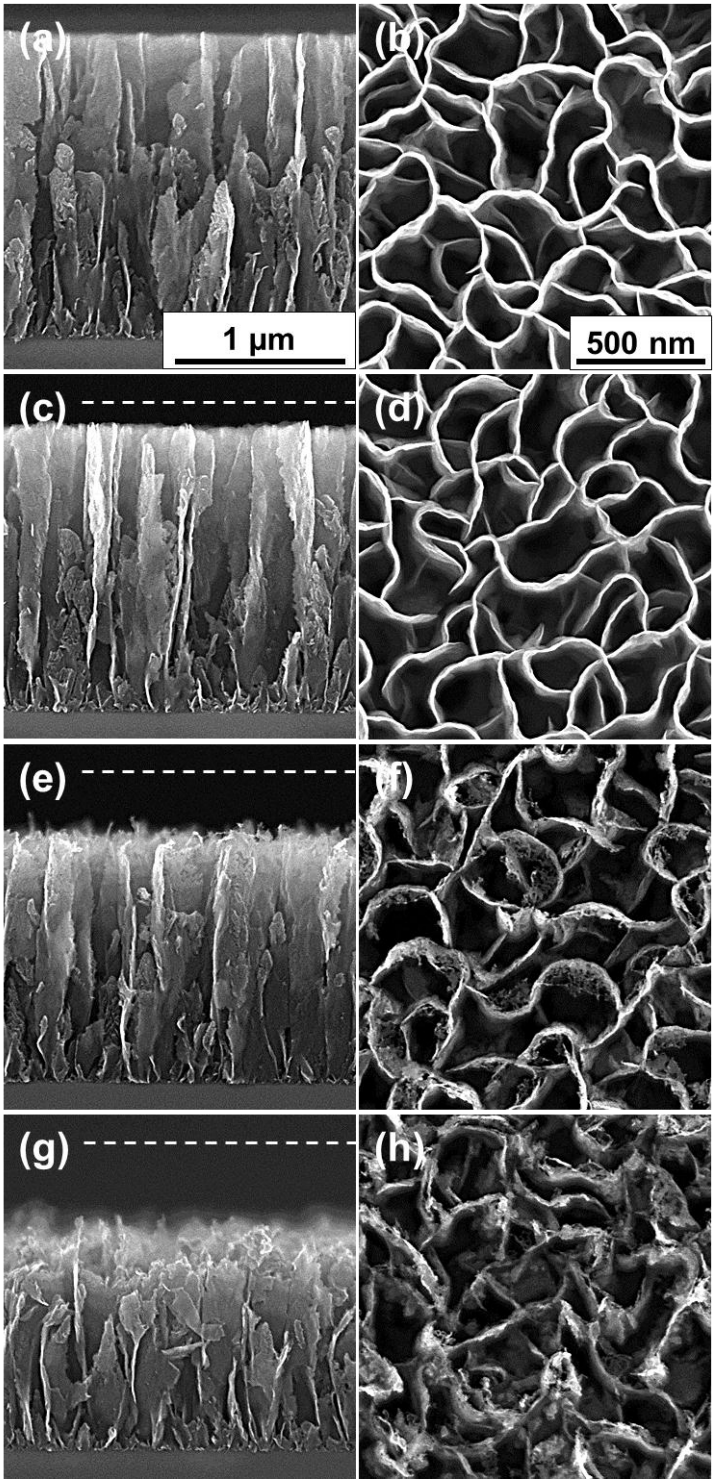


Fig. 3.10. Cross-sectional SEM images and each overhead view of CH-CNWs (a),(b) before and after the O treatment at (c),(d) 25, (e),(f) 300, and (g),(h) 700˚C for 5 min. The white dash lines in (c), (g), and (g) indicate the average height of the initial CH-CNWs before the treatment.

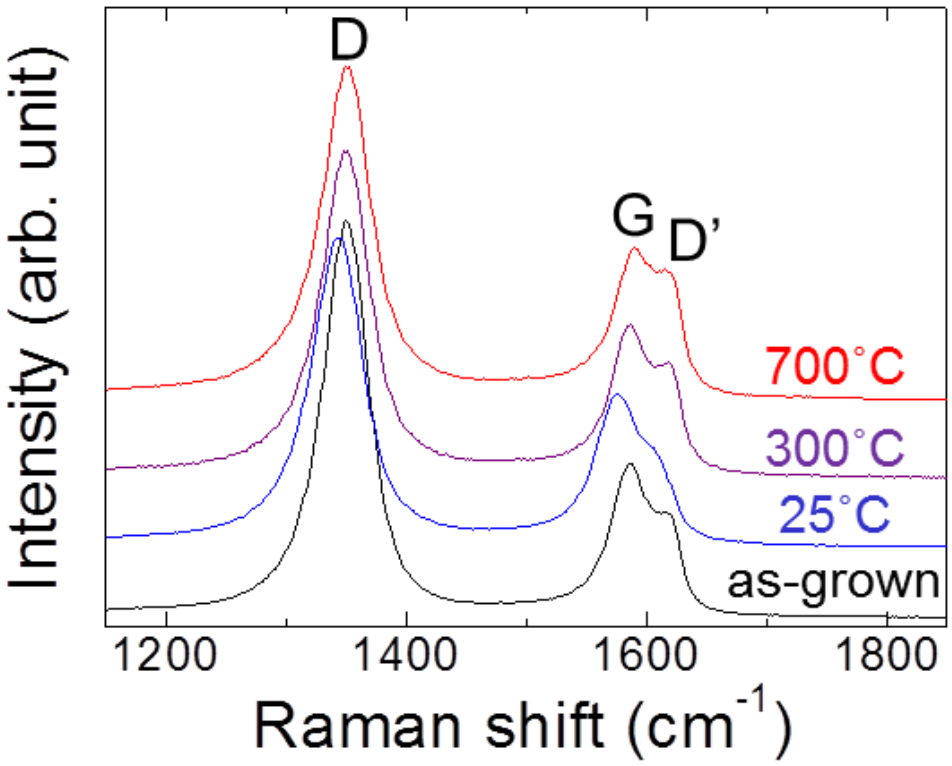


Fig. 3.11. Raman spectra for CH-CNWs before and after the O treatments at 25, 300, and 700˚C.

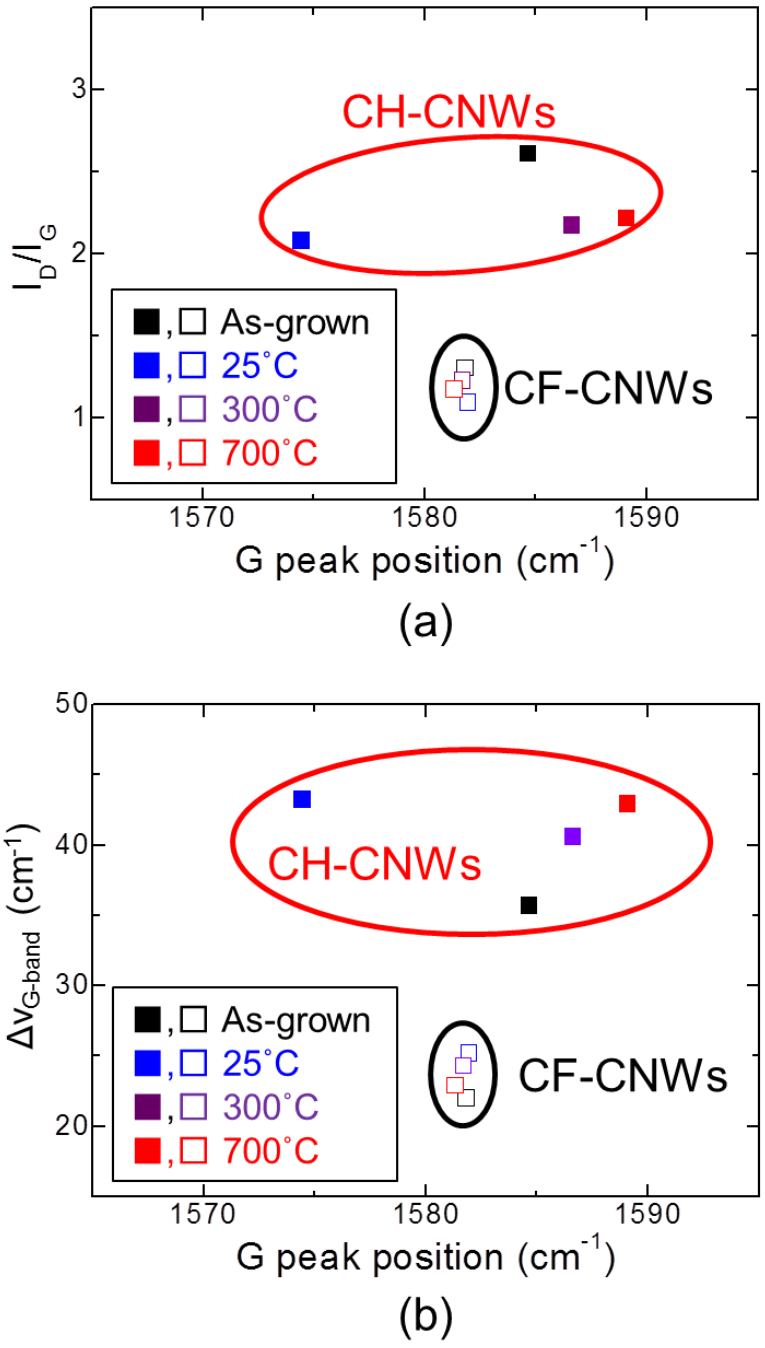


Fig. 3.12. (a) Peak intensity ratio of D-band to G-band, $I_D/I_G$, and (b) FWHM of G-band as a function of G peak position in the Raman spectra of CF- and CH-CNWs before and after O treatments.

## 3.5 Discussion about reaction with atomic oxygen in structures of CNWs

The selective etching of the top edge of CNWs employing oxygen atoms is modeled with a proposed mechanism as schematically shown in Fig. 3.13. The hierarchy of the CNW structure is shown in Fig. 3.13(a). The CNWs have a mazelike structure in which the bending or branching walls are almost continuous crytallographically, which leads to the cross-sectional view of one wall with the edges only on the top. The top edge is based on graphene edges which are highly-reactive to various chemical species as mentioned in Section 1.3.2. The CNW surface possibly contains several domain boundaries on the (002) graphite plane on the basis of winding planes with crystallographic dislocations and distortions [21].

In Fig. 3.13(b), the reaction with oxygen atoms is explained as follows: oxygen atoms are dominantly adsorbed on the CNW edge and surface without the formation of volatile products or desorption at room temperature. Namely, the atomic oxygen exposure at relatively low temperature readily induces oxygen-covered surfaces. On the other hand, at higher temperatures, not only does the formation of volatile products become a dominant reaction at the edge, but also reactions such as desorption, recombination of oxygen atoms, and secondary formation of volatile products by desorbed oxygen occur favorably on the wall surface [6,22-26]. Especially, the formation of CO or $CO_2$ preferentially occurs on the top edges highly-reactive to O atoms, where the rate-determining process for the progression of etching is adsorption of O atoms. As a result, while the etching from the reactive edges of CNWs is enhanced,

the amount of adsorbed oxygen decreases on the CNW surface as well as at the edge as shown in Fig. 3.13(c).

The oxidative reactions are consistent with the results from the SEM observations and XPS analysis. The above oxidative processes can result in the selective etching of the top edges of CNWs without formation of the pits and etching of the domain boundaries over the graphene planes on the wall surfaces. Our interpretation of the oxidation suggests that almost no in-plane graphene edge such as vacancies exist on the CNW surfaces. This provides the possibility for realizing the selective oxidation of the graphene edge without modification of the six-membered ring plane of planar graphene.

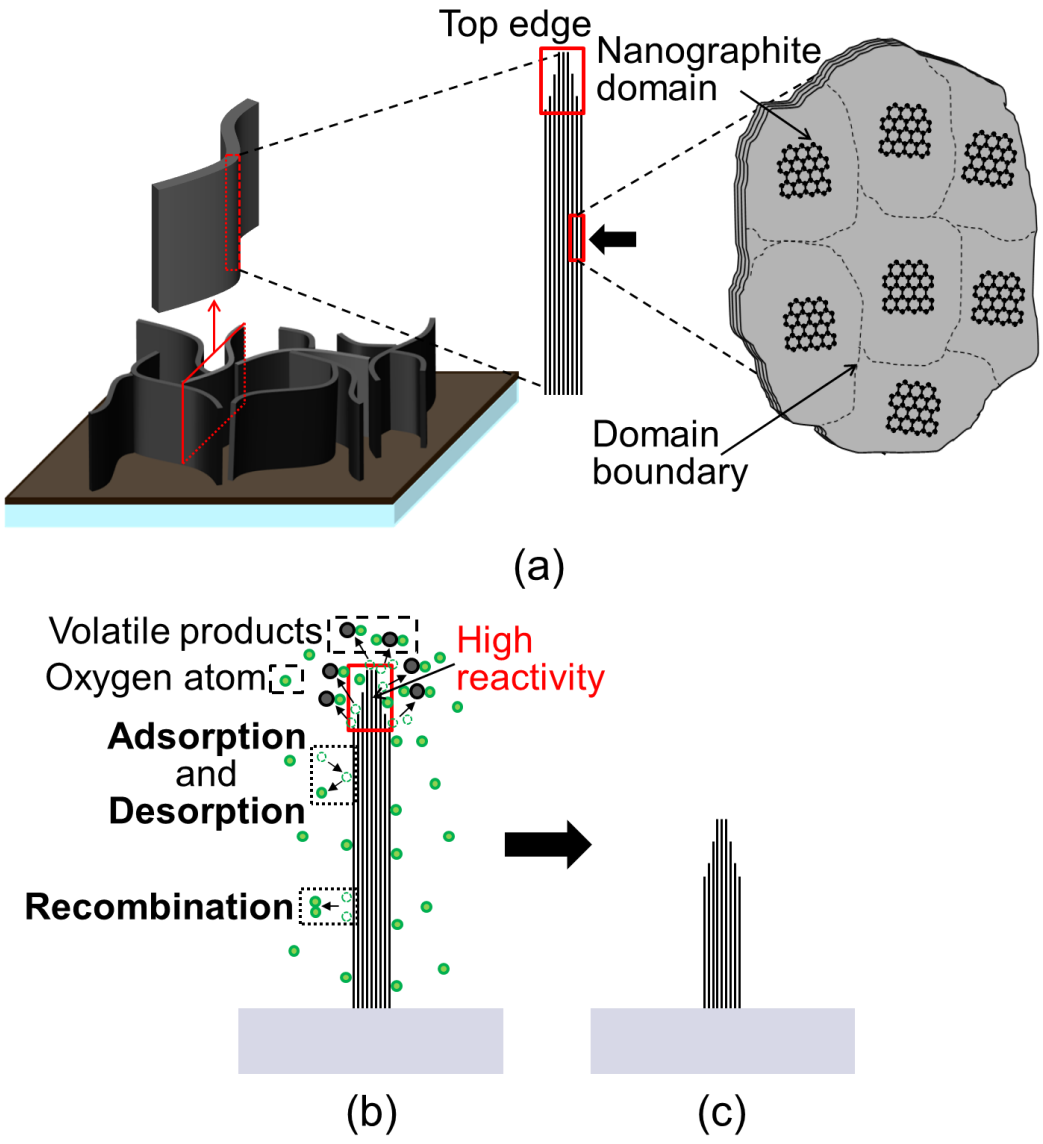


Fig. 3.13. (a) Structural model of CNWs and (b), (c) reaction models of oxidation with O atoms in the structure.

## 3.6 Summary

We investigated the effects of oxidative reactions with atomic oxygen (O) on the structures of CNWs. CNWs were exposed to O atoms generated by an inductively-coupled $O_2$ plasma. The CNWs were selectively etched from the top edges with almost no etching on the wall surface. The preferential reactions with O atoms induced a kind of amorphization through oxidative chemisorption and etchings mainly on the top edges, but its influences on the total crystallinity were small. Activation energy and reaction probability for the reaction with O atoms were also estimated for the etching from the top edges using the temperature dependence. As a result, it was found that the etching reaction with O atoms proceeded with almost no barrier (the activation energy of about 60 meV) and preferentially and effectively removed the carbon atoms on the top edges of CNWs. This also indicates that the rate-determining process for the oxidative etching from the top edges of CNWs is adsorption of O atoms. XPS analysis also indicated that almost no surface oxide layers was formed by the oxidation reaction with heating due to the dominant etching reaction or desorption of adsorbed oxygen and the promotion of recombination at higher temperatures.

We also investigated the influences of the crystallinities of CNWs on the oxidative reaction with O atoms by comparing two types of CNWs with significantly different crystalline structures. The lower crystallinities of graphene sheets and lower-crystallized layered structure with larger lattice spacing and smaller crystallite size in graphite (002) lattice enhanced the etching reaction from the top edges of CNWs and chemisorption with O atoms and caused the rougher and amorphous surface morphologies. However, there was almost no morphological change in the wall surfaces, which means such

crystallinities hardly affect the selectivity of the reaction with O atoms in CNWs.

# References

[1] F. J. Vastola, P. L. Walker, and J. P. Wightman: Carbon **1** (1963) 11.

[2] H. Marsh, T. E. O'Hair, R. Reed, and W. F. K. Wynne-Jones: Nature **198** (1963) 1195.

[3] C. E. Gleit, W. D. Holland, and R. C. Wrigley: Nature **200** (1963) 69.

[4] H. B. F. Gow and W. R. Marsh: USAEC Report TID-7597 **1** (1961) 16.

[5] G. R. Hennig, G. J. Dienes, and W. L. Kosiba: Proc. Second Int. Conf. on the Peaceful Uses of Atomic Energy **7** (1958) 301.

[6] H. Marsh, T. E. O'Hair, and W. F. K. Wynne-Jones: Trans. Faraday Soc. **61** (1965) 274.

[7] C. Wong, R. T. Yang, and B. L. Halpern: J. Chem. Phys. **78** (1983) 3325.

[8] H. Nagai, M. Hiramatsu, M. Hori, and T. Goto: Rev. Sci. Instrum. **74** (2003) 3453.

[9] R. T. Yang and C. Wong: J. Chem. Phys. **75** (1981) 4471.

[10] J. R. Hahn: Carbon **43** (2005) 1506.

[11] P. M. Ajayan, T. W. Ebbesen, T. Ichihashi, S. Iijima, K. Tanigaki, and H. Hiura: Nature **362** (1993) 522.

[12] A. L. Koh, E. Gidcumb, O. Zhou, and R. Sinclair: ACS Nano **7** (2013) 2566.

[13] T. Mori, M. Hiramatsu, K. Yamakawa, K. Takeda, and M. Hori: Diamond and Related Materials **17** (2008) 1513.

[14] A. C. Ferrari and J. Robertson: Phys. Rev. B **61** (2000) 14095.

[15] A. C. Ferrari and J. Robertson: Phys. Rev. B **64** (2001) 075414.

[16] S. Tinck and A. Bogaerts: Plasma Sources Sci. Technol. **20** (2011) 015008.

[17] Y. Xie and P. M. A. Sherwood: Chem. Mater. **2** (1990) 293.

[18] M. Hiramatsu, K. Shiji, H. Amano, and M. Hori: Appl. Phys. Lett. **84** (2004) 4708.

[19] A. Yoshida, Y. Kaburagi, and Y. Hishiyama: Carbon **44** (2006) 2333.

[20] H. Zhou, C. Qiu, F. Yu, H. Yang, M. Chen, L. Hu, Y. Guo, and L. Sun: J. Phys. D: Appl. Phys. **44** (2011) 185404.

[21] K. Kobayashi, M. Tanimura, H. Nakai, A. Yoshimura, H. Yoshimura, K. Kojima, and M. Tachibana: J. Appl. Phys. **101** (2007) 094306.

[22] H. Harker, C. Jackson, and W. F. K. Wynne-Jones: Proc. Royal. Soc. London, Ser. A **262** (1961) 328.

[23] T. Sun, S. Fabris, and S. Baroni: J. Phys. Chem. C **115** (2011) 4730.

[24] P. G. Dickens and M. B. Sutcliffe: Trans. Faraday Soc. **60** (1964) 1272.

[25] R. Larciprete, S. Fabris, T. Sun, P. Lacovig, A. Baraldi, and S. Lizzit: J. Am. Chem. Soc. **133** (2011) 17315.

[26] E. X. Zhang, A. K. M. Newaz, B. Wang, C. X. Zhang, D. M. Fleetwood, K. I. Bolotin, R. D. Schrimpf, S. T. Pantelides, and M. L. Alles: Appl. Phys. Lett. **101** (2012) 121601.

# Chapter 4

# Effects of ion irradiation to CNWs on reaction with radicals in oxygen plasma

## 4.1 Introduction

Plasma etching is one of promising techniques for designing graphene nanostructures such as Hall bars and nanoribbons [1,2]. On the other hand, the plasma etching is also used to form disorders on a graphene plane affecting its various properties as described in Section 1.4. In particular, oxygen ($O_2$) plasma can induce some effects on characteristics and properties such as Raman scattering, surface morphologies, field effect conductivity, photoluminescence, thermopower, and electronic properties [3-9]. While the plasma-induced disorders, functional groups, and their effects on properties have not been fully characterized, some structural studies such as Raman spectroscopic evaluations suggest crystallographic evolutions with progressing the plasma exposure.

The introduction of disorders by $O_2$ plasma etching can induce a gradual evolution

from the $sp^2$-bonded carbon network of graphene into amorphous carbon with a relatively large amount of $sp^3$ bonding [10,11]. This evolution consists of two main regimes with increasing the amount of disorders. One is a so-called ‘graphite to nanocrystalline graphite’ (or ‘low-defect-density regime’) phase as a lower level of defected graphene and the other is a so-called ‘nanocrystalline graphite to mainly $sp^2$ amorphous carbon’ phase (or ‘high-defect-density’ regime) as a higher level of defected graphene [10,11]. These crystallographic changes can easily occur due to ion-assisted oxidative reaction with oxygen-related radicals during reactive ion etching (RIE) using $O_2$ plasma.

Ion irradiation itself can be used to modify the morphologies of graphene planes by introducing specific defects and to cut graphene sheets. The types and concentrations of defects on graphene can be identified using different ion irradiations with various energies and a wide range of the incident angle [12]. The incident angle affects sputtering processes of carbon (C) atoms from the six-membered rings and amorphized areas where there are a large amount of disorders with $sp^3$ bonding. Furthermore, relatively high-energetic ions with an optimized incident angle can improve the resilience of the hexagonal rings. In addition, even noble gas ion irradiation can provide insights into the response of graphene to irradiation with other chemical species [13].

However, while the $O_2$ plasma RIEs and ion irradiations have been carried out on the plane of planer graphene, such etching characteristics and effects of ion irradiation on the edge have not been experimentally studied yet. Because CNWs consist of vertically standing graphene sheets and have top edges directed normal to the surface, the top edges based on graphene edges can be easily and preferentially exposed to ions as well as reactive neutral species. In addition, there are various characteristic

nanostructures such as bends and branches composed of graphene sheets in CNWs. Accordingly, studies on $O_2$ plasma RIEs and ion irradiations for CNWs give us a new knowledge on reaction processes by oxygen-related species and ions in edge-sensitive vertically-aligned graphene sheets and characteristic graphitic nanostructures including defects such as bends and branches.

In this chapter, we investigated the effects of ion irradiations on the reaction with oxidative radicals such as oxygen (O) atoms in the structures of CNWs. Firstly, the RIE using capacitively-coupled $O_2$ plasma was conducted for CNWs. The etch rate and morphological changes were evaluated and compared with the case of atomic oxygen treatment. Moreover, to identify the effects of O-related ions such as $O_2^+$, the dependence of the $O_2$ concentration in $O_2$/Ar plasma where Ar gas acted as promotion of gas dissociation and novel gas ions was investigated. We also focused on the more limited reaction with O atoms and Ar ions to clarify the effects of combination of O atoms with ion irradiation on the edges and planes in CNWs. The ion irradiation area was controlled by changing the ion incident angle to the wall surface.

## 4.2 Experimental details

CNWs were fabricated on Si substrates using the RI-PECVD system as described in Subsection 2.1.1. The flow rates of $C_2F_6$ as carbon source gas and $H_2$ were 50 and 100 sccm at the total pressure of 173 Pa. The VHF and microwave powers were 270 and 250 W. The substrate temperature was about 630˚C. The typical deposition time was 30 min. After the growth of the CNWs, the CNWs were etched by using a capacitively

coupled plasma reactor. A very high frequency (VHF, 60 MHz) power of 500 W was applied to the top electrode and a low frequency (LF, 2 MHz) power of 500 W was applied to the bottom electrode. The sample was placed on the bottom electrode with an electrostatic chucking system in order to maintain the sample temperature by circulating coolant at 20 ˚C. Pure oxygen gas was introduced into the chamber with the flow rate of 200 sccm and the pressure was maintained at 2 Pa by the automatic pressure controller. For $O_2$/Ar plasma, $O_2$/Ar mixture gases was also introduced with the total flow rate of 200 sccm and the $O_2$ concentration was changed from 2 to 100%. The sample of CNWs was etched for 1 min.

In Section 4.4, to obtain CNWs with as vertical orientation as possible, CNWs were synthesized on Si substrates using the RI-PECVD with $CH_4$ gas as a carbon source gas. The flow rates of $CH_4$ and $H_2$ were 100 and 50 sccm at the total pressure of 1 Pa. The VHF and microwave powers were 300 and 400 W. The substrate temperature was about 600˚C. The deposition time was 15 min. After the synthesis, the CNWs were irradiated with O atoms and Ar ions using the multi-beam plasma irradiation system as described in Subsection 2.1.2. $O_2$ and Ar gases were individually introduced into the radical source and ion source with the both gas flow rate of 10 sccm and the total pressure in the chamber was 0.1 Pa. The RF powers for the radical and ion sources were 500 and 400 W. The ion acceleration voltage was 200 V. The substrate temperature was 300˚C. The irradiation time was 5 to 10 min. As shown in Fig. 4.1, the ion-irradiated region on the wall surface was controlled by changing an ion incident angle ($\theta$) with adjusting a setting angle of the sample. The length of ion-irradiated area from the top of CNW, $L$, can be calculated using the simple equation

$$L = \frac{D}{tan\,\theta}, \tag{4.1}$$

where $D$ is the average distance between each wall in CNWs. When the height and $D$ were approximately 900 nm and 200 nm, respectively, and $\theta$ was 80˚, the calculated $L$ was about 1100 nm which was theoretically enough for ions to reach the whole area of the wall surfaces.

After the RIE and irradiation of O atoms and Ar ions ($O+Ar^+$ irradiation), the morphologies of the CNWs were observed by scanning electron microscopy (SEM). The crystalline structures of CNWs were also evaluated using Raman spectroscopy. For the $O+Ar^+$ irradiation, the chemical bonding states of carbon and adsorbed O atoms were evaluated by X-ray photoelectron spectroscopy (XPS) with changing the take-off angle of photoelectrons, $\varphi$.

Optical emission spectroscopy (OES) was used for evaluating the relative densities of O atoms in the $O_2$/Ar plasma. The emission line of O atoms at 778 nm was measured. A small amount of Xe gas was added to the plasma with the flow rate of 5 sccm and the Xe* emission line at 823 nm was also measured for an actinometer to obtain information on the electron density and temperature in the plasma.

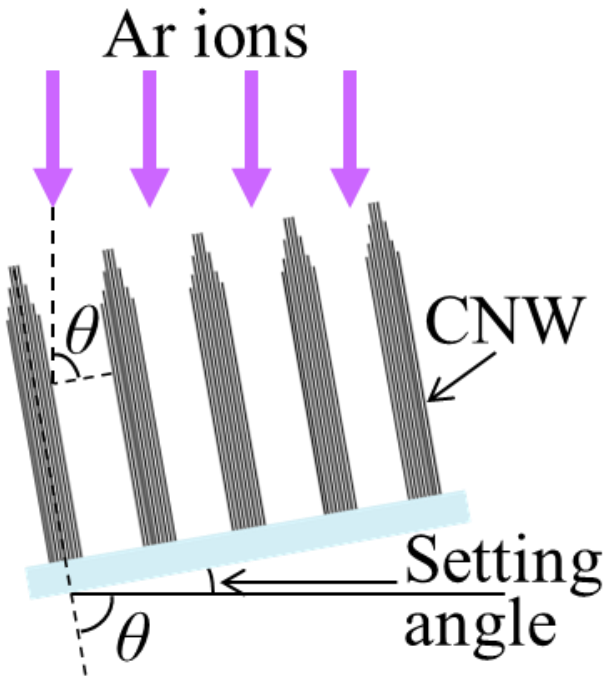


Fig. 4.1. Illustration of a schematic of ion irradiations to CNWs.

# 4.3 Reactive ion etching of CNWs using $O_2$ plasma

## 4.3.1 Etching characteristics of pure $O_2$ plasma etching of CNWs

We examined reactive ion etching (RIE) reactions using $O_2$ plasma. Figure 4.2 shows SEM oblique images of each cross section of (a) an initial sample with a height of 1200 nm, and (b) a sample etched by $O_2$ plasma for 1 min. The top edges of the CNWs were sharpened and formed spear-like structures. The height of the CNWs decreased drastically to approximately 400 nm as the spears were ignored. In a previous study, our research group reported the experimental results of the RIE of CNWs using $N_2/H_2$ plasma [14]. We recognized that the RIE properties were much different between the $N_2/H_2$ plasma and $O_2$ plasma.

Interestingly, the $O_2$ plasma RIE induced a kind of selective etching of the top edges of the CNWs depending on the characteristic structure. Namely, because the branching points of the walls have a different crystalline structure from that of the other part of the wall due to formation of a joint between graphene edges and six-membered ring plane, these may be harder to be etched off. For RIE, an ion bombardment is a dominant factor in promotion of etching reactions. If the ion energy necessary for etching is different between the branching points and other parts, the etch rate can differ. On the other hand, the etching reaction at room temperature is hard to occur without ion bombardments, which means almost no etching on the wall surface. These facts lead a kind of anisotropic etching. These are characteristic differences from the atomic oxygen treatments in which highly-reactive atomic oxygen can react with the top of CNWs regardless of its crystalline structures.

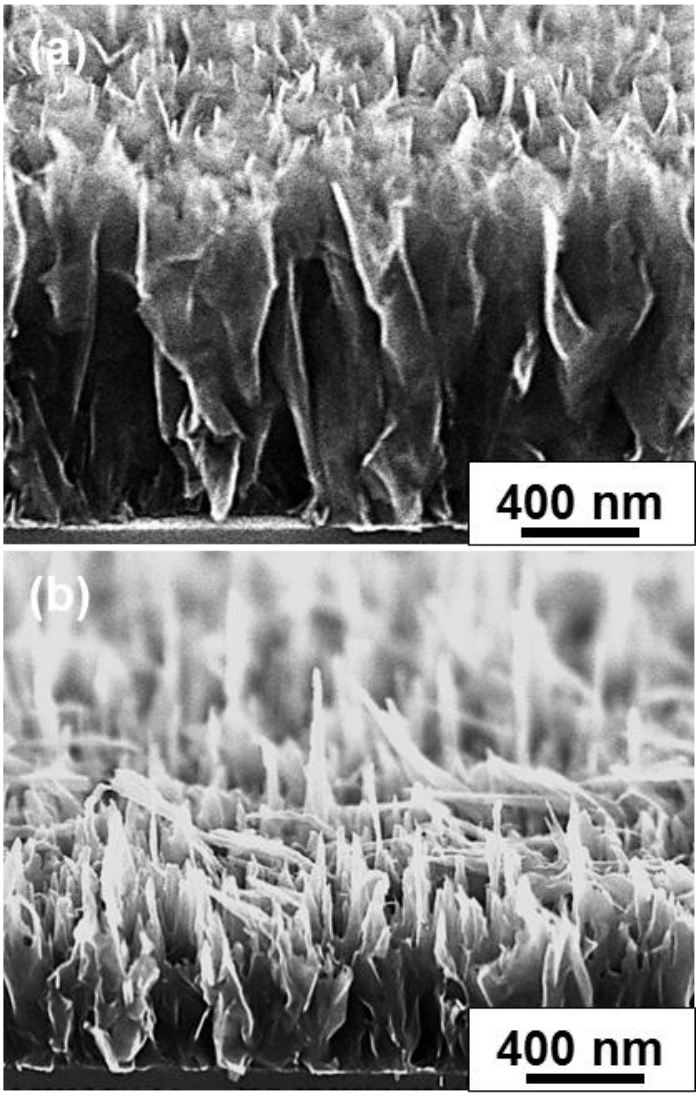


Fig. 4.2. Cross-sectional oblique SEM images of the CNWs (a) before and (b) after $O_2$ plasma reactive ion etching (RIE).

### 4.3.2 Dependence of $O_2$ concentration in $O_2$/Ar plasma on RIE reactions in CNWs

To clarify the effects of radicals and ions in $O_2$ plasma, we also carried out the RIE using $O_2$/Ar plasma with changing the $O_2$ concentration, which could mainly change the plasma density and species contributing to the RIE reaction. Figure 4.3 shows the oblique SEM images of cross sections of the CNWs after the $O_2$/Ar plasma etchings with changing the $O_2$ concentration. The average height of CNWs decreased to approximately 400 nm as a maximum difference with increasing the $O_2$ concentration. The morphology of the top edges of CNWs dramatically changed and formed the spear-like structures at the $O_2$ concentration of more than 8%. The average height of the spears strongly depended on the $O_2$ concentration. In addition, the etch rates were estimated with the average height of CNWs as the spears were ignored. As shown in Fig. 4.4, while the etch rate drastically increased to approximately 800 nm/min at the $O_2$ concentration of up to 25%, that was almost constant at the more $O_2$ concentrations. These results mean that the oxidative etching of CNWs in the vertical direction can occur due to synergetic reactions of O-related radicals and ions.

Figure 4.5 shows the emission intensity ratios of O 778 nm line to Xe 823 nm line, $I_O/I_{Xe}$ as relative densities of O atoms as a function of $O_2$ concentration. Additionally, the emission intensity of Xe 823 nm line, $I_{Xe}$, as a function of $O_2$ concentration was also shown in Fig. 4.5. $I_{Xe}$ decreased with increasing $O_2$ concentration, which means a decrease in the plasma (electron) density. This phenomenon can be caused by easily-dissociation of Ar gas which may also promote the $O_2$ gas dissociation in the lower $O_2$ concentrations. On the other hand, although changes in the electron

temperature may be one of factors in such phenomenon, the former is considered to be reasonable because there was no change in the intensity ratios of each emission line in the spectra. In contrast, $I_O/I_{Xe}$ almost linearly increased with increasing the $O_2$ concentration, which means an increase in the density of O atoms. These results suggest that while the increase in the O atom density contributes to promote the etching reaction on the top edges of CNWs at the $O_2$ concentration of up to 25%, at the higher $O_2$ concentrations, the decrease in the plasma density affecting the ion density may retard the further progression of the etching reaction and saturate the etch rate.

Raman spectra of the CNWs before and after the $O_2$/Ar plasma etchings were measured. The peak intensity ratios of D-band to G-band ($I_D/I_G$) and full width at half maximum of G-band ($\Delta\nu_{G\text{-band}}$) were determined by curve fitting with Lorentzian peak shape for each Raman spectrum. Figure 4.6 shows the values of $I_D/I_G$ and $\Delta\nu_{G\text{-band}}$ as a function of $O_2$ concentration, in which each initial value was shown by the red lines. $I_D/I_G$ decreased from 2.60 to 2.19 after the plasma etching at the lowest $O_2$ concentration of 2% and further decreased gradually up to 1.91 with increasing $O_2$ concentration as shown in Fig. 4.6(a). On the other hand, $\Delta\nu_{G\text{-band}}$ drastically increased from 40 to 80 $cm^{-1}$ after the plasma etching at the lowest $O_2$ concentration of 2%, but the variation of $\Delta\nu_{G\text{-band}}$ drastically decreased to 66 $cm^{-1}$ at the $O_2$ concentration of 10% and then gradually decreased up to 60 $cm^{-1}$ after the pure $O_2$ plasma etching.

These tendencies of $I_D/I_G$ and $\Delta\nu_{G\text{-band}}$ in the Raman spectra suggest that the $O_2$/Ar plasma etchings can induce amorphization mainly on the top edges, which may strongly depend on the amount of ions contributing the RIE reactions. However, such amorphization of graphitic structures in CNWs may be classified into results from physically- and chemically-induced disorders by the tendencies of $I_D/I_G$ and $\Delta\nu_{G\text{-band}}$ in

the Raman spectra. At the lowest $O_2$ concentration, the highest-density ions are irradiated to the CNWs and physically break the $sp^2$ bond network leading amorphization, which results in the smallest variation of $I_D/I_G$ and largest variation of $\Delta\nu_{G\text{-band}}$. In contrast, during the pure $O_2$ plasma exposure, not only ion bombardments but also O-related radicals physically and chemically induce disorders in the graphitic structures of CNWs. Especially, oxidative chemisorption may easily occur the edges and defects in CNWs. Such collapses of relatively-high graphitization region and chemically-modification of defected region including the edges may result in the largest variation of $I_D/I_G$ and smallest variation of $\Delta\nu_{G\text{-band}}$.

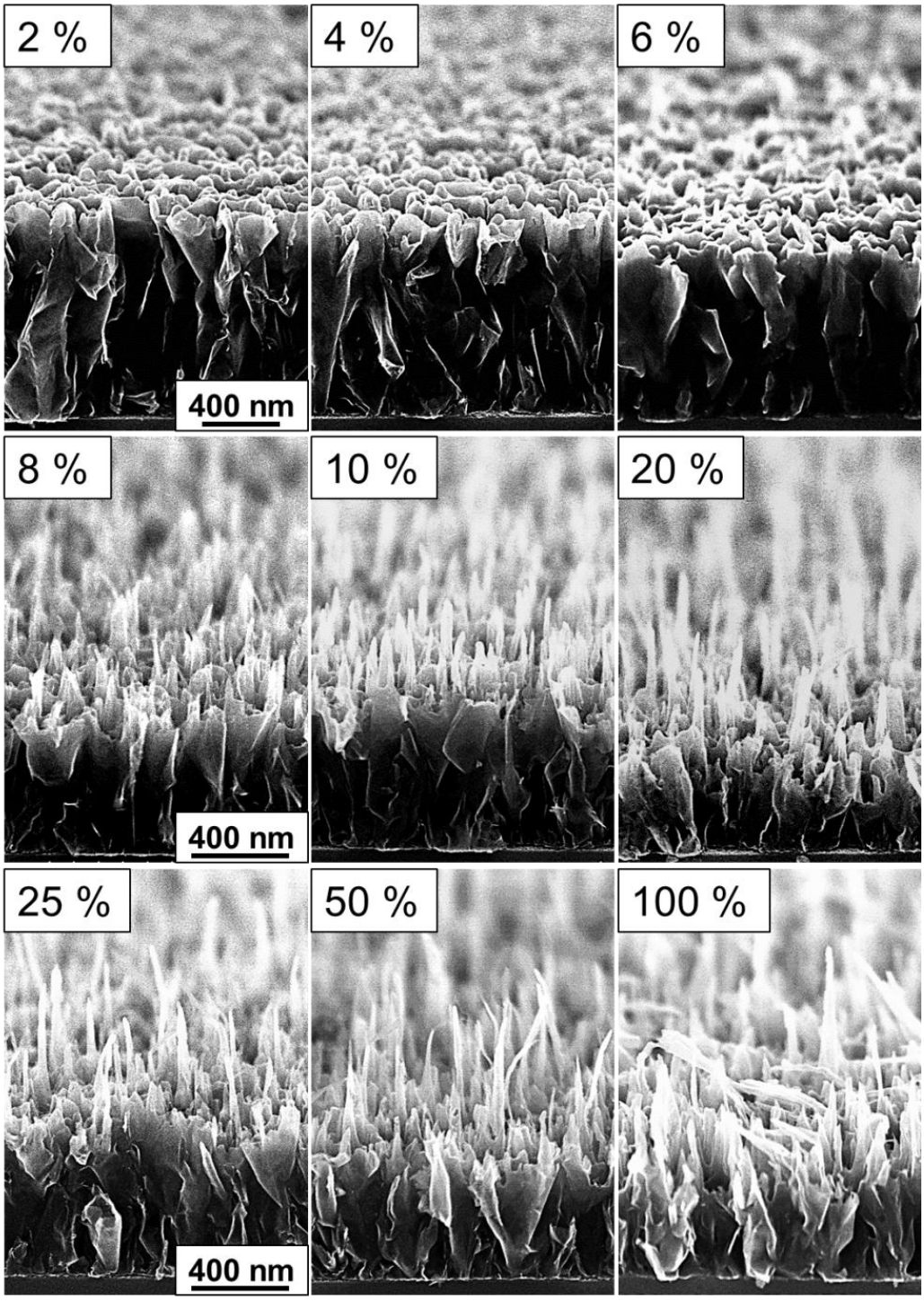


Fig. 4.3. Oblique SEM images of cross sections of the CNWs after the $O_2$/Ar plasma etchings with changing the $O_2$ concentration from 2 to 100%.

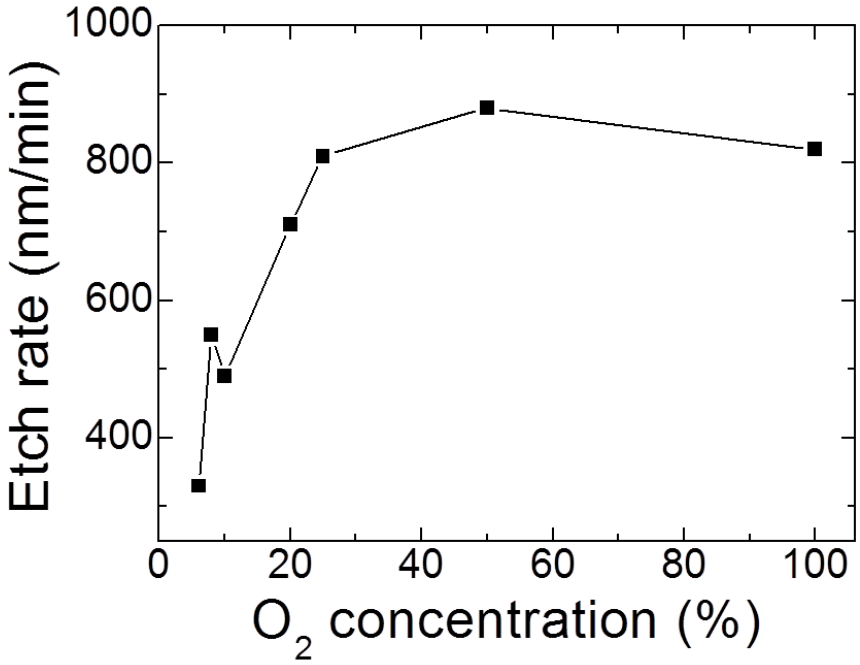


Fig. 4.4. Etch rates of the CNWs in the vertical direction as a function of $O_2$ concentration.

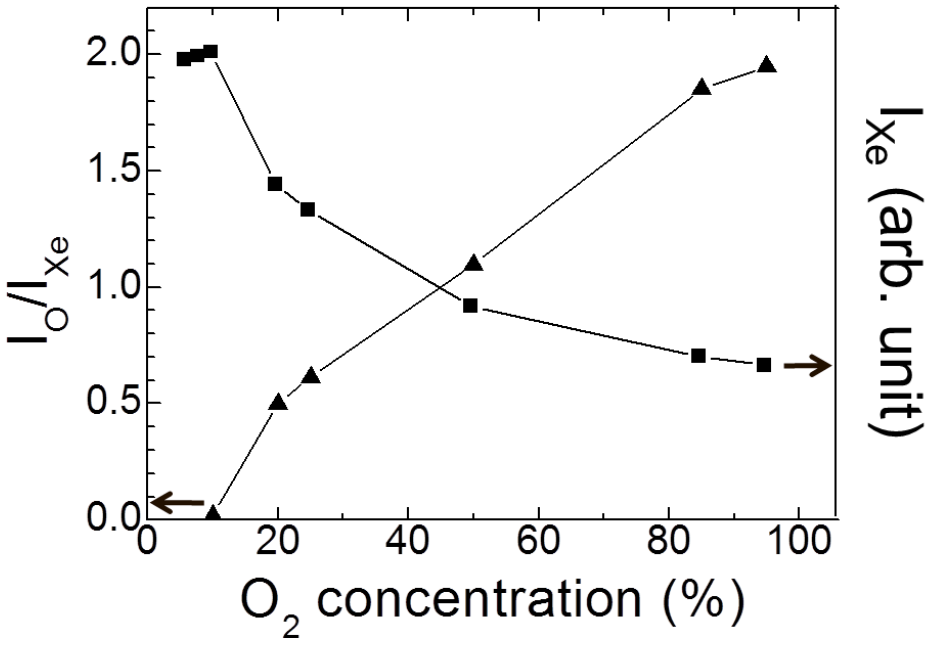


Fig. 4.5. Emission intensity ratio of O 778 nm line to Xe 823 nm line as a relative density of O atoms and emission intensity of Xe 823 nm line as a function of $O_2$ concentration.

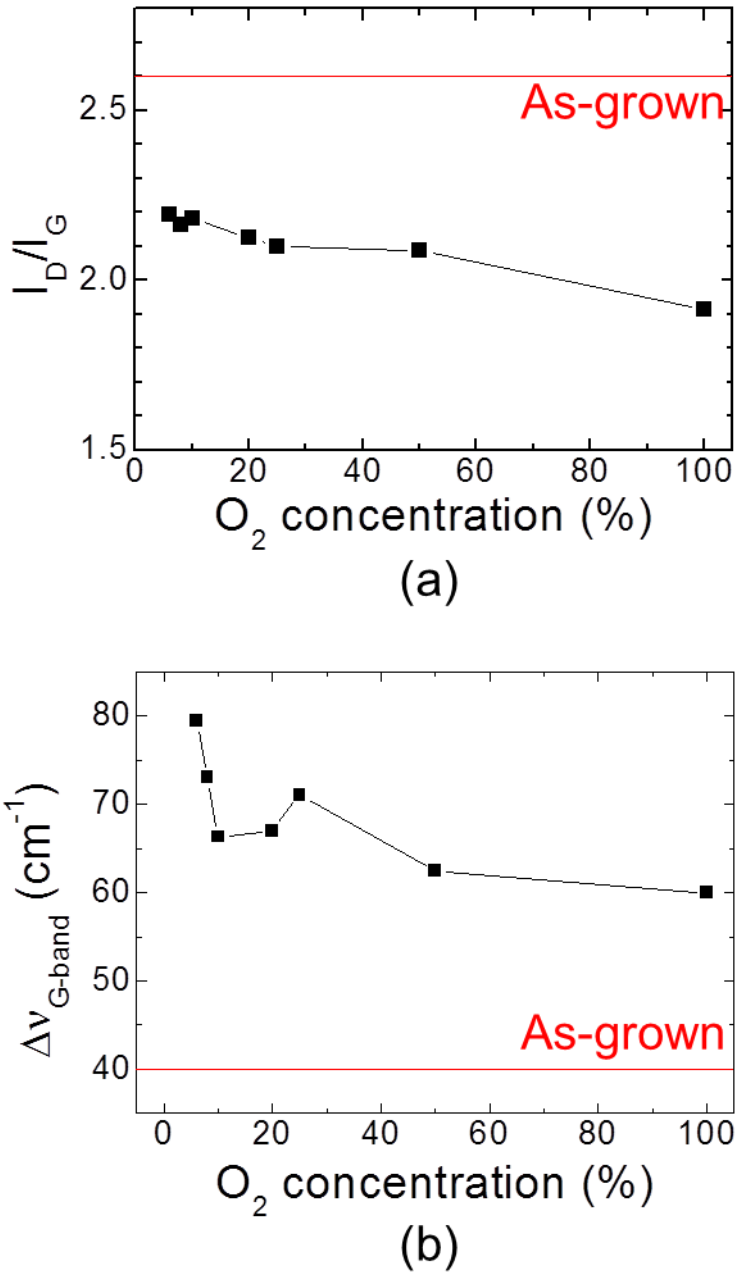


Fig. 4.6. (a) Peak intensity ratios of D-band to G-band ($I_D/I_G$) and (b) full width at half maximum of G-band ($\Delta\nu_{G\text{-band}}$) for the CNWs before and after the $O_2$/Ar plasma etching as a function of the $O_2$ concentration. The red lines indicate the initial values for the as-grown CNWs.

# 4.4 Control of edge and plane oxidation of CNWs employing O atom and Ar ion irradiations

## 4.4.1 Effects of grazing-incident ion on morphologies and crystalline structures

Firstly, we investigated the effects of ion irradiation vertically to CNW film surface on the reaction with oxygen (O) atoms. To suppress unwanted etchings from the top edges of CNWs, the CNWs were exposed to O atoms at 300˚C under the lower pressure than the case of Chapter 3. Figure 4.7 shows the cross-sectional SEM images and each overhead view with insets as lower-magnified views of the CNWs before and after the O atom and Ar ion ($O+Ar^+$) irradiations for 5 min. While the height of the CNWs exposed to only O atoms hardly changed under the conditions as shown in Fig. 4.7(c), that irradiated with both O atoms and Ar ions slightly but significantly decreased from 1000 nm to 950 nm as shown in Fig. 4.7(e). The morphologies of CNWs hardly changed even after the $O+Ar^+$ irradiations as shown in Fig. 4.7(d) and (f). However, we confirmed an enhancement of the etching reaction from the top edges of CNWs with O atoms due to Ar ion irradiation similarly to the RIE in Section 4.3. On the other hand, no spear was formed on the etched edges, which indicates that formation of such spears by the RIE may occur due to higher ion energy and contributions of molecular species.

Then, we also investigated the effects of ion irradiation to the wall surfaces of CNWs on the reaction with O atoms employing grazing-incident ions. The CNWs were irradiated with O atoms and Ar ions at the incident angle ($\theta$) of 80˚. Figure 4.8 shows

the cross-sectional SEM images and each tilted overhead view with insets as lower-magnified overhead views of the CNWs before and after the $O+Ar^+$ irradiations at $\theta$ = 80 and 90˚ for 10 min. The height of CNWs decreased from 900 to 750 nm after the $O+Ar^+$ irradiation at $\theta$ = 90˚ as shown in Fig. 4.8(c). On the other hand, the height of CNWs irradiated at $\theta$ = 80˚ was approximately 700 nm in Fig. 4.8(e). Furthermore, there were obviously rougher surfaces of the edges and planes around the wall tops in the CNWs irradiated at $\theta$ = 80˚ as shown in Fig. 4.8(f). These results indicate that ion irradiation to the wall surfaces of CNWs can enhance the etching reaction with O atoms not only the wall surfaces but also on the top edges, which may be caused by formation of defects on the wall surface almost over the top to bottom.

The crystallinities of CNWs exposed with O atoms and Ar ions were also evaluated by Raman spectroscopy. Figure 4.9 shows the Raman spectra normalized with each G-band peak intensity for the CNWs before and after the $O+Ar^+$ irradiations at $\theta$ = 80 and 90˚ for 10 min. The relative peak intensity of D-band slightly decreased after $O+Ar^+$ irradiations. The value of $I_D/I_G$ decreased from 2.00 to 1.74 after the irradiation at $\theta$ = 80˚ whereas the value decreased to 1.84 after the irradiation at $\theta$ = 90˚. In the higher Raman shift region, the relative peak intensity of 2D-band also slightly decreased after the irradiations. These changes in Raman spectra for the CNWs mean that formation of disorders in the graphitic structures of CNWs and amorphization can be more readily enhanced by the larger amount of ions incident to the wall surfaces. The ions irradiated to the wall surfaces of CNWs contribute to etchings in both the vertical and parallel directions through the formation of disorders, which lead to decreases in the height and thickness and rougher surface morphologies on the edges and planes.

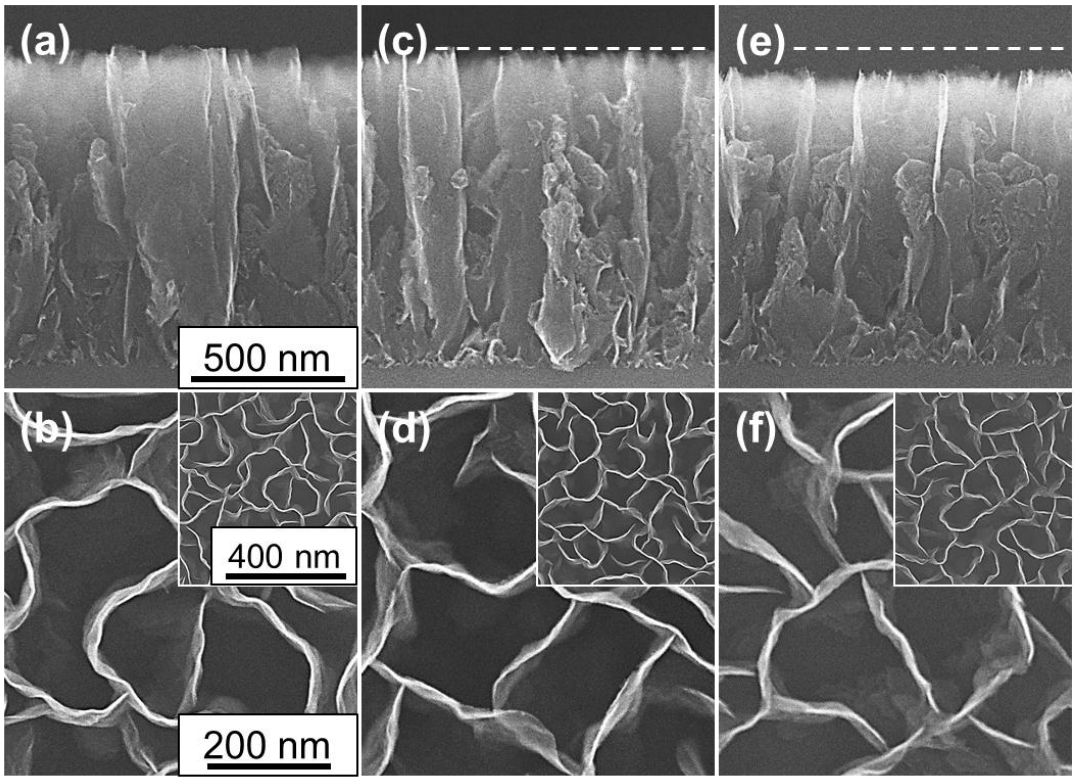


Fig. 4.7. Cross-sectional SEM images and each overhead view with insets as lower-magnified views of the CNWs (a),(b) before and after (c),(d) the O atom irradiation and (e),(f) O atom and Ar ion irradiation for 5 min.

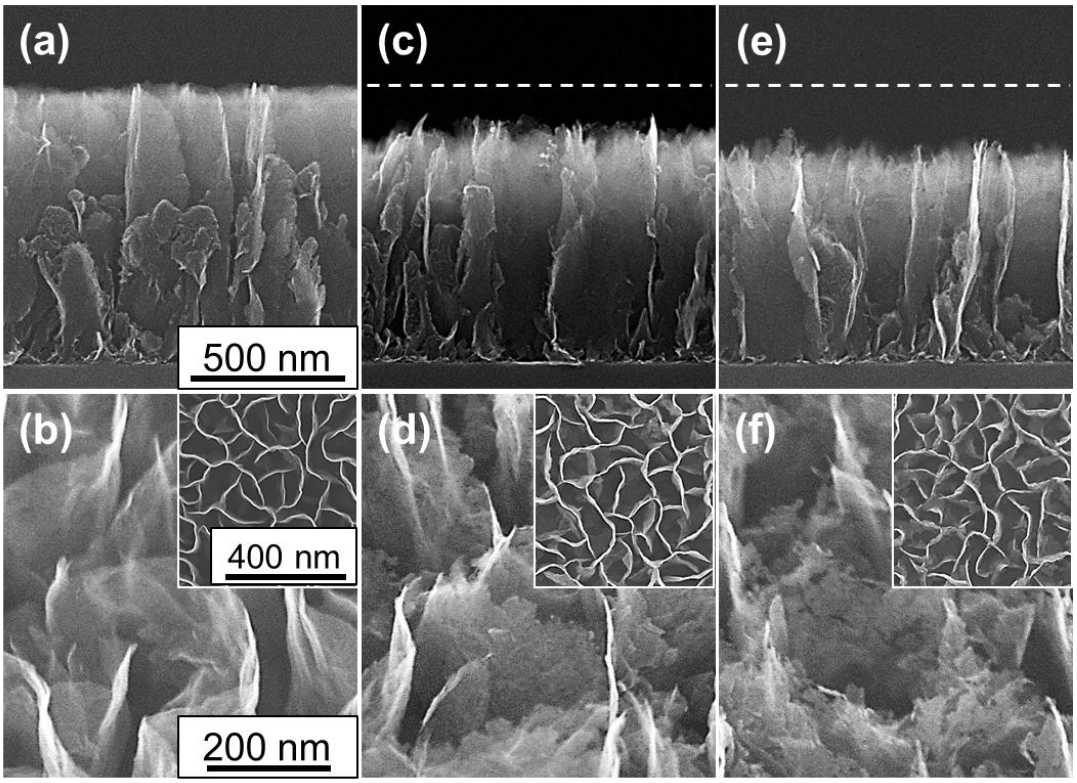


Fig. 4.8. Cross-sectional SEM images and each tilted overhead view with insets as lower-magnified overhead views of the CNWs (a),(b) before and after the $O+Ar^+$ irradiations at (c),(d) $\theta$ = 80 and (e),(f) 90° for 10 min.

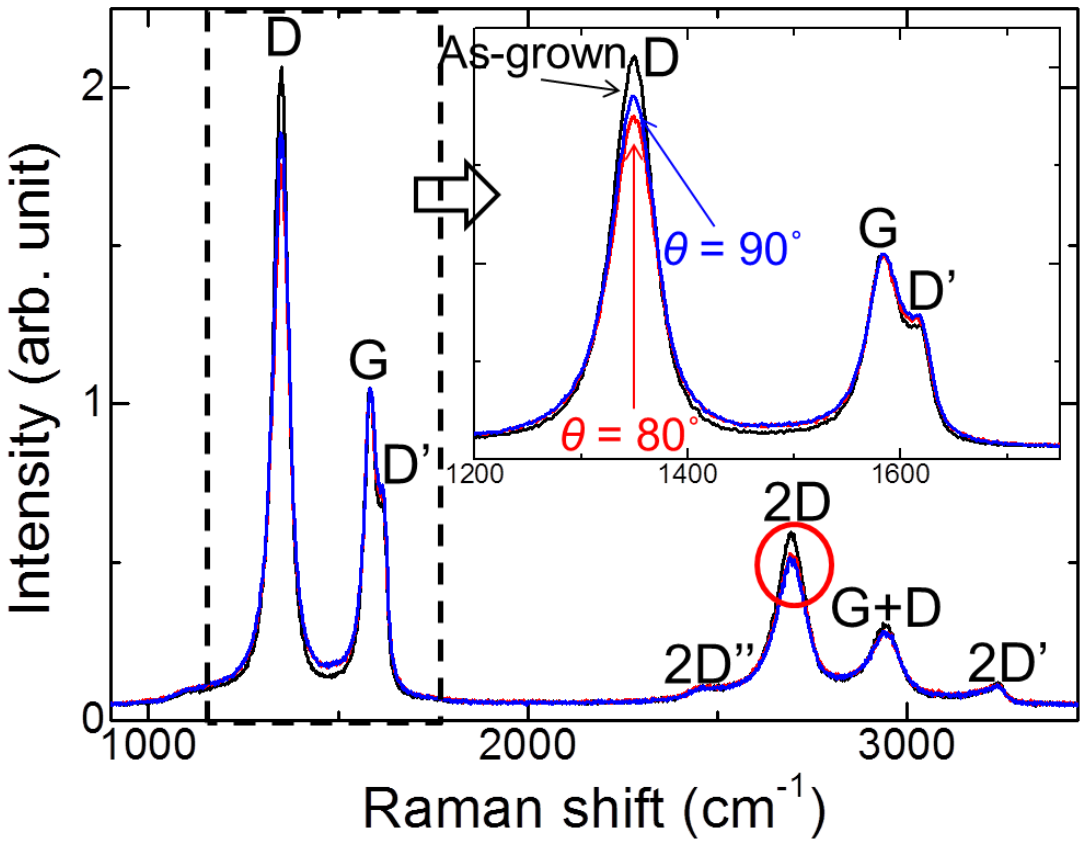


Fig. 4.9. Raman spectra for the CNWs before and after the $O+Ar^+$ irradiations at $\theta$ = 80 and 90° for 10 min. The inset shows the magnified spectra in the lower Raman shift region including D-, G-, and D'-band.

### 4.4.2 Surface chemical states on ion-irradiated areas in CNWs

To identify surface chemical changes such as adsorptions of oxidizing species in the CNWs, an XPS analysis was carried out at a take-off angle of photoelectrons, $\varphi$, of 8˚ and 90˚. It should be noted that the spectra at a smaller $\varphi$ means a chemical state near the top edges of CNWs are reflected. Figure 4.10 shows the C 1s and O 1s photoelectron spectra at $\varphi$ = 8˚, 90˚ for the CNWs before and after the $O+Ar^+$ irradiations at the ion incident angle $\theta$ = 80˚, 90˚ for 10 min. The O 1s peaks were expressed as the peak area ratios of O 1s to C 1s.

First, we focused on the O 1s peaks. In the case of the as-grown CNWs, the larger peaks was found at $\varphi$ = 8˚ compared with that at $\varphi$ = 90˚, which indicates larger amount of O atoms absorbed at the top edges. Focusing on the spectra at $\varphi$ = 8˚, after the irradiation at $\theta$ = 90˚, the peak area was smaller than that for the as-grown CNWs. At that time, the integrated peak intensity ratio of O 1s to C 1s, $I_O/I_C$, was calculated using the photoionization cross sections of each element, and the ratio slightly decreased from 0.07 to 0.05 after the irradiation. In contrast, the peak area at $\varphi$ = 8˚ increased after the irradiation at $\theta$ = 80˚ and $I_O/I_C$ ratio increased up to 0.15. On the other hand, for the spectra at $\varphi$ = 90˚, the peak areas increased from 0.03 to 0.07 and 0.11 after the irradiation at $\theta$ = 90˚ and 80˚, respectively.

In addition, each C 1s peak was decomposed into graphitic or amorphous C-C bonding peak and some oxide peaks such as C-OH or C-O-C, C=O, and O=C-OH by curve fitting assuming Gaussian-Lorentzian peak shapes after Shirley background correction. Then, the integrated peak intensity ratio of a sum of the oxide peaks to the total C 1s peak, $I_O'/I_C$, was calculated as shown in Table 4.1. Although $I_O'/I_C$ ratio

exhibited the almost same behavior as $I_O/I_C$ ratio, in the case of the irradiation at $\theta = 90^\circ$, $I_O'/I_C$ ratio for $\varphi = 8^\circ$ increased from 0.09 to 0.13 in contrast to the decrease in $I_O/I_C$ ratio. This inconsistency between $I_O/I_C$ and $I_O'/I_C$ ratios indicates that the amount of C-C bonds around the top edges of CNWs may decrease through bond breakings due to ion bombardments. These results indicate that Ar ion irradiations to the wall surface of CNWs can induce defects reactive to O atoms, whereas on the top edges, desorption of O atoms and other oxidative species as well as bond breakings of C-C bonds may easily occur due to heating and ion bombardments. Accordingly, it was found that combination with O atoms and Ar ions can selectively oxidize the top edges and wall surfaces of CNWs.

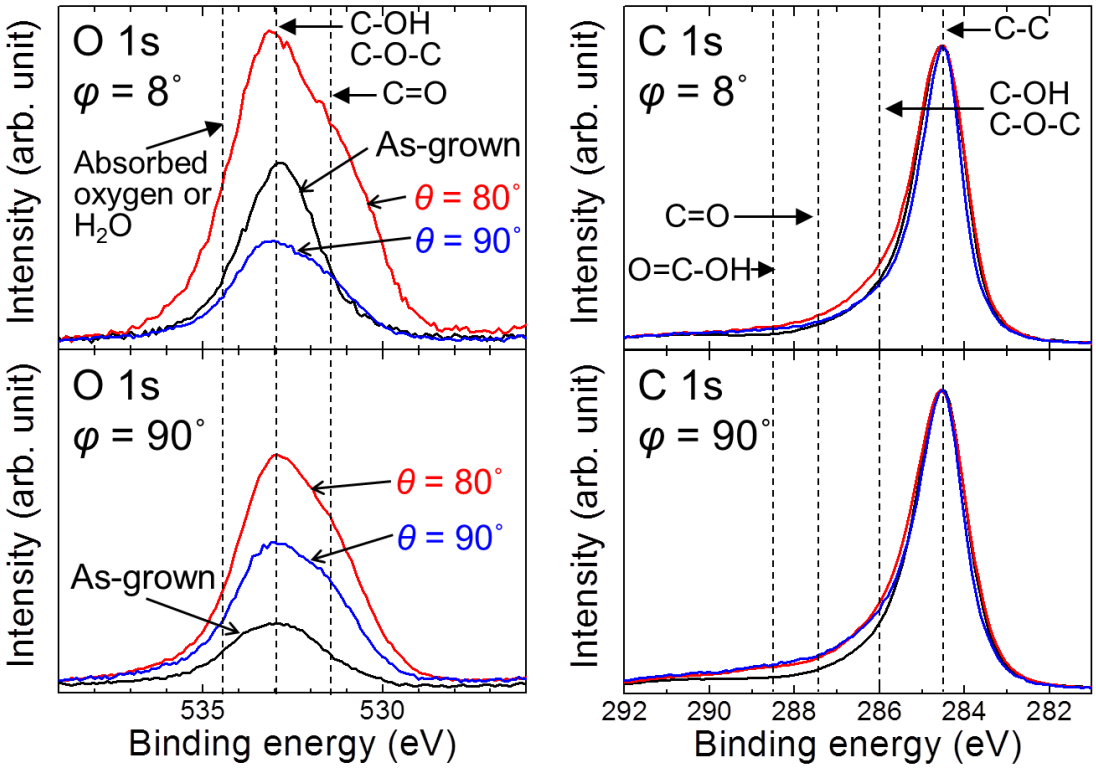


Fig. 4.10. C 1s and O 1s photoelectron spectra at $\varphi$ = 8°, 90° for the CNWs before and after the O+$Ar^+$ irradiations at $\theta$ = 80° and 90° for 10 min. The C 1s and O 1s peaks were normalized with the C 1s peak intensity and integrated peak intensity at each take-off angle, respectively.

Table 4.1. Integrated peak intensity ratio of O 1s to C1s, $I_O/I_C$, and that of a sum of the oxide peaks in each C 1s peak to the total C 1s, $I_O'/I_C$, for the CNWs before and after the O+$Ar^+$ irradiations at $\theta$ = 80° and 90°.

| | As-grown | | Irradiation at $\theta$ = 90° | | Irradiation at $\theta$ = 80° | |
|---|---|---|---|---|---|---|
| | $\varphi$ = 8° | $\varphi$ = 90° | $\varphi$ = 8° | $\varphi$ = 90° | $\varphi$ = 8° | $\varphi$ = 90° |
| $I_O/I_C$ | 0.07 | 0.03 | 0.05 | 0.07 | 0.15 | 0.11 |
| $I_O'/I_C$ | 0.09 | 0.08 | 0.13 | 0.14 | 0.13 | 0.12 |

## 4.5 Summary

We investigated the effects of ion irradiations on the reaction with oxidative radicals such as oxygen (O) atoms in $O_2$ plasma in the structures of CNWs. The reactive ion etchings (RIE) were carried out for CNWs using a dual-frequency capacitively-coupled $O_2$ or $O_2$/Ar plasma. The CNWs were selectively etched from the top edges with almost no etching on the wall surface. The etch rate was determined with both the density of O-related radicals and ions contributing to the RIE reaction. The top edges of the etched CNWs formed spear-like structures, which also strongly depended on the $O_2$ concentration. On the other hand, the O-related radicals and ions differently affected the crystalline structures of CNWs, which may induce chemically- and physically-disorders in the graphitic structures and leads to amorphization. As a result, it was suggested that ion irradiations during the RIE using $O_2$ or $O_2$/Ar plasmas can contribute to enhancements of etchings and amorphization in CNWs due to synergetic reactions of O-related radicals and ions.

We also demonstrated independently-controlled O atom and Ar ion irradiations to CNWs. While the Ar ion irradiation to the top edges of CNWs enhanced the etching reaction and amorphization similarly to the case of RIE, no spear was formed on the etched edge surface. The difference from the RIE indicated that formation of such spears by the RIE may occur due to higher ion energy and contributions of molecular species. The Ar ion irradiation to the wall surface of CNWs enhanced the oxidative etchings not only on the wall surface itself but also on the top edges due to formation of defects on the wall surface almost over the top to bottom. Consequently, control of ion-irradiated areas in CNWs with changing the ion incident angle opens the way for

selective oxidations of the top edges and wall surfaces with O-related radicals.

# References

[1] C. Berger, Z. Song, X. Li, X. Wu, Na. Brown, C. Naud, D. Mayou, T. Li, J. Hass, A. N. Marchenkov, E. H. Conrad, P. N. First, and W. A. de Heer: Science **312** (2006) 1191.

[2] M. Y. Han, B. Ozyilmaz, Y. B. Zhang, and P. Kim: Phys. Rev. Lett. **98** (2007) 206805.

[3] D. C. Kim, D.-Y. Jeon, H.-J. Chung, Y. S. Woo, J. K. Shin, and S. Seo: Nanotechnol. **20** (2009) 375703.

[4] K. Kim, H. J. Park, B.-C. Woo, K. J. Kim, G. T. Kim, and W. S. Yun: Nano Lett. **8** (2008) 3092.

[5] Y. J. Shin, Y. Y. Wang, H. Huang, G. Kalon, A. Thye, S. Wee, Z. Shen, C. S. Bhatia, and H. Yang: Langmuir **26** (2010) 3798.

[6] T. Gokus, R. R. Nair, A. Bonetti, M. Boehmler, A. Lombardo, K. S. Novoselov, A. K. Geim, A. C. Ferrari, and A. Hartschuh: ACS Nano **3** (2009) 3963.

[7] K.-J. Kim, J. Choi, H. Lee, M. C. Jung, H. J. Shin, T.-H. Kang, B. Kim, and S. Kim: J. Phys.: Condens. Matter. **22** (2010) 045005.

[8] N. Xiao, X. Dong, L. Song, D. Liu, Y. Y. Tay, S. Wu, L.-J. Li, Y. Zhao, T. Yu, H. Zhang, W. Huang, H. H. Hng, P. M. Ajayan, and Q. Yan: ACS Nano **5** (2011) 2749.

[9] A. Nourbakhsh, M. Cantoro, T. Vosch, G. Pourtois, F. Clemente, M. H. van der Veen1, J. Hofkens, M. M. Heyns, S. D. Gendt, and B. F. Sels: Nanotechnol. **23** (2010) 435203.

[10] A. C. Ferrari: Solid State Commun. **143** (2007) 47.

[11] I. Childres, L. A. Jauregui, J. Tian, and Y. P. Chen: New J. Phys. **13** (2011) 025008.

[12] O. Lehtinen, J. Kotakoski, A. V. Krasheninnikov, and J. Keinonen: Nanotechnol. **22** (2011) 175306.

[13] B. Guo, Q. Liu, E. Chen, H. Zhu, L. Fang, and J. R. Gong: Nano Lett. **10** (2010) 4975.

[14] S. Kondo, H. Kondo, Y. Miyawaki, H. Sasaki, H. Kano, M. Hiramatsu, and M. Hori: Jpn. J. Appl. Phys. **50** (2011) 075101.

# Chapter 5

# Modification of edges and planes of CNWs using radicals in hydrogen peroxide solution

## 5.1 Introduction

Liquid-phase oxidation using oxidative agents has been used for chemical and crystallographic modifications of graphene-based materials toward various purposes and applications. For example, carbon nanotubes (CNTs) has been oxidized with many liquid-phase oxidizing agents such as potassium permanganate ($KMnO_4$), nitric acid ($HNO_3$), a mixed liquid of $HNO_3$ and sulfuric acid ($H_2SO_4$), and hydrogen peroxide ($H_2O_2$) [1-7]. Oxidation of CNTs preferentially occurs at defected regions including graphene plane defects, edges, dangling bonds, and kink sites. In the oxidation process, oxidative functional groups such as carboxylic (-COOH), carbonyl (-C=O), and hydroxyl (-OH) groups are formed on the surface of nanotubes as well as graphene surface.

In particular, $H_2O_2$ which is a relatively mild oxidant show specific performances

for purification and modification of CNTs. It has been reported that $H_2O_2$ treatments can successfully remove impurities such as carbon impurities and catalyst metals in some types of CNTs [5,8,9]. In addition, $H_2O_2$ can selectively oxidize semiconducting single-wall CNTs (SWCNTs) and result in a higher than 80% concentration of metallic SWCNTs in the final product [6]. Furthermore, $H_2O_2$ can preferentially decompose thinner single-wall CNTs (SWCNTs) and be an effective agent for the diameter-selective purification of SWCNTs [10,11].

Such selective oxidations are attributed to specific reactions of oxidative radicals in the $H_2O_2$ solution and the structural features of CNTs such as curvature effects and existence of disordered parts on the rolled graphene surface. On the other hand, CNWs possess various structural fluctuations such as graphitic defects including the edges and domain boundaries and graphene nanostructures such as bends and branches, which are partially similar to defects based on a graphene lattice in CNTs but identifiable. Therefore, the oxidation of CNWs using oxidative radicals in $H_2O_2$ solution may result in selective modifications of the crystalline structures through preferential oxidative processes in graphitic defects on both the edges and planes. Moreover, the oxidation processes on a graphene edge and plane in $H_2O_2$ solution themselves have not been microscopically observed and identified yet.

In this chapter, we investigated the effects of oxidative radicals in $H_2O_2$ solution such as hydroxyl radical (·OH) on the surface morphologies of CNWs. Furthermore, the reaction mechanism was discussed comparing with morphological and chemical changes in a typical graphite surface by the same $H_2O_2$ treatment. We also demonstrated the atomic oxygen (O) treatments of $H_2O_2$-treated CNWs and graphite. The chemical properties of the $H_2O_2$-modified edges and planes for the reaction with O atoms were

investigated.

## 5.2 Experimental details

CNWs were fabricated on Si substrates using the RI-PECVD system as described in Subsection 2.1.1. The flow rates of $C_2F_6$ as carbon source gas and $H_2$ were 50 and 100 sccm at the total pressure of 133 Pa. The VHF and microwave powers were 220 and 300 W. The substrate temperature was about 630˚C. The deposition time was 45 min.

After the growth of the CNWs, the CNWs were treated with 30%-$H_2O_2$ solution for 12 hours at 90 ˚C. Then, the CNWs were heated in air at 110 ˚C on a hotplate to dry them. In addition, for comparison, an about 100-μm-thick graphite sample exfoliated from stacked graphite with a domain size of up to 1 μm was also treated with the $H_2O_2$ solution for 12 hours.

After the $H_2O_2$ treatments, the CNWs were also irradiated with O atoms using the radical source of the multi-beam plasma irradiation system as described in Subsection 2.1.2. The $O_2$ gas flow rate was 10 sccm and the total pressure in the chamber was 0.1 Pa. The RF powers applying to the radical source were 500 W. The substrate temperature was about 700˚C. The irradiation time was 5 to 10 min.

# 5.3 Effects of $H_2O_2$ treatments on graphitic structures of CNWs and graphite

## 5.3.1 Morphologies of $H_2O_2$-treated CNWs and graphite

Figures 5.1(a) and 5.1(b) show the cross-sectional SEM images of CNWs before and after the $H_2O_2$ treatment and insets show their overhead-view images. Each magnified view of the insets is shown in Figs. 5.1(c) and 5.1(d). Initial height of the CNWs before the $H_2O_2$ treatment was about 900 nm. As shown in Figs. 5.1(a) and 5.1(b), the height of CNWs hardly changed but slightly decreased to 850 nm after the $H_2O_2$ treatment. On the other hand, characteristic nanometer-scale asperities were formed on the side wall surface of the CNWs as shown in the inset of Fig. 5.1(b), while no change in the edge morphologies was observed. The average size of the dents was approximately 20 to 30 nm from Fig. 5.1(d). In the case of the atomic oxygen treatment, the CNWs are selectively etched from the top edges with almost no change in the wall surface morphology as shown in Chapter 3. This result indicates that the radicals in $H_2O_2$ solution such as ·OH react preferentially with the wall surface of CNWs and induce the characteristic changes in their morphology. However, considering the fact that, in general, graphene edges are much more chemically reactive than a six-membered ring plane, the radicals such as ·OH should react also with the top edges of CNWs and induce some structural changes. This will be discussed later from the aspect of chemical states.

To discuss about a formation process of nanometer-scale asperities on the wall

surfaces of CNWs, a graphite sample with a typical six-membered ring plane was also treated with the $H_2O_2$ solution. Figures 5.2(a) and 5.2(b) show AFM images of the graphite surfaces before and after the $H_2O_2$ treatment. As shown in Fig. 5.2(a), the pristine graphite surface was relatively smooth although there were some steps. After the treatment, some bumps with approximately 50 to 200 nm in width and 2 to 5 nm in height were found at approximately 100 to 200 intervals (Fig. 5.2(b)). As a result, the surface roughness of the graphite critically increased after the $H_2O_2$ treatment due to formation of characteristic asperities, which is similar to the morphological change occurred on the wall surface of CNWs. The results indicate that the radicals such as ·OH may preferentially react with a region of specific crystalline structures on a graphene plane such as graphitic defects and distortions.

In the case of CNTs, $H_2O_2$ can preferentially decompose thinner single-wall CNTs (SWCNTs) and be an effective agent for the diameter-selective purification of SWCNTs [10,11]. The selectivity for oxidation of CNTs is caused by curvature effects, which means a kind of stress regions on a graphene plane or resulting defects and distortions may be reactive to the oxidative radicals in $H_2O_2$ solution. According to these facts, the radicals may also preferentially react with the domain boundaries on the wall surface of CNWs and graphite surface with some stresses and defects.

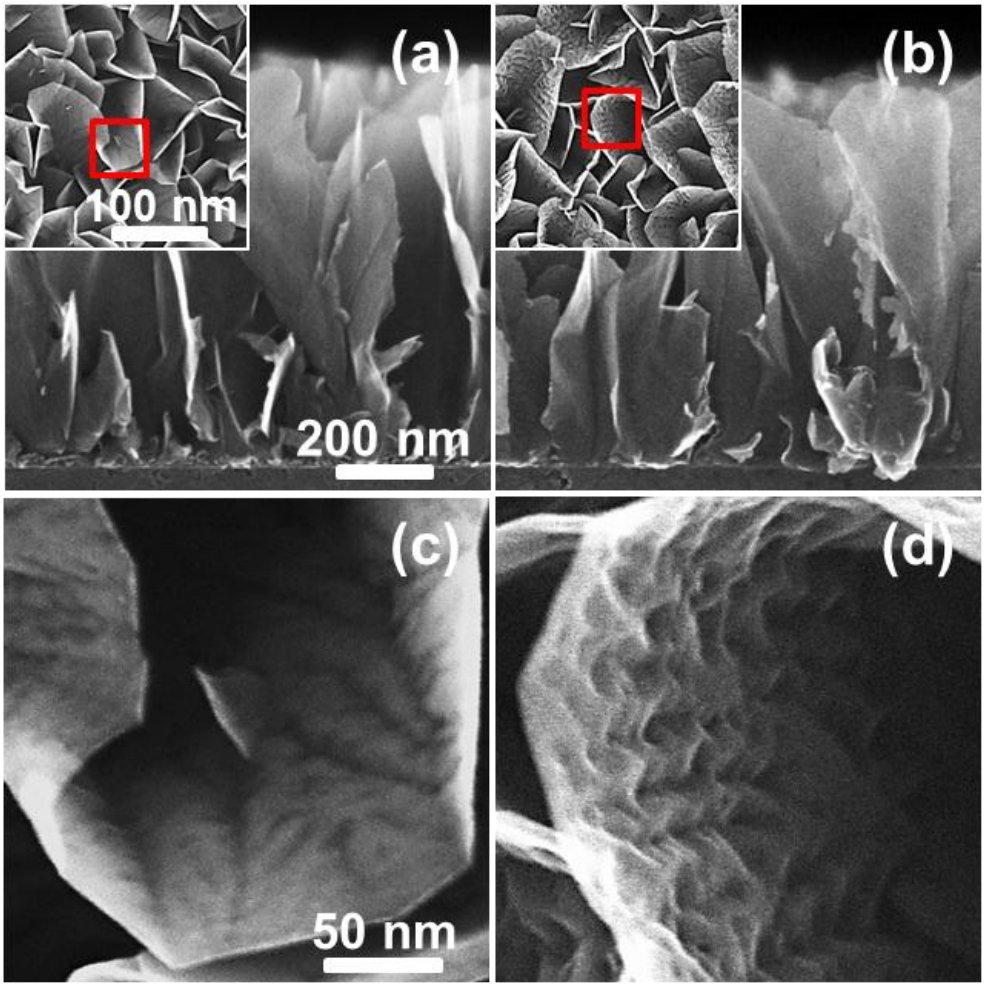


Fig. 5.1. Cross-sectional SEM images of the CNWs (a) before and (b) after the $H_2O_2$ treatment in which insets show each overhead view. (c), (d) Magnified views of the areas pointed by red squares in the insets.

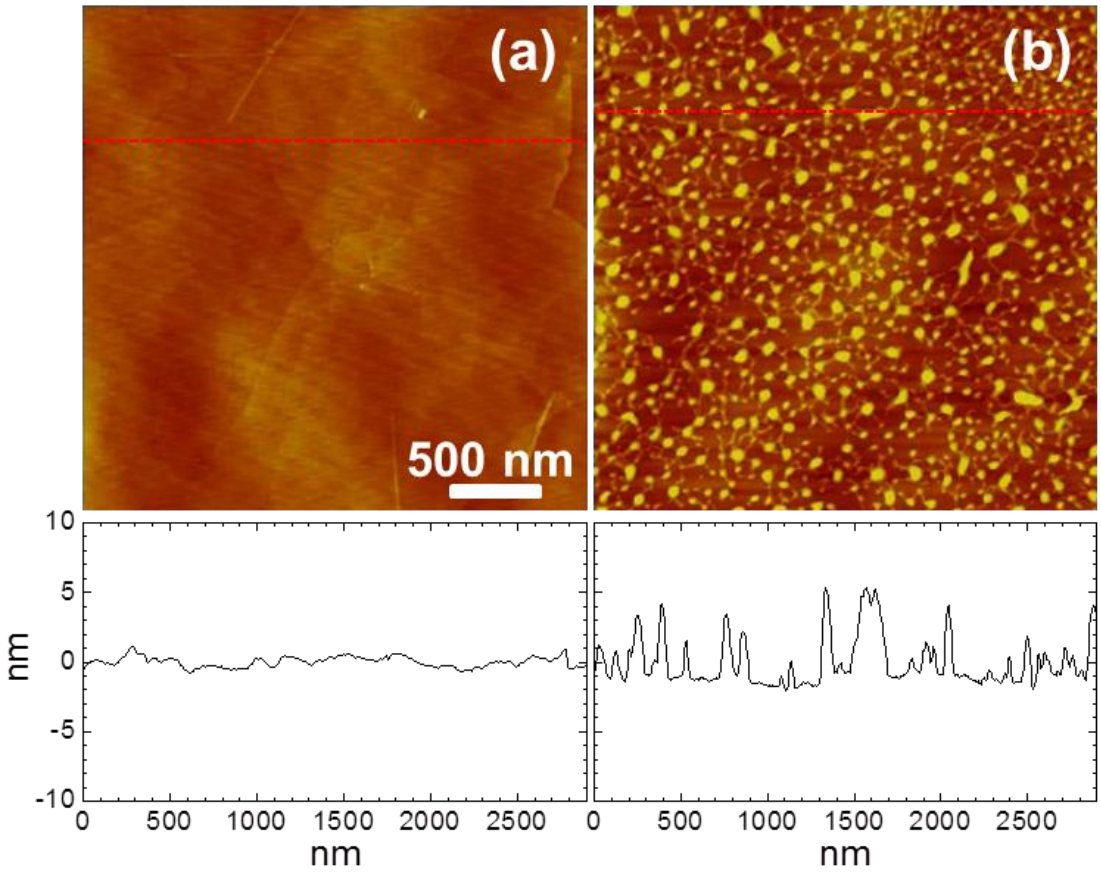


Fig. 5.2. AFM images of the surface of the graphite (a) before and (b) after $H_2O_2$ treatment with each line profile of cross sections pointed by red dash lines.

### 5.3.2 Raman spectroscopic analyses of $H_2O_2$-treated CNWs and graphite

Raman spectra of the CNWs and graphite were measured to evaluate their crystalline structures. Figure 5.3 shows Raman spectra of the CNWs and graphite before and after the $H_2O_2$ treatment. Each Raman spectrum was normalized by a peak intensity of G-band. As shown in Fig. 5.3(a), the relatively strong and sharp D-band and D'-band in the Raman spectra of CNWs are attributed to the boundaries between nanographite domains as well as the high density of top edges [12,13]. The intensity of D-band peak slightly decreased after the treatment. This small difference may be attributed to an inactivation of graphitic defects caused by chemical modifications such as hydroxyl adsorptions.

Furthermore, the domain size was also evaluated using eq. (2.2). The domain sizes of the as-grown and treated CNWs were calculated to be 11.5 and 12.7 nm, respectively. Although there were effects of the top edges of CNWs in this estimation, if such the effect of the top edges could be eliminated, an increase in the estimated value is less than twice [12]. The $L_a$ values are almost equal to the average size of the dents observed in Fig. 5.1(d). This result suggests that the morphological changes on the wall surfaces of CNWs by the $H_2O_2$ treatment depend on the domain size. On the other hand, no D-band peak was found for the pristine graphite and only a slight peak was found after the $H_2O_2$ treatment. This means that the graphite used in this study has nearly single-crystalline structure according to the Raman spectra, and the defects were formed only on the surface after the $H_2O_2$ treatment. It is deduced that the defects exist mainly on the surface of graphite. Therefore, this kind of grain size estimation does not

necessarily correspond to their surface conditions.

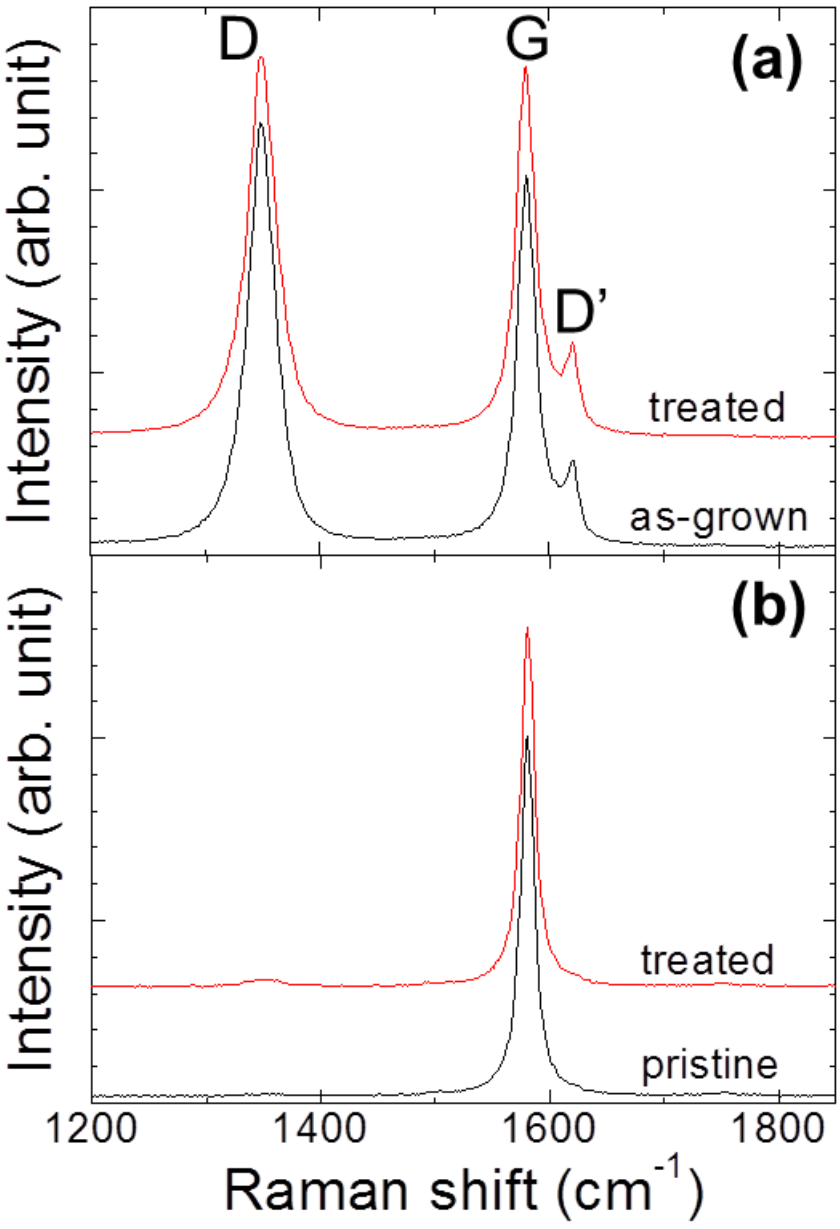


Fig. 5.3. Raman spectra of (a) the CNWs and (b) the graphite before and after the $H_2O_2$ treatment.

### 5.3.3 Surface chemical states of $H_2O_2$-treated CNWs and graphite

To identify surface chemical changes such as adsorptions of oxidizing species in the CNWs and graphite, an XPS analysis was carried out at a take-off angle of photoelectrons, $\varphi$, of 8˚. The photoelectron spectra at $\varphi$ = 8˚ include specific information focusing on the top edges of CNWs and the several layers on the graphite surface. Figure 5.4 shows the C 1s and O 1s photoelectron spectra at $\varphi$ = 8˚ for the CNWs and graphite before and after the $H_2O_2$ treatments. The O 1s peaks were expressed as the peak area ratios of O 1s to C 1s. Table 5.1 shows the integrated peak intensity ratio of O 1s to C1s, $I_O/I_C$, calculated using the photoionization cross sections of each element. In addition, the integrated peak intensity ratio of a sum of oxide peaks caused by C-OH or C-O-C, C=O, and O=C-OH in a C ls peak to the total C 1s peak, $I_O'/I_C$, was also calculated as shown in Table 5.1.

In the case of the CNWs, the C-OH and C-O-C components increased after the $H_2O_2$ treatment and its portion of the C ls peak area increased from 0.19 to 0.25. At that time, $I_O/I_C$ ratio at $\varphi$ = 8˚ increased from 0.10 to 0.33 after the $H_2O_2$ treatment. On the other hand, it was also confirmed that the $I_O/I_C$ ratio at $\varphi$ = 90˚ was 0.07 before the treatment and increased to 0.15 after the treatment. $I_O'/I_C$ ratios at $\varphi$ = 8, 90˚ showed the same tendency to increase after the treatment as the $I_O/I_C$ ratio. However, it should be noted that the photoelectron spectra at $\varphi$ = 90˚ also include the information of the top edges. Therefore, these results mean that the radicals such as ·OH adsorbed mainly on the top edges due to higher-density dangling bonds.

In the case of the graphite, not only the C-OH and C-O-C components but also C=O one decreased after the treatment. The $I_O/I_C$ ratio at $\varphi$ = 8˚ slightly decreased from

0.10 to 0.07, while that at $\varphi$ = 90˚ slightly increased from 0.01 to 0.03. The same tendencies were observed for the $I_O'/I_C$ ratios in the C 1s peak. These phenomena mean that while oxidative chemisorption on a few layers of graphene within a depth of about 1 nm from the surface slightly decreased, that on graphene sheets within a depth of 1 to about 10 nm from the surface increased. The much lower $I_O/I_C$ and $I_O'/I_C$ ratios at $\varphi$ = 90˚ indicates that the detected oxygen-related components exist only at the step edges on the graphite surface. Furthermore, slight decreases of $I_O/I_C$ and $I_O'/I_C$ ratios at $\varphi$ = 8˚ suggest hydroxyl adsorption around the characteristic asperities formed after the $H_2O_2$ treatment is lower than that at other regions. In contrast, slight increases of $I_O/I_C$ and $I_O'/I_C$ ratios indicate burrowing of oxidative species into the underlying layers, which may induce the asperities due to local reduction of the interaction energy between the graphene layers.

According to these XPS results, it is suggested that oxygen components on the plane surface of the CNWs also decreased after the $H_2O_2$ treatment as well as the graphite surface while those on the underlying graphene sheets may increase due to burrowing. These results indicate that the radicals such as ·OH preferentially react with the top edges of CNWs and form hydroxyl or ether functional groups. Although such the radicals also should react with defected and distorted regions on a graphene plane such as the domain boundaries in the CNWs, they don't form stable functional groups. Such the radicals burrow into the underlying graphene sheets or desorbed through some etching reactions, which can results in formation of the characteristic asperities on the plane surface. For the different etching reaction from that in the case of the etching from the top edges by O atoms, it has been reported that amorphous carbon components around the CNT can be selectively etched by the $H_2O_2$ treatment [8,9]. However, the

detailed mechanism of formation of the characteristic asperities is not clear yet, and need the further investigation. As a result, we have demonstrated a selective morphological modification of wall surfaces of the CNWs by the $H_2O_2$ treatment.

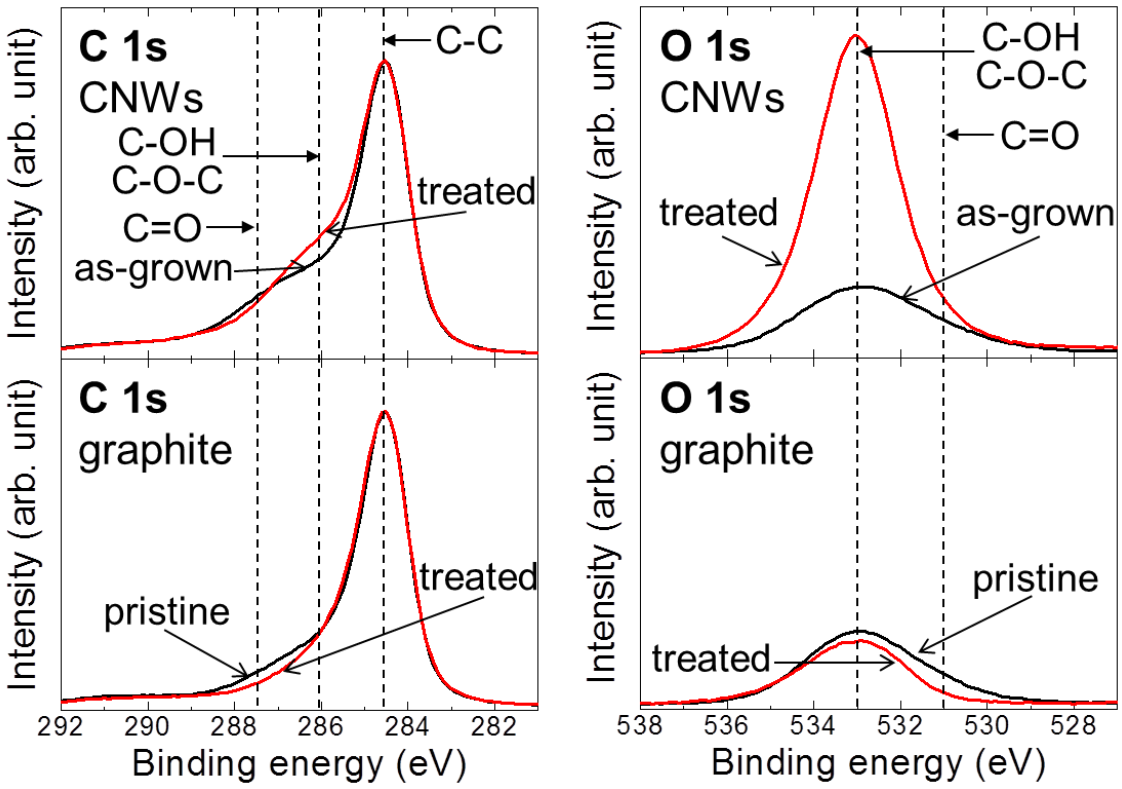


Fig. 5.4. C ls and O 1s photoelectron spectra at a take-off angle of 8˚ for the CNWs and the graphite before and after $H_2O_2$ treatment.

Table 5.1. Integrated peak intensity ratio of O 1s to C1s, $I_O/I_C$, and that of a sum of oxide peaks in each C 1s peak to the total C 1s, $I_O'/I_C$, for the CNWs and graphite before and after $H_2O_2$ treatments.

| | CNWs | | | | graphite | | | |
|---|---|---|---|---|---|---|---|---|
| | as-grown | | $H_2O_2$-treated | | pristine | | $H_2O_2$-treated | |
| | $\varphi$ = 8˚ | $\varphi$ = 90˚ | $\varphi$ = 8˚ | $\varphi$ = 90˚ | $\varphi$ = 8˚ | $\varphi$ = 90˚ | $\varphi$ = 8˚ | $\varphi$ = 90˚ |
| $I_O/I_C$ | 0.10 | 0.07 | 0.33 | 0.15 | 0.10 | 0.01 | 0.07 | 0.03 |
| $I_O'/I_C$ | 0.33 | 0.15 | 0.36 | 0.22 | 0.24 | 0.09 | 0.17 | 0.12 |

# 5.4 Effects of reaction with O atoms on $H_2O_2$-treated graphitic structures

## 5.4.1 Changes in surface morphologies of $H_2O_2$-treated CNWs and graphite by reaction with O atoms

Figures 5.5(a) and 5.5(b) show the cross-sectional SEM images of CNWs after the $H_2O_2$ treatment and after the following atomic oxygen (post-O) treatment and insets show their overhead-view images. Each magnified view of the insets is shown in Fig. 5.5(c) and 5.5(d). The height of CNWs slightly decreased from 850 to 800 nm after the post-O treatment as shown in Fig. 5.5(a) and 5.5(b). The edge morphologies significantly changed to be rougher and characteristic sharp edges which seem to have a kind of patterns depending on the nanometer-scale asperities formed on the wall surface around the top edges after the $H_2O_2$ treatment. On the other hand, the wall surfaces roughened by the nanometer-scale asperities in the $H_2O_2$-treated CNWs were smoother after the post-O treatment than before as shown in Fig. 5.5(d). These results indicate that the bumped parts in the asperities on the wall surface are preferentially etched by O atoms, which may also induce bi-directional etchings from both the top edges and side wall around the top edges and form the characteristic sharp edges.

We also exposed the graphite treated with $H_2O_2$ to O atoms to discuss about the morphological changes in the edge and wall surfaces of $H_2O_2$-treated CNWs. Figures 5.6(a) and 5.6(b) show AFM images of the graphite surfaces after the $H_2O_2$ treatment and after the post-O treatment. As shown in Fig. 5.6(b), the average width and height of

the bumps formed after the $H_2O_2$ treatment decreased to less than 50 nm and less than 3 nm as shown in Fig. 5.6(b). As a result, the surface roughness of the $H_2O_2$-treated graphite drastically decreased after the post-O treatment due to etchings of characteristic asperities, which is similar to the morphological change occurred on the wall surface of CNWs. It has been found that O atoms preferentially etch the top edges of CNWs in Chapter 3. On the other hand, the radicals in $H_2O_2$ solution such as ·OH hardly chemisorb on a graphene plane as shown in Subsection 4.3.3. These results suggest that the bumps formed on the graphene surfaces by $H_2O_2$ treatments may contain a relatively-high density of edges and other defects rather than chemically-induced reactive sites, which leads to selective etchings of the nanometer-scale asperities and planarization of the $H_2O_2$-treated graphene planes.

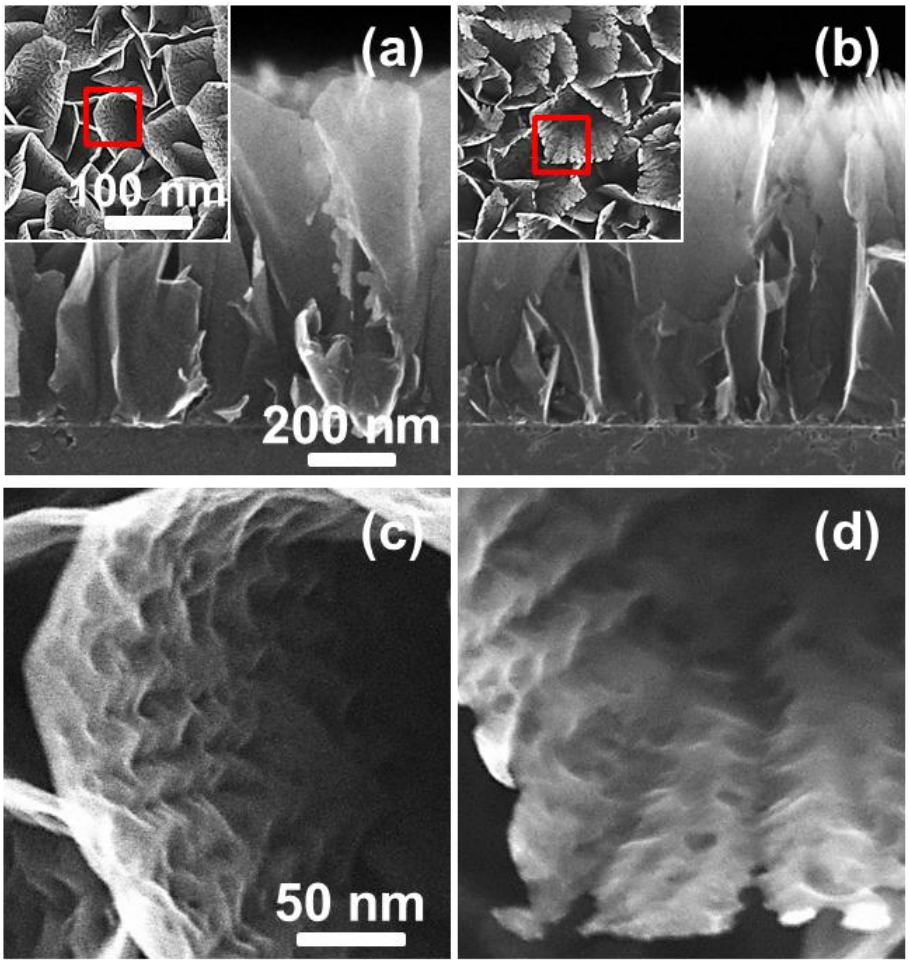


Fig. 5.5. Cross-sectional SEM images of the CNWs (a) after the $H_2O_2$ treatment and (b) after the following atomic oxygen treatment in which insets show each overhead view. (c), (d) Magnified views of the areas pointed by red squares in the insets.

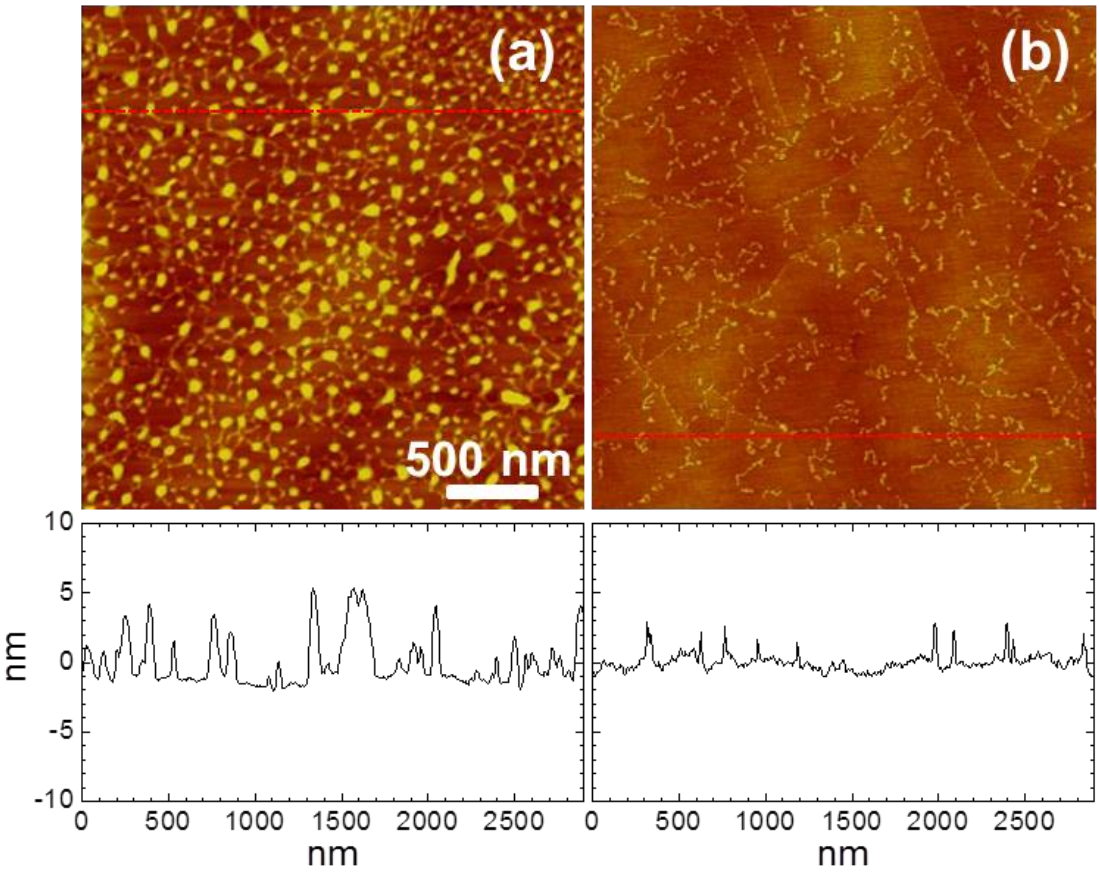


Fig. 5.6. AFM images of the surface of the graphite (a) after the $H_2O_2$ treatment and (b) after the following atomic oxygen treatment with each line profile of cross sections pointed by red dash lines.

### 5.4.2 Surface chemical changes in $H_2O_2$-treated CNWs and graphite by reaction with O atoms

XPS analyses were also carried out at a take-off angle of photoelectrons, $\varphi$, of 8˚. Figure 5.7 shows the C 1s and O 1s photoelectron spectra at $\varphi$ = 8˚ for the CNWs and graphite before and after the $H_2O_2$ treatments and post-O treatments. The O 1s peaks were normalized with the peak areas of C 1s. Similarly to Subsection 5.3.3, the integrated peak intensity ratio of O 1s to C1s, $I_O/I_C$, and the integrated peak intensity ratio of a sum of oxide peaks in each C ls peak to the total C 1s peak, $I_O'/I_C$, were calculated as shown in Table 5.2.

In the case of the CNWs, the C-OH or C-O-C components further increased after the post-O treatment and its portion of the C ls peak area increased from 0.25 to 0.32. At that time, $I_O/I_C$ ratio at $\varphi$ = 8˚ increased from 0.33 to 0.37 after the post-O treatment. Additionally, the $I_O/I_C$ ratio at $\varphi$ = 90˚ was also confirmed to further increase from 0.15 to 0.18 by the post-O treatment, which absolutely also includes the information of the top edges. On the other hand, while $I_O'/I_C$ ratio at $\varphi$ = 8˚ increased from 0.36 to 0.41 after the post-O treatment, that at $\varphi$ = 90˚ slightly decreased to 0.20. This inconsistency between $I_O/I_C$ and $I_O'/I_C$ ratios indicates that the amount of C-C bonds on the wall surfaces of CNWs may decrease through etchings of the bumps on the corrugated surfaces. Therefore, the $H_2O_2$-chemisorbed top edges of CNWs can enhance further formation of oxidative functional groups through the reaction with O atoms and air exposure after the treatment. Such chemisorption has never been observed in the CNWs after the O treatment with heating as shown in Subsection 3.3.3.

In the case of the graphite, the C-OH or C-O-C and C=O components increased after the post-O treatment, despite the tendency to decrease after the $H_2O_2$ treatment. The $I_O/I_C$ ratio at $\varphi = 8^\circ$ clearly increased from 0.07 to 0.16 after the post-O treatment, while that at $\varphi = 90^\circ$ hardly changed and remained to be 0.03. The same tendencies were observed for the $I_O'/I_C$ ratios in the C 1s peak. The increases in the $I_O/I_C$ and $I_O'/I_C$ ratios at $\varphi = 8^\circ$ show that the bumps being etched by O atoms on the $H_2O_2$-treated graphite surface may contain a relatively-high density of edges and other defects which can be easily oxidized by O atoms during the post-O treatment and air exposure after the treatment. Furthermore, almost no change in the $I_O/I_C$ and $I_O'/I_C$ ratios at $\varphi = 90^\circ$ including the information of those at $\varphi = 8^\circ$ suggests that oxygen components might be mainly in the underlying region on the bumped area and those can reduce due to the preferential etching of the bumps.

According to these XPS results, it is indicated that O atoms preferentially react with not only the top edges but also the bumps induced by the $H_2O_2$ treatment on the graphene planes in CNWs and graphite. These reactions with O atoms in the $H_2O_2$-modified graphitic structures can induce etchings from both the edges and planes and enhance the oxidation of the entire graphitic structures.

The nanometer-scale asperities on the wall surface of CNWs can be utilized as more stable anchors for supported metal nanoparticles in fuel cells and organopollutant degradation devices [14,15]. The rougher surfaces may also increase the effective surface area for such nanoparticles. Furthermore, control of defects on the graphene planes may contribute to develop the electronic and magnetic properties [16]. In addition, such the asperities can be reduced by O atom exposure after the $H_2O_2$ treatment. This result suggests a possibility to realize side wall etching and thickness

control of walls in the CNWs, which is essential to control electrical properties of graphene materials and realize their applications to electrical devices. The subsequent atomic oxygen treatment after the $H_2O_2$ treatment can also enhance the chemical reactivity of graphitic structures to oxidation. This study will open a new avenue towards highly-selective morphological and chemical modifications of the plane surface of CNWs for realizing green energy devices, biosensors, and electronic devices.

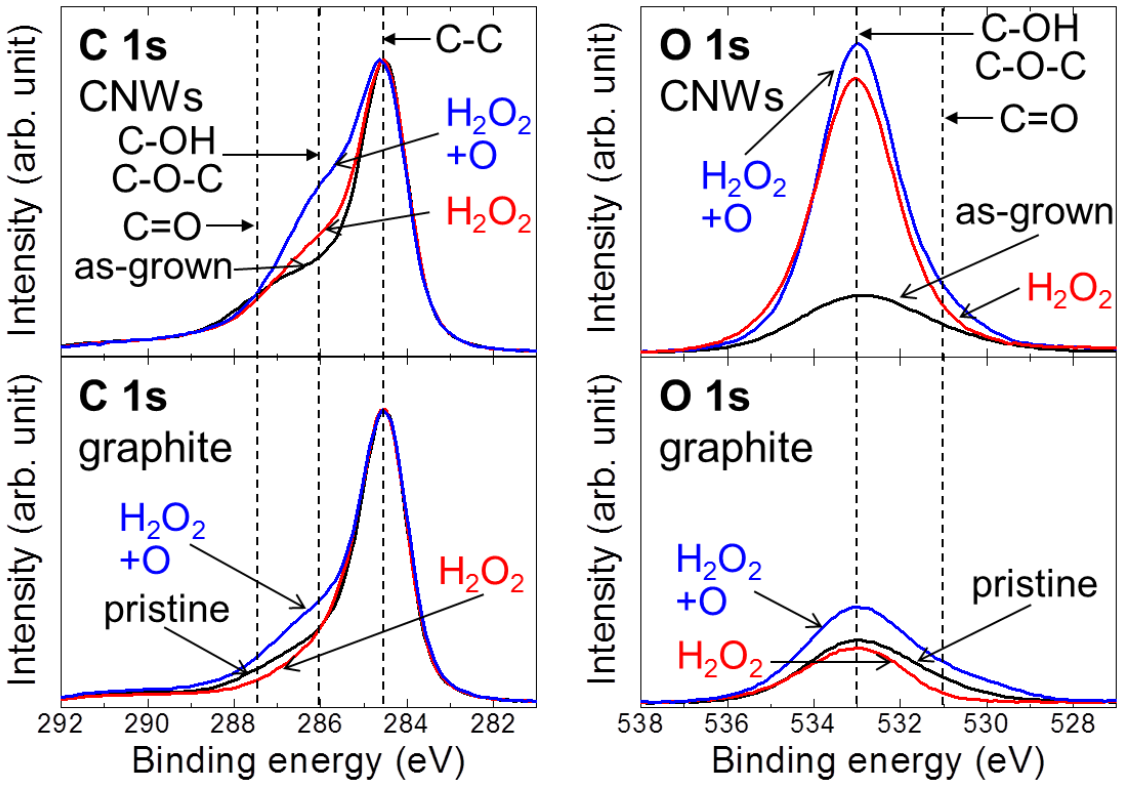


Fig. 5.7. C ls and O 1s photoelectron spectra at a take-off angle of 8˚ for the CNWs and the graphite before and after $H_2O_2$ treatment and post-O treatment.

Table 5.2. Integrated peak intensity ratio of O 1s to C1s, $I_O/I_C$, and that of a sum of oxide peaks in each C 1s peak to the total C 1s, $I_O'/I_C$, for the CNWs and graphite before and after post-O treatments.

| | CNWs | | | | graphite | | | |
|---|---|---|---|---|---|---|---|---|
| | $H_2O_2$-treated | | post-O-treated | | $H_2O_2$-treated | | post-O-treated | |
| | $\varphi$ = 8˚ | $\varphi$ = 90˚ | $\varphi$ = 8˚ | $\varphi$ = 90˚ | $\varphi$ = 8˚ | $\varphi$ = 90˚ | $\varphi$ = 8˚ | $\varphi$ = 90˚ |
| $I_O/I_C$ | 0.33 | 0.15 | 0.37 | 0.18 | 0.07 | 0.03 | 0.16 | 0.03 |
| $I_O'/I_C$ | 0.36 | 0.22 | 0.41 | 0.20 | 0.17 | 0.12 | 0.32 | 0.11 |

## 5.5 Summary

We investigated the effects of reaction with radicals in $H_2O_2$ solution such as ·OH on graphitic structures of CNWs and graphite. We have developed the selective modification technique for controlling the wall surface morphology including domain boundaries of CNWs employing the $H_2O_2$ solution. Oxidative radicals in the $H_2O_2$ solution induced characteristic nanometer-scale asperities on the wall surfaces of CNWs without etchings from the top edges. This type of characteristic asperities was also observed on a typical graphite surface after the $H_2O_2$ treatment. The domain sizes in the CNWs evaluated using the Raman spectra were almost equal to the size of the dents observed in the SEM image of the treated CNWs. The XPS analysis indicated that hydroxyl or ether functional groups were formed mainly on the top edges of CNWs after the $H_2O_2$ treatment, while oxygen components on the plane surface decreased. Consequently, it was found that the radicals such as ·OH selectively oxidized the top edges of CNWs and modified the surface morphologies on the wall surface without etchings from the top edges.

The surface roughness of the $H_2O_2$-treated wall surface of CNWs and graphite surface drastically decreased after the post-O treatment due to etchings of characteristic asperities. It was suggested that the bumps formed on the graphene surfaces by $H_2O_2$ treatments may contain a relatively-high density of edges and other defects rather than chemically-induced reactive sites. It was found that the reaction with O atoms in the $H_2O_2$-modified graphitic structures can induce etchings from both the edges and planes and enhance the oxidation of the graphitic structures.

# References

[1] N. Zhang, J. Xie , and V. KVaradan: Smart Mater. Struct. **11** (2002) 962.

[2] X. Zhang, T. V. Sreekumar, T. Liu, and S. Kumar: J. Phys. Chem. B **108** (2004) 16435.

[3] I. D. Rosca, F. Watari, M. Uo, and T. Akasaka: Carbon **43** (2005) 3124.

[4] H. Kong, C. Gao, and D. Yan: J. Am. Chem. Soc. **126** (2004) 412.

[5] Y. Wang, X. D. Bai, and J. Liang: New Carbon Mater. **20** (2005) 103.

[6] Y. Miyata, Y. Maniwa, and H. Kataura: J. Phys. Chem. B **110** (2006) 25.

[7] K. Hernadi, A. Siska, L. Thien-Nga, L. Forro, and I. Kiricsi: Solid State Ionics **141-142** (2001) 203.

[8] Y. Feng, G. Zhou, G. Wang, M. Qu, and Z. Yu: Chem. Phys. Lett. **375** (2003) 645.

[9] Y. Feng, H. Zhang, Y. Hou, T. P. McNicholas, D. Yuan, S. Yang, L. Ding, W. Feng, and J. Liu: ACS Nano **2** (2008) 1634.

[10] F. Simon, Á. Kukovecz, and H. Kuzmany: AIP Conf. Proc. **685** (2003) 185.

[11] M. Yudasaka, M. Zhang, and S. Iijima: Chem. Phys. Lett. **374** (2003) 132.

[12] S. Kurita, A. Yoshimura, H. Kawamoto, T. Uchida, K. Kojima, M. Tachibana, P. Molina-Morales, and H. Nakai: J. Appl. Phys. **97** (2005) 104320.

[13] Z. H. Ni, H. M. Fan, Y. P. Feng, Z. X. Shen, B. J. Yang, and Y. H. Wu: J. Chem. Phys. **124** (2006) 204703.

[14] K. Mase, H. Kondo, S. Kondo, M. Hori, M. Hiramatsu, and H. Kano: Appl. Phys. Lett. **98** (2011) 193108.

[15] T. Horibe, H. Kondo, K. Ishikawa, H. Kano, M. Sekine, M. Hiramatsu, and M. Hori: Appl. Phys. Express **6** (2013) 045103.

[16] F. Banhart, J. Kotakoski, and A. V. Krasheninnikov: ACS Nano **8** (2011) 26.

# Chapter 6

# Conclusions

## 6.1 Summary of this thesis

In this thesis, the oxidation processes in CNWs under some different oxidative conditions were investigated to precisely control the graphitic structures including edges and various defects. The reactions with oxygen (O) atoms, ions, and molecular radicals such as hydroxyl radicals (·OH) including their synergies and combinations in the graphitic structures were clarified. The selectivity of the oxidation of the edges and wall surfaces in CNWs was discussed by focusing on each morphological and chemical change, which leads to establish highly-selective modifications of graphene edges and plane. The summary of each chapter is briefly described as follows.

In Chapter 1, as an introduction of this thesis, carbon nanowalls (CNWs) were explained with respect to fundamental characteristics, growth controls, and treatments. Graphitic defects and oxidative processes for controlling them were described for the motivation. Then, the purpose and overview of this thesis were also described.

In Chapter 2, two main plasma processing systems were described, in which one

was for synthesis of CNWs and the other was for post-growth treatment of them. CNWs were synthesized using the RI-PECVD system. The CNWs were treated using multi-beam plasma irradiation system which consisted of two remote plasma sources. Various evaluation methods of the treated CNWs were also described. The principles of the evaluation methods and analyses techniques such as scanning electron microscopy (SEM), Raman spectroscopy, X-ray photoelectron spectroscopy (XPS), X-ray diffraction (XRD), and atomic force microscope were explained.

In Chapter 3, the effects of oxidative reactions with atomic oxygen (O) on the structures of CNWs were investigated. The CNWs were selectively etched from the top edges with almost no etching on the wall surface by the reaction with O atoms. The preferential reactions with O atoms induced a kind of amorphization through oxidative chemisorption and etchings mainly on the top edges, but its influences on the total crystallinity were small. Activation energy and reaction probability for the reaction with O atoms were also estimated for the etching from the top edges. As a result, it was found that the etching reaction with O atoms proceeded with almost no barrier and preferentially and effectively removed the carbon atoms on the top edges of CNWs. Through the investigation of the influences of the crystallinities of CNWs on the oxidative reaction with O atoms, it was found that the lower crystallinities of graphene sheets and lower-crystallized layered structure enhanced the etching reaction from the top edges of CNWs and chemisorption with O atoms and caused the rougher and amorphous surface morphologies. However, there was almost no morphological change in the wall surfaces, which means such crystallinities hardly affect the selectivity of the reaction with O atoms in CNWs.

In Chapter 4, the effects of ion irradiations on the reaction with oxidative radicals

such as oxygen (O) atoms in $O_2$ plasma in the structures of CNWs were investigated. The CNWs were selectively etched from the top edges with almost no etching on the wall surface by the reactive ion etchings (RIE) using $O_2$ or $O_2$/Ar plasma. Both the density of O-related radicals and ions contributing to the RIE reaction affected the etching from the top edges, which also induced spear-like structures strongly depended on the $O_2$ concentration. On the other hand, the O-related radicals and ions differently affected the crystalline structures of CNWs, which may induce chemically- and physically-disorders in the graphitic structures and leads to amorphization. Synergetic reactions of O-related radicals and ions during the RIE enhanced etchings and amorphization in CNWs. We also demonstrated independently-controlled O atom and Ar ion irradiations to CNWs. While the Ar ion irradiation to the top edges of CNWs enhanced the etching reaction and amorphization similarly to the case of RIE, no spear was formed on the etched edge surface due to lower ion energy and absence of molecular species. Furthermore, the Ar ion irradiation to the wall surface of CNWs enhanced the oxidative etchings not only on the wall surface itself but also on the top edges due to formation of defects on the whole surface. Such control of ion-irradiated areas in CNWs with changing the ion incident angle opens the way for selective oxidations of the top edges and wall surfaces with O-related radicals.

In Chapter 5, the effects of reaction with radicals in $H_2O_2$ solution such as ·OH on surface morphologies and chemistry of graphitic structures in CNWs and graphite were investigated. The selective modification technique for controlling the wall surface morphology including domain boundaries of CNWs was developed. Oxidative radicals in the $H_2O_2$ solution induced characteristic nanometer-scale asperities on the wall surfaces of CNWs without etchings from the top edges. This type of characteristic

asperities was also observed on a typical graphite surface after the $H_2O_2$ treatment. The domain sizes in the CNWs evaluated using the Raman spectra were almost equal to the size of the dents observed in the SEM image of the treated CNWs. Hydroxyl or ether functional groups were formed mainly on the top edges of CNWs after the $H_2O_2$ treatment, while oxygen components on the plane surface decreased. Consequently, it was found that the radicals such as ·OH selectively oxidized the top edges of CNWs and modified the surface morphologies on the wall surface without etchings from the top edges. In addition, such the asperities were reduced by O atom exposure after the $H_2O_2$ treatment, which suggested a possibility to realize side wall etching and thickness control of walls in the CNWs. The subsequent atomic oxygen treatment after the $H_2O_2$ treatment also enhanced the chemical reactivity of graphitic structures to oxidation. This study will open a new avenue towards highly-selective morphological and chemical modifications of the plane surface of CNWs for realizing green energy devices, biosensors, and electronic devices.

## 6.2 Scopes for future works

Oxygen atom exposure using remote $O_2$ plasmas has been carried out at various pressures. Theoretically, it has been found that oxidative processes for chemisorption and formation of defects on a graphene plane by O atoms strongly depend on the amount of O atoms contributing to the reaction. In an experimental case, the flux of O atoms reaching the graphene plane is one of important factors in control of the oxidative

processes in graphitic materials such as CNWs. In this thesis, we have performed O atom exposures in combination with the measurement of the absolute density of O atoms and estimation of the flux using VUVAS. Such combination of evaluating materials and gas-phase diagnostics enables us to precisely control the amount of O atoms and more systematically study on the oxidative processes on graphitic structures. Furthermore, we have demonstrated independently-controlled radical and ion irradiation techniques using the multi-beam plasma irradiation system. Ion irradiations play important roles of formation of defects and enhancements of the oxidative reaction. In comparison with the RIE using $O_2$ plasma, it has been indicated that the ion energy may be one of critical factors in modification of the edge morphologies of CNWs, which reconfirms that effects of ion irradiation on the graphitic structures can depend on the ion energy. Therefore, control of the ion energy as well as the ion incident angle as shown in our specific system is necessary to understand and control the effects on the graphitic structures. Accordingly, detailed studies on O atom and ion irradiation to CNWs and other graphene materials with controlling fluxes, ion incident angle, and ion energy will experimentally clarify the mechanism of oxidative processes and precisely and selectively modify the crystallographic structures.

This thesis has also shown that the radicals in $H_2O_2$ solution such as ·OH can selectively modify the wall surface morphology and edge chemistry in CNWs. Furthermore, the following O atom exposure can achieve further chemisorbed edges and planes and side-wall etching leading to reduce the thickness of wall. Therefore, cycling treatments using $H_2O_2$ and O atoms are promising oxidation techniques to control the oxidation and the number of graphene sheets in CNWs, which even lead to synthesis of some kinds of graphene-oxide nanostructures and vertically-aligned nanographenes.

Oxidized graphitic structures and reduced thickness of wall in CNWs can modify the electronic properties, for example, opening their energy band gap and develop the magnetic properties. The successfully-modified electronic band structures or magnetic moments and structural features of CNWs such as large surface area will develop the future nanoelectronics, optoelectronic devices such as solar cells, magnetic devices, and biological or medical applications such as biosensors. To realize the precise modifications and these applications, the effect of each radical in $H_2O_2$ solution has to be identified and precisely controlled. For instance, an irradiation with ·OH to CNWs can be carried out by $H_2O$ plasma.

# Acknowledgements

The present research was performed in Professor Hori and Professor Sekine Laboratory, Department of Electrical Engineering and Computer Science, Nagoya University. Author would like to appreciate his research advisor, Professor Masaru Hori, Department of Electrical Engineering and Computer Science, Nagoya University, for his guidance, advices, and encouragements through the course of this research. The author also would like to thank his vice-advisors, Professor Makoto Sekine, Plasma Nanotechnology Research Center, Nagoya University, and associate Professor Hiroki Kondo, Department of Electrical Engineering and Computer Science, Nagoya University, for lots of valuable comments. The author also would like to thank his vice-advisers, Professor Seiichi Miyazaki, Department of Quantum Engineering, Nagoya University, and Professor Noritsugu Umehara, Department of Mechanical Science and Engineering, Nagoya University, for their guidance and valuable suggestions in preparing this thesis.

At the same time, the author would like to thank Professor Hirotaka Toyoda, Department of Electrical Engineering and Computer Science, Nagoya University, for his hearty management in International Training Program.

The author is enormous grateful to Professor Mineo Hiramatsu, Department of Electrical and Electronic Engineering, Meijo University, Professor Masafumi Ito, Department of Electrical and Electronic Engineering, Meijo University, Professor Kenji Ishikawa, Plasma Nanotechnology Research Center, Nagoya University, Assistant Professor Keigo Takeda, Department of Electrical Engineering and Computer Science, Nagoya University, and associate Professor Satomi Tajima, Plasma Nanotechnology Research Center, Nagoya University, for their valuable comments and suggestions. The author would like to appreciate his corroborating researchers, Drs. Wakana Takeuchi and Shingo Kondo for their uncountable superior advices and specific suggestions in the author’s research. The author would like to acknowledge Dr. Koji Yamakawa at Katagiri Engineering Co., Ltd. for their helpful advices and discussions.

The author appreciates Prof. Matthew Goeckner, Prof. Lawrence J. Overzet, Dr. Cristina Estrada, Dr. Daisuke Ogawa, and all other members in Plasma Applications Laboratory, University of Texas at Dallas, United States, for giving me the opportunity to study in the group.

The author also thanks sincerely Dr. Yusuke Abe, Dr. Hitoshi Watanabe, Mr. Hyung

Jun Cho, and Mr. Lingyun Jia who aided his experimental works carried out in this study and also expressed their valuable suggestions and discussions. He also thanks Dr. Chang Sung Moon, Dr. Hirotoshi Inui, Dr. Tsuyoshi Yamaguchi, Dr. Arkadiusz Malinowski, Dr. Hiroshi Yamamoto, Dr. Shang Chen, Dr. Takuya Takeuchi, Dr. Yudai Miyawaki, Dr. Takayuki Hiraoka, Mr. Toshiya Suzuki, Mr. Lu Yi, Mr. Jong Yun Park, Mr. Takayoshi Tsutsumi, Mr. Yusuke Kondo, Mr. Atsushi Ando, Mr. Kota Mase, Mr. Tetsuya Kimura, Mr. Hiroki Kuroda, Mr. Yuto Matsudaira, Mr. Hiroyuki Mikuni, Mr. Sho Kawashima, Mr. Tokushige Kino, Mr. Shinpei Amasaki, Mr. Masanori Kato, Mr. Takayuki Kanda, Mr. Yasuyuki Yasuda, Mr. Naoya Sumi, Mr. Tatsuya Hagino, Mr. Kohei Asano, Mr. Jun Kuki, Mr. Ryosuke Kometani, Mr. Atsushi Fukushima, Mr. Takeyoshi Horibe, Ms. Ya Lu, Mr. Leyong Yu, Mr. Jiadong Cao, Mr. Kuangda Sun, Mr. Haoran Wang, Mr. Zecheng Liu, Mr. Takashi Kako, Mr. Masayuki Nakamura, Mr. Keita Miwa, Mr. Xu Da, Mr. Harry Zhang, Ms. Sijie Liang, and all other students who have studied in Profeessor Hori and Professor Sekine Laboratory for giving the big pleasure in life and creating a most enjoyable work atmosphere..

The author appreciates Ms. Azusa Ohta, Ms. Megumi Oshigane, Ms. Naoko Kataoka, Ms. Masako Takahashi, Ms. Yukie Kase, and Ms. Machiko Sakai for lots of encouragements and helpful advices in day-to-day life.

Finally, the author would like to appreciate his family including Mr. Akira Shimoeda, Ms. Chieko Shimoeda, Mr. Daisuke Shimoeda, Mr. Masaya Shimoeda, his grandparents, uncles, aunts, and cousins, for their help, support, and encouragement.

*Hironao Shimoeda*

February 2014

# List of papers related to this thesis

## 1. Original Papers

| Title | Journal | Authors<br>Related Chapter |
|---|---|---|
| 1. Atomic Oxygen Etching form the Top Edges of Carbon Nanowalls | Applied Physics Express **6** 095201 (2013). | H. Shimoeda, H. Kondo, K. Ishikawa, M. Hiramatsu, M. Sekine, and M. Hori |
| 2. Nanostructure modification to carbon nanowall surface employing hydrogen peroxide solution | Japanese Journal of Applied Physics (Accepted) | H. Shimoeda, H. Kondo, K. Ishikawa, M. Hiramatsu M. Sekine, and M. Hori |
| 3. Porous Graphene Materials Fabricated by Hierarchical Regrowth of Flowerlike Nanographene Sheets on Oxygen-plasma Treated Carbon Nanowalls | Applied Physics Express (submitted) | H. Shimoeda, H. Kondo, K. Ishikawa, M. Hiramatsu M. Sekine, and M. Hori |

## 2. International Conferences

| Title | Conference | Authors |
|---|---|---|
| 1. Effect of Oxygen Etching on the Morphologies of Carbon Nanowalls | 2nd International Symposium on Advance Plasma Science and its Application, PA082C, Meijo University, Nagoya, Japan, Mar. 7-10, 2010 | H. Shimoeda, Y. Miyawaki, K. Takeda, K. Ishikawa, H. Kondo, M. Hiramatsu, M. Sekine, and M. Hori |
| 2. Morphological modification of carbon nanowalls by oxygen plasma etching | International Symposium on Technology Evolution for Silicon Nano-Electronics, P-30, Tokyo Institute of Technology, Tokyo, Japan, Jun. 3-5, 2010 | H. Shimoeda, Y. Miyawaki, K. Takeda, M. Hiramatsu, M. Sekine, and M. Hori |
| 3. Effects of Substrate Temperatures on Crystallographic Changes of Carbon Nanowalls Induced by Radical Irradiation | 3rd International Symposium on Advanced Plasma Science and its Applications for Nitrides and Nanomaterials, P1-048C, Nagoya Institute of Technology, Nagoya, Japan, Mar. 6-9, 2011 | H. Shimoeda, H. Kondo, K. Takeda, K. Ishikawa, M. Hiramatsu, M. Sekine, and M. Hori |
| 4. Effects of Oxgen Radical Irradiation on Crystalline Structures of Carbon Nanowalls | The 13th International Workshop on Advanced Plasma Processing and Diagnostics, p-17, Daejeon Convention Center, Deajeon, Korea, Jul. 21-22, 2011 | H. Shimoeda, H. Kondo, K. Ishikawa, M. Hiramatsu, M. Sekine, and M. Hori |
| 5. Evaluation of crystallographic properties of carbon nanowalls by raman spectroscopy | 4th International Symposium on Advanced Plasma Science and its Applications for Nitrides and Nanomaterials, P3086C, Chubu Univ., Aichi, Japan, Mar. 4-8, 2012 | H. Shimoeda, H. Kondo, K. Ishikawa, M. Hiramatsu, M. Sekine, and M. Hori |
| 6. Edge and Surface Modification of Nanographenes in Carbon Nanowalls by Hydrogen Peroxide Treatments | The 4th International Conference on Microelectronics and Plasma Technology, N047, Ramada Plaza Jeju Hotel, Jeju, Korea, July 4-6, 2012 | H. Shimoeda, H. Kondo, K. Ishikawa, M. Hiramatsu, M. Sekine, and M. Hori |

| Title | Conference | Authors |
|---|---|---|
| 7. Effects of Hydroxyl Radicals on Crystallographic and Electrinic Structures of Carbon Nanowalls | The 16th International Workshop on Advanced Plasma Processing and Diagnostics, Okazaki Conference Center, Okazaki, Japan, Jan. 25-27, 2013 | H. Shimoeda, H. Kondo, K. Ishikawa, M. Hiramatsu, M. Sekine, and M. Hori |
| 8. Effects of morphological changes induced by hydrogen peroxide treatment on electrical properties of carbon nanowalls | 5th International Symposium on Advanced Plasma Science and its Applications for Nitrides and Nanomaterials, P1061C, Nagoya, Japan, Jan. 28-Feb. 1, 2013 | H. Shimoeda, H. Kondo, K. Ishikawa, M. Hiramatsu, M. Sekine, and M. Hori |
| 9. Crystallographic and chemical modification of carbon nanowalls by radical oxidation | The 12th Asia Pacific Physics Conference of AAPPS and The 3rd Asia-Europe Physics Summit, International Conference Halls, Makuhari Messe Chiba, Japan, Jul. 14-19, 2013 | H. Shimoeda, H. Kondo, K. Ishikawa, M. Hiramatsu, M. Sekine, and M. Hori |
| 10. Effects of Hydrogen Peroxide Treatment on Nanostructures in Carbon Nanowalls | International Union of Materials Research Societies - Internet Conference on Electronic Materials 2012, D-4-O24-012, Yokohama, Japan, Sep. 23-28, 2012 | H. Shimoeda, H. Kondo, K. Ishikawa, M. Hiramatsu, M. Sekine, and M. Hori |
| 11. Effects of Hydroxyl Radical on Nanographene Surfaces in Carbon Nanowalls | 11th Asia-Pacific Conference on Plasma Science and Technology and 25th Symposium on Plasma Science for Materials, Kyoto University ROHM Plaza, Kyoto, Japan, Oct. 2-5, 2012 | H. Shimoeda, H. Kondo, K. Ishikawa, M. Hiramatsu, M. Sekine, and M. Hori |

## 3. Research Projects

International Training Program (Program for incubating young researchers on plasma nanotechnology materials and device processing, conducted by Japan Society for the Promotion of Science)

1. The University of Texas at Dallas, International Center for Advanced Materials Processing (ICAMP), America, from January to March, 2011
2. Sungkyunkwan University, Center for Advance Plasma Surface Technology (CAPST), Korea, from September to November, 2012.

## 4. Award

1. Effects of Hydroxyl Radicals on Crystallographic and Electrinic Structures of Carbon Nanowalls
   The 16th International Workshop on Advanced Plasma Processing and Diagnostics, Okazaki Conference Center, Okazaki, Japan, Jan. 25-27, 2013
   Best Student Award.